Universität Bonn

Physikalisches Institut

Measurement of the Weak Mixing Angle and the Spin of the Gluon from Angular Distributions in the Reaction $pp \to Z/\gamma^* + X \to \mu^+\mu^- + X$ with ATLAS

Kristof Schmieden

The measurement of the effective weak mixing angle with the ATLAS experiment at the LHC is presented. It is extracted from the forward–backward asymmetry in the polar angle distribution of the muons originating from Z boson decays in the reaction $pp \to Z/\gamma^* + X \to \mu^+\mu^- + X$. In total $4.7\,\text{fb}^{-1}$ of proton–proton collisions at $\sqrt{s} = 7\,\text{TeV}$ are analysed. In addition, the full polar and azimuthal angular distributions are measured as a function of the transverse momentum of the Z/γ^* system and are compared to several simulations as well as recent results obtained in $p\bar{p}$ collisions. Finally, the angular distributions are used to confirm the spin of the gluon using the Lam-Tung relation.

Physikalisches Institut der
Universität Bonn
Nußallee 12
D-53115 Bonn

BONN-IR-2013-06
April 2013
ISSN-0172-8741

Universität Bonn

Physikalisches Institut

Measurement of the Weak Mixing Angle and the Spin of the Gluon from Angular Distributions in the Reaction $pp \to Z/\gamma^* + X \to \mu^+\mu^- + X$ with ATLAS

Kristof Schmieden

Dieser Forschungsbericht wurde als Dissertation von der Mathematisch-Naturwissenschaftlichen Fakultät der Universität Bonn angenommen und ist 2013 auf dem Hochschulschriftenserver der ULB Bonn `http://hss.ulb.uni-bonn.de/diss_online` elektronisch publiziert.

1. Gutachter:	Prof. Dr. Norbert Wermes
2. Gutachter:	Prof. Dr. Jochen Dingfelder
Angenommen am:	04.12.2012
Tag der Promotion:	22.04.2013

Contents

List of Acronyms

MC Monte–Carlo

PDF parton density function

bg background

SF scale factor

CB combined

MCP Muon Combined Performance

EV eigenvector

GRL good run list

SM Standard Model

GWS Glashow-Weinberg-Salam

QCD quantum chromodynamics

QED quantum electrodynamics

EW electro-weak

LO leading order

NLO next-to-leading order

ISR initial state radiation

BC bunch crossing

LHC Large Hadron Collider

ID inner detector

MS muon spectrometer

TRT transition radiation tracker

CSC cathode strip chamber

MDT monitored drift tube

RPC resistive-plate chamber

TGC thin-gap chamber

A_{fb} forward-backward asymmetry

CS frame Collins-Soper frame

1. Introduction

Human desire to understand the world, in which we live, propelled the development of religion, philosophy and natural sciences which, from different perspectives, all are addressing fundamental questions about the origin of our world, the structures inherent and our existence itself. It drove high energy particle physics as a broad field of fundamental research dedicated to unravel the fundamental constituents of matter. With the construction of more and more powerful accelerators the exploration of smaller and smaller structures became possible, leading to the discovery of new fundamental particles. In the 1960's a theoretical model has been developed which consistently describes the elementary particles and the interactions among them. It is called the Standard Model (SM) of particle physics. Additional fundamental particles were predicted before their experimental discovery, e.g. the charm and top quark, the latter having been discovered in 1995.

Despite this great success of the SM, it leaves fundamental questions unanswered. The SM, apart from other short comings, neither explains the observation of dark matter on cosmological scales nor the fact that three families of leptons and quarks are observed which only differ by their masses, while the interactions are identical. It is very difficult to understand why weak nuclear interactions and gravity differ by as much as 32 orders of magnitude in strength, i.e. their coupling constants. In fact, gravity is not considered at all in the SM and the numerous attempts to include it have been unsuccessful up to now. Therefore the SM can not be complete. A strong effort is currently underway to experimentally establish the process which gives mass to the fundamental particles of the SM. This process is believed to be the Higgs mechanism [1] which requires the existence of a further elementary boson. It has not yet been experimentally identified and is the last missing particle in the SM.

In the hope to shed some light on the open questions of particle physics a new accelerator has been built at the European Organisation for Nuclear Research (CERN), the Large Hadron Collider (LHC) [2]. Together with its experiments it is the largest global effort ever to investigate the fundamental structure of matter. The accelerator is designed to produce proton–proton collisions at a center-of-mass energy of $\sqrt{s} = 14\,\text{TeV}$. Since the start of the data taking in 2010, at a center of mass energy of 7TeV, many results have been published, culminating in the first ground-breaking discovery of a new particle in July 2012. It is a strong candidate for the long searched Higgs boson. However, the nature of the new particle still has to be studied. Two experiments, ATLAS [3] and CMS [4], are optimised for the study of such new phenomena.

Besides the search for new particles strong effort is devoted to precisely measure and test the parameters of the SM in the new energy regime accessible at the LHC. Any deviation from the SM predictions would hint to new physics. Within the SM valuable information on the structure of the nucleon and the strong and electroweak forces can be obtained. This thesis is devoted to such a measurement. The di-muon channel is investigated in the reaction $pp \to Z/\gamma^* + X \to \mu^+\mu^- + X$. In particular, the angular distributions of the final state muon provide access to a fundamental parameter of the

SM, the weak mixing angle θ_W. It is measured in this thesis with an accuracy ten times better than before in proton–proton interactions. Although the precision does not reach that of the LEP[1] [5] experiments, it is of interest to study effects due to the hadronic initial state at the LHC. In addition, the angular distributions also allow a measurement of the spin of the gluon. Albeit already well known the spin determination provides an independent cross check of the observed properties of the studied reaction.

The thesis is structured as follows. First the theoretical foundations of the SM are presented with a focus on the electroweak interaction and a discussion of the angular distributions in the process $pp \to Z/\gamma^* + X \to \mu^+\mu^- + X$. Then the ATLAS experiment is introduced in chapter 4. Chapter 5 presents the measurement of the reconstruction efficiency of the final state muons. It provides a basis for measurements of the weak mixing angle and the spin of the gluon. The corresponding analyses are presented in chapters 6 and 7, respectively.

[1] The Large Electron Positron collider was located at CERN and until the year 2000 in operation. It was dedicated to electroweak precision measurements.

2. Theoretical Considerations

Four fundamental forces are presently known: gravity, electromagnetism, weak and strong force. All but gravity are described by the SM of particle physics. This theory includes the interactions of all known elementary particles which make up the visible matter in the universe. The design of the theory was finalized in the mid 1970's and numerous predictions of the SM have since been experimentally tested and confirmed. Several parameters are measured very accurately, e.g. the magnetic moment of the electron g which is measured to a precision of 10^{-13} [6]. Despite the tremendous success of the theory, it is not capable of explaining all observations in particle physics. Several experimentally established facts must be put explicitly into the model. A derivation from underlying theoretical principles is not possible at present, e.g. for the number of quark and lepton families. All attempts to incorporate gravity in a consistent way have failed so far. Furthermore, no potential particle for dark matter is available which seems to be responsible for more than 80 % of the total matter in the universe. Also the asymmetry between matter and antimatter in the universe remains unexplained up to now. To elucidate the boundaries of the model and hunt for possible signs of physics beyond the SM, direct searches for new particles as well as precision tests of parameters of the theory are performed in many different experiments.

This chapter briefly describes the elementary particles in the SM and the interactions among them. Special emphasis is put on the electroweak interaction, including spontaneous symmetry breaking and the weak mixing angle as well as higher order corrections and definitions of effective parameters of the theory. Discussions in this chapter are largely based on the textbooks [7] and [8].

2.1. The Standard Model of Particle Physics

Two types of fundamental particles are included in the model: *fermions* carry half-integer spin $S = \frac{1}{2}$ and are the basic constituents of matter. *Bosons* carry integer spin $S = 0, 1$ and mediate the forces between the fermions and, in some cases, also between themselves. The fundamental fermions can be divided into two types, leptons and quarks. Only the latter ones participate in the strong interaction, which distinguishes them from leptons. Six leptons are known: electron e, muon μ, tauon τ, all with electric charge[1] $Q = 1$, and the corresponding electrically neutral neutrinos ν_e, ν_μ and ν_τ. Neutrinos only interact via the weak force while the other leptons also interact electromagnetically.

Similarly to the leptons six *flavours* of quarks are known: u, c, t with charge $Q = +2/3$ and d, s, b with charge $Q = -1/3$. Additionally to the electric and weak charge quarks have another degree of freedom, called *color*, which can be either *red*, *green* or *blue*. Experiments suggest that all free particles are colorless (white), i.e. in a color singlet state. This is also known as *confinement* as all colored particles are confined in bound objects. It is realized in two ways. Three quarks carrying different colors form bound

[1] The electric charge is always stated in units of the elementary charge e.

Families			Quantum Numbers				
1	2	3	T	T^3	Y	Q	C
Leptons							
$\begin{pmatrix}\nu_e\\e^-\end{pmatrix}_L$	$\begin{pmatrix}\nu_\mu\\\mu^-\end{pmatrix}_L$	$\begin{pmatrix}\nu_\tau\\\tau^-\end{pmatrix}_L$	$\begin{pmatrix}1/2\\1/2\end{pmatrix}$	$\begin{pmatrix}1/2\\-1/2\end{pmatrix}$	$\begin{pmatrix}-1\\-1\end{pmatrix}$	$\begin{pmatrix}0\\-1\end{pmatrix}$	$\begin{pmatrix}0\\0\end{pmatrix}$
e_R^-	μ_R^-	τ_R^-	0	0	-2	-1	0
Quarks							
$\begin{pmatrix}u\\d\end{pmatrix}_L$	$\begin{pmatrix}c\\s\end{pmatrix}_L$	$\begin{pmatrix}t\\b\end{pmatrix}_L$	$\begin{pmatrix}1/2\\1/2\end{pmatrix}$	$\begin{pmatrix}1/2\\-1/2\end{pmatrix}$	$\begin{pmatrix}1/3\\1/3\end{pmatrix}$	$\begin{pmatrix}2/3\\-1/3\end{pmatrix}$	$\begin{pmatrix}r,g,b\\r,g,b\end{pmatrix}$
u_R	c_R	t_R	0	0	4/3	2/3	r,g,b
d_R	s_R	b_R	0	0	-2/3	-1/3	r,g,b

Table 2.1.: Elementary fermions and their quantum numbers (explained in the subsequent paragraph), T: Weak isospin; T^3: 3rd component of weak isospin; Y: Hypercharge; Q: electric charge; C: color charge. All quantum numbers flip their sign when considering anti-fermions.

states called baryons. Examples are the proton (uud) and neutron (udd). Alternatively, quark-antiquark pairs – called mesons – represent color singlets when combining color and the corresponding anticolor, e.g. π^+ ($u\bar{d}$). Mesons and baryons participate in the strong interaction and are referred to as hadrons.

An overview of all fermions and their quantum numbers is shown in table 2.1. They are organised in three families, also called generations, which only differ in the mass of the fermions and their flavour. All macroscopic objects are built of the four particles belonging to the 1st generation, e, ν_e, u and d. Heavier fermions of the 2nd and 3rd generations always decay into lighter ones via the weak interaction.

Within the SM forces are described as gauge fields and are mediated by corresponding gauge bosons, which are identified with the generators of the underlying symmetry group of each interaction. The electromagnetic interaction, mediated by the photon (γ), is described within a theory called quantum electrodynamics (QED) which is invariant under U(1) gauge transformations. The weak interaction is described by a field theory with an underlying SU(2) symmetric gauge group with three gauge bosons: the charged W^+ and W^- and the neutral Z^0. Both forces have been successfully combined to a single underlying interaction called the *electroweak* interaction, which is formulated as a $\mathrm{SU(2)_L} \otimes \mathrm{U(1)_Y}$ gauge group. The subscript L denotes *left handed* and Y the *hypercharge*. This interaction is of special interest for this thesis and will be explained in more detail in section 2.1.1. The strong force can be formulated as a field theory with underlying gauge group $\mathrm{SU(3)_C}$[2], which has eight generators corresponding to eight differently colored gauge bosons called gluons (g). Gluons carry color and anti-color themselves and therefore interact with each other, which is one of the peculiarities of this theory called quantum chromodynamics (QCD). It will be briefly discussed in section 2.1.3. Despite all efforts it has not yet been possible to unify strong and electroweak interactions. It is strongly believed, however, that this is not a problem in principle, and the quantum theory underlying the SM is assigned the symmetry structure $\mathrm{SU(3)_C} \otimes$

[2]The index C denotes the *color* charge of the involved particles.

interaction	charge	gauge Boson(s)	
		symbol	charges carried
electromagnetic	Q	γ	none
weak	weak isospin T	W^+, W^-, Z	weak, electric (only $W^\pm$)
strong	color C	g_i, $i = 1 \dots 8$	color

Table 2.2.: Forces described by the Standard Model, their charges and force mediating gauge bosons.

$\mathrm{SU(2)_L} \otimes \mathrm{U(1)_Y}$. Forces, corresponding charges and gauge bosons are summarized in table 2.2.

2.1.1. Electroweak interaction

Experimental studies of the β-decay revealed that only left handed leptons take part in charged current weak interactions. The interactions can be described by a combination of vector (V) and axialvector (A) operators which turns out to be V-A. Hence, the theory is also called *V-A* theory. Left handed (Weyl-) fermions [9] are obtained by means of the helicity operator: $f_L = 0.5(1 - \gamma_5)f$, where f is the dirac spinor describing a fermion. Leptons l ($l = e, \mu, \tau$) and the corresponding neutrinos ν_l are combined into a left handed doublet L^l and a right handed singlet R^l under the weak SU(2) symmetry:

$$\mathrm{L}^l = \frac{1}{2}(1-\gamma_5)\begin{pmatrix}\nu_l\\ l^-\end{pmatrix} = \begin{pmatrix}\nu_l\\ l^-\end{pmatrix}_{\mathrm{L}}, \qquad \mathrm{R}^l = \frac{1}{2}(1+\gamma_5)\,l^- = l^-_{\mathrm{R}}. \tag{2.1}$$

Using this, the charged currents can be written as

$$J^{l,\pm}_\mu = \bar{\mathrm{L}}^l \gamma_\mu \tau^\pm \mathrm{L}^l, \tag{2.2}$$

with $\tau^\pm = (\tau^1 \pm i\tau^2)/2$ and τ^j being the Pauli matrizes[3]. Together with the neutral current

$$J^{l,3}_\mu = \bar{\mathrm{L}}^l \gamma_\mu \frac{\tau^3}{2} \mathrm{L}^l \tag{2.3}$$

they form a weak isospin triplet under SU(2):

$$J^{l,j}_\mu = \bar{\mathrm{L}}^l \gamma_\mu T^j \mathrm{L}^l = \bar{\mathrm{L}}^l \gamma_\mu \frac{\tau^j}{2} \mathrm{L}^l, \qquad for\ (j = 1,2,3) \tag{2.4}$$

with T^j being the corresponding weak charge which obeys the SU(2) algebra. Due to the presence of a vector–operator (γ_μ) weak interactions violate parity conservation.

In order to combine the weak with the electromagnetic force a new quantum number called *weak hypercharge* is introduced. It is the eigenvalue of Y which is related to the simultaneous symmetry under the groups $U(1)_Y$ and $SU(2)_L$:

$$Y = 2\left(Q - T^3\right). \tag{2.5}$$

[3] Pauli matrizes: $\tau^1 = \left(\begin{smallmatrix}0&1\\1&0\end{smallmatrix}\right)$, $\tau^2 = \left(\begin{smallmatrix}0&-i\\i&0\end{smallmatrix}\right)$, $\tau^3 = \left(\begin{smallmatrix}1&0\\0&-1\end{smallmatrix}\right)$. τ^j is used to denote the Pauli matrices instead of the usual σ^j to make clear that they are applied in weak isospin space, and not the regular spin space.

$\frac{Y}{2}$ is the generator of the $U(1)_Y$ group. The concept of combining two charges in this way originates from the Nakano-Nishijima-Gell-Mann relation [10] in which strong isospin and electric charge are combined to the *hypercharge* in the same way.

Knowing the currents, a lagrangian $\mathscr{L}$ with $SU(2)_L \otimes U(1)_Y$ symmetry is constructed. It is divided in parts $\mathscr{L} = \mathscr{L}_F + \mathscr{L}_G + \mathscr{L}_S + \mathscr{L}_Y$ describing the interaction of fermions, kinetic energy of the gauge field, a scalar field and a Yukawa type interaction between the scalar field and the fermions, respectively. The fermionic part is constructed as[4]

$$\mathscr{L}_F = \sum_{l=e,\mu\tau} \left[\bar{\mathrm{L}}^l i\gamma^\mu D_\mu \mathrm{L}^l + \bar{\mathrm{R}}^l i\gamma^\mu D_\mu \mathrm{R}^l\right] \tag{2.6}$$

$$= \sum_{l=e,\mu\tau} \bar{\mathrm{L}}^l i\gamma^\mu (\partial_\mu - ig\frac{\vec{\tau}}{2}\cdot\vec{W}_\mu + \frac{i}{2}g'B_\mu)\mathrm{L}^l + \bar{\mathrm{R}}^l i\gamma^\mu(\partial_\mu + ig'B_\mu)\mathrm{R}^l. \tag{2.7}$$

W^i_μ, $i = 1,2,3$ and B_μ are the massless gauge boson fields of $SU(2)_L$ and $U(1)_Y$, respectively, and g, g' the corresponding couplings. Note that the singlet states R do not couple to W^i_μ. The covariant derivative is defined as

$$D_\mu = \partial_\mu - ig\frac{\vec{\tau}}{2}\cdot\vec{W}_\mu - ig'\frac{Y}{2}B_\mu \tag{2.8}$$

with $Y = -1$ for L and $Y = -2$ for R. The kinetic energy term of the gauge fields, which should be added to $\mathscr{L}_F$, is written as

$$\mathscr{L}_G = -\frac{1}{4}F^i_{\mu\nu}F^{i\mu\nu} - \frac{1}{2}B_{\mu\nu}B^{\mu\nu},\ (i = 1,2,3) \tag{2.9}$$

where $F^i_{\mu\nu}$ and $B_{\mu\nu}$ are the field strength tensors of the gauge fields corresponding to $SU(2)_L$ and $U(1)_Y$, respectively. Gauge boson mass terms do not appear in this theory as they would break the local gauge invariance of the lagrangian. To make fermions and all bosons but the photon massive a spontaneous breakdown of the electroweak symmetry is needed [11], i.e. the Higgs mechanism [1]. The symmetry is broken as:

$$SU(2)_L \otimes U(1)_Y \to U(1)_{em}\,. \tag{2.10}$$

In order to achieve the electroweak symmetry breaking in the simplest way a doublet of complex scalar fields is added to the theory:

$$\mathscr{L}_S = (D_\mu\phi)^\dagger(D^\mu\phi) - V(\phi^\dagger\phi);\ \phi = \begin{pmatrix}\varphi^+\\ \varphi^0\end{pmatrix},\ Y_\phi = +1,\ \varphi^0\text{neutral},\ \varphi^+\text{charged}. \tag{2.11}$$

The potential V is defined in a gauge invariant way by

$$V(\phi^\dagger\phi) = m^2\phi^\dagger\phi + \lambda(\phi^\dagger\phi)^2, \quad m,\lambda \in \mathbb{R}. \tag{2.12}$$

Higher orders of $(\phi^\dagger\phi)$ are not allowed in order to keep the theory renormalizable. To ensure the stability of the vacuum, λ has to be greater than zero. If in addition $m^2 = -\mu^2$ is chosen negative, the potential takes the famous shape of a mexican hat, illustrated

[4] The scaler product for 3-vectors is always indicated by using variables overset with vector symbols, whereas the Einstein summation convention is used for 4-vectors.

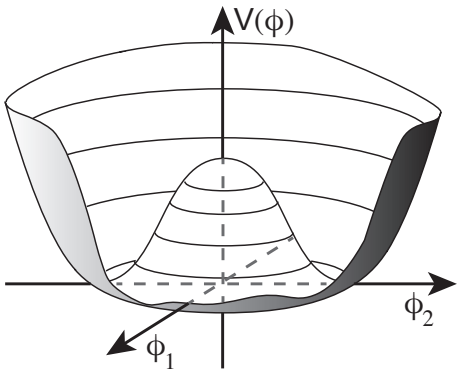

Figure 2.1.: Illustration of the shape of the potential according to Eq. (2.12). The import feature is the degenerate ground state lying on a circle around the $V(\phi)$ axis. The symmetry is spontaneously broken when a physical ground state develops by choosing a specific position in the degenerate minimum of $V(\phi)$.

in Fig. 2.1. Couplings of the scalar fields to fermions are defined as Yukawa type interactions, respecting the $SU(2)_L \otimes U(1)_Y$ symmetry:

$$\mathscr{L}_Y = -\sum_{l,j}^{e,\mu,\tau} G^{lj}(\bar{\mathrm{L}}^l \phi \mathrm{R}^j + \bar{\mathrm{R}}^l \phi^\dagger \mathrm{L}^j) + h.c. \tag{2.13}$$

The full lagrangian of the electroweak theory is obtained as the sum of the discussed parts: $\mathscr{L} = \mathscr{L}_F + \mathscr{L}_G + \mathscr{L}_S + \mathscr{L}_Y$.

Another very convincing need for an additional particle in the framework of the standard model arises from the scattering cross section of W bosons. This process violates unitarity for larger energies, in case no scalar field is considered. This is fixed by introducing an additional particle, like the Higgs boson, which leads to an additional diagram in the scattering amplitude.

Electroweak symmetry breaking

The potential of the scalar fields given in Eq. (2.12) and illustrated in Fig. 2.1 has a degenerate ground state, as the minimum $\min\{\phi^\dagger\phi\} = \min\{|\phi|^2\} = v^2/2$, with $v := \sqrt{\mu^2/\lambda}$, describes a circle in the ϕ^0–ϕ^+ plane. Through the choice of any (arbitrary) value $\phi_0 = <0|\phi|0>$ for the ground state, the symmetry is spontaneously broken. All generators T^j and Y are broken as they do not annihilate the vacuum, i.e. $Y|0> \neq 0$, whereas the charge operator $Q = T^3 - Y/2$ remains unbroken, i.e. $Q\phi_0 = 0 \Rightarrow e^{-i\varepsilon Q}\phi_0 = \phi_0$ with $\varepsilon \in \mathbb{R}$ being arbitrary. Hence, the remaining symmetry of the theory is $U(1)_{em}$, consistent with experimental observations. From the three generators of the gauge groups belonging to the broken symmetries three massless Goldstone bosons[5] are expected, which become visible in the following parametrization of ϕ:

$$\phi = \begin{pmatrix} \varphi^+ \\ \varphi^0 \end{pmatrix} = e^{i\vec{\tau}\cdot\vec{\xi}/2v} \begin{pmatrix} 0 \\ (v+H)/\sqrt{2} \end{pmatrix}; \quad \xi^j,\ j = 1,2,3 \text{ and } H \in \mathbb{R}. \tag{2.14}$$

[5] After the Goldstone theorem [12] each broken symmetry leads to a massless boson, called Goldstone boson.

The ξ^j are interpreted as Goldsone bosons and H is called the Higgs boson which is a scalar particle.

A special gauge called *unitary gauge* can be found such that the three Goldstone bosons disappear and all fields can be associated with particles again. The appropriate gauge transformations is

$$U(\vec{\xi}) = e^{-i\vec{\tau}\cdot\vec{\xi}/2v}. \tag{2.15}$$

All transformed fields will be labelled with a prime. Now the first term of Eq. (2.11), which describes the dynamics of free gauge bosons and contains the mass-squared term for the weak gauge bosons, becomes

$$\mathscr{L}_{\text{mass}} = (D_\mu\phi)'^{\dagger}(D^\mu\phi)' = \frac{v^2}{8}\left(g^2 W'^1_\mu W'^{1\mu} + g^2 W'^2_\mu W'^{2\mu} + (gW'^3_\mu - g'B'_\mu)^2\right). \tag{2.16}$$

The physical, charged boson fields are defined as

$$W^\pm_\mu = \frac{W'^1_\mu \mp iW'^2_\mu}{\sqrt{2}}. \tag{2.17}$$

With this the first two terms of Eq. (2.16) simplify to $g^2v^2W^+_\mu W^-_\mu/4$ which corresponds to the squared mass term of the W bosons $M_W = gv/2$, assuming the same absolute charge for both W bosons. The weak eigenstates in the remaining term of Eq. (2.16) can be expressed in terms of mass eigenstates in the following way:

$$\begin{pmatrix} Z_\mu \\ A_\mu \end{pmatrix} = \begin{pmatrix} \cos\theta_W & -\sin\theta_W \\ \sin\theta_W & \cos\theta_W \end{pmatrix} \begin{pmatrix} W'^3_\mu \\ B'_\mu \end{pmatrix}. \tag{2.18}$$

Applying this rotation the last term in Eq. (2.16) reads

$$\frac{v^2}{8}\,(Z_\mu\ A_\mu) = \begin{pmatrix} g^2+g'^2 & 0 \\ 0 & 0 \end{pmatrix} \begin{pmatrix} Z^\mu \\ A^\mu \end{pmatrix} = \frac{v^2}{8}(g^2+g'^2)Z_\mu Z^\mu + 0\cdot A_\mu A^\mu. \tag{2.19}$$

θ_W is called *weak mixing* or *Weinberg* angle and is the observable of interest in chapter 6 which deals with its measurement. The mixing angle is affected by several higher order corrections which lead to the definition of an effective mixing angle discussed in sec. 2.1.2. From Eq. (2.19) the Z mass is found to be $M_Z = v\sqrt{g^2+g'^2}/2$ whereas the field A_μ, which is associated with the photon, remains massless. The masses of the W and Z bosons are related via

$$\cos\theta_W = \frac{M_W}{M_Z}. \tag{2.20}$$

As a direct consequence the relation $g' = \tan\theta_W g$ between both involved coupling constants is obtained.

Also fermions acquire mass by spontaneous symmetry breaking. This exhibits when $\mathscr{L}_Y$ is considered in unitary gauge. It contains mass terms of the form $G_{l,j}v/\sqrt{2}\bar{\mathrm{L}}^l\mathrm{R}^j$. As neutrinos are massless in this theory the matrix relating their weak eigenstates to the mass eigenstates can be diagonalized and no mixing between mass eigenstates and flavour eigenstates is found. This leads to flavour conservation in the Glashow-Weinberg-Salam (GWS) model, which is violated for the case of massive neutrinos. In the quark sector the picture changes. As quarks are massive, with very different masses, weak and mass eigenstates are not identical. This gives rise to the CKM matrix [13] describing the flavour mixing of the mass eigenstates.

Finally, the mass term of the Higgs boson in the scalar potential

$$V(\phi' \dagger \phi') = -\frac{\mu^2 v^2}{4} + \frac{1}{2}\left(2\mu^2\right) H^2 + \lambda v H^3 + \frac{\lambda}{4} H^4 \tag{2.21}$$

is found to be $M_H = \sqrt{2\mu^2}$. The exact value can not be predicted in the GWS model. Recently the LHC experiments ATLAS and CMS announced the discovery of a new particle with a mass of $126\,\mathrm{GeV/c^2}$ [14, 15], which is a candidate for the long searched Higgs boson. The discovery of H would fix the value of μ, the last unknown fundamental parameters of the SM.

The fermion lagrangian in the unitary gauge reads

$$\mathscr{L}_F = \sum_l^{e,\mu,\tau} \left[\bar{\mathrm{L}}'^l i\gamma^\mu \partial_\mu \mathrm{L}'^l + \bar{\mathrm{R}}'^l i\gamma^\mu \partial_\mu \mathrm{R}'^l + g \vec{J}^l_\mu \cdot \vec{A}'^\mu + \frac{g'}{2} J^{Yl}_\mu B'^\mu \right] \tag{2.22}$$

where the first two terms describe the kinetic energy of a lepton and its neutrino. The last two terms represent the electroweak currents which can be split into neutral and charged currents, where the neutral current can be further divided into the electromagnetic and weak contributions (1st and 2nd term in Eq. (2.24), respectively)

$$\mathscr{L}_{\mathrm{CC}} = g\left(J^{l1}_\mu A'^\mu + J^{l2}_\mu A'^\mu\right) = \frac{g}{\sqrt{2}}\left(J^{l-}_\mu W^{-\mu} + J^{l+}_\mu W^{+\mu}\right) \quad \text{and} \tag{2.23}$$

$$\begin{aligned}
\mathscr{L}_{\mathrm{NC}} &= g J^{l3}_\mu A'^{3\mu} + \frac{1}{2} g' J^{lY}_\mu B'^\mu \\
&= \left(g \sin\theta_W J^{l3}_\mu + g' \cos\theta_W \frac{J^{lY}_\mu}{2}\right) A^\mu + \left(g \cos\theta_W J^{l3}_\mu - g' \sin\theta_W \frac{J^{lY}_\mu}{2}\right) Z^\mu \\
&= g \sin\theta_W J^{em}_\mu A^\mu + \frac{g}{\cos\theta_W}\left(J^{l3}_\mu - \sin^2\theta_W J^{em}_\mu\right) Z^\mu .
\end{aligned} \tag{2.24}$$

From the second term in the weak neutral current (Eq. (2.24)) the coupling to left and right handed fermions follows as $g_R = -Q_f \sin^2\theta_W$ and $g_L = T^3_f - Q_f \sin^2\theta_W$, where Q is the electric charge in units of e. The vector and axialvector couplings are then given as:

$$g^f_V = g^f_L + g^f_R = T^3_f - 2Q_f \sin^2\theta_W \tag{2.25}$$

$$g^f_A = g^f_L - g^f_R = T^3_f \tag{2.26}$$

$$\Rightarrow \sin^2\theta_W = \left(1 - \frac{g_V}{g_A}\right)\frac{T^3_f}{2Q_f} \tag{2.27}$$

2.1.2. Effective weak mixing angle and higher order corrections

Without further ado the theory described in the previous chapter is only consistent in lowest order of perturbation theory, called tree level. Infinite integrals appear when considering higher order diagrams like photon radiation or internal loops, examples of which are shown in Fig. 2.2. Divergences of these kind can be absorbed when redefining the physical parameters of the theory, a procedure called renormalisation. The redefined quantities are considered to be the observables accessible in experiments and the 'bare' parameters of the theory may differ from them. The exact value of an observable predicted by theory depends on the chosen renomalisation procedure and scale. Many

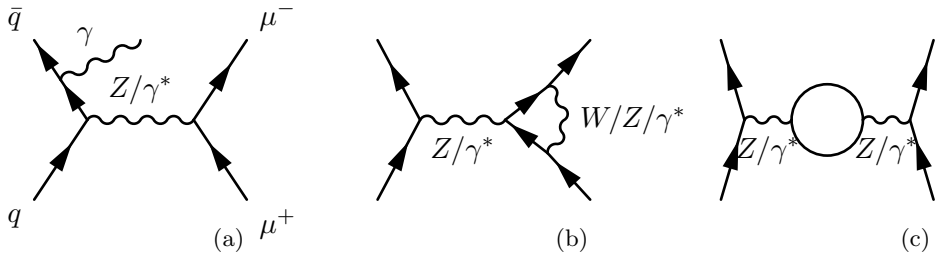

Figure 2.2.: Exemplary next-to-leading order diagrams representing three types of electroweak corrections to the Z production and decay. (a): Initial state photon radiation. (b): Electroweak final state correction. (c): Propagator correction, leading to running of α_{em}.

electroweak corrections can be absorbed into a renormalised Fermi coupling constant G_F. The tree level expression of the couplings given in Eq. (2.25) and (2.26) is then modified to

$$\bar{g}_V^f = \sqrt{\rho_f}\left(T_f^3 - 2Q_f\kappa_f \sin^2\theta_W\right), \quad \bar{g}_A^f = \sqrt{\rho_f}\, T_f^3. \tag{2.28}$$

The radiative electro-weak (EW) corrections are absorbed into ρ_f and κ_f which depend on the fermion f and the used renormalisation scheme and scale. It is convenient to define an effective weak mixing angle such that the couplings are the tree level expressions times $\sqrt{\rho_f}$, i.e.

$$\sin^2\theta_W^{\text{eff}} = \kappa_f \sin^2\theta_W \text{ and } \bar{g}_V^f = \sqrt{\rho_f}\left(T_f^3 - 2Q_f \sin^2\theta_W^{\text{eff}}\right). \tag{2.29}$$

In the Monte–Carlo (MC) simulation program PYTHIA, which is used in this thesis, the modified minimal subtraction scheme ($\overline{\text{MS}}$ scheme) [16] is used in the renormalisation procedure. This scheme greatly reduces the dependence of SM parameters on the top mass. The parameters of the effective couplings are $\sqrt{\rho_l} = 0.9981$ and $\kappa_l = 1.0013$ which translates into

$$\sin^2\theta_W^{\text{eff}} = \sin^2\theta_W^{\overline{\text{MS}}}|_{M_Z} + 0.00029, \tag{2.30}$$

where $\sin^2\theta_W^{\overline{\text{MS}}}|_{M_Z}$ is the weak mixing angle calculated in the $\overline{\text{MS}}$ scheme with the renormalisation scale μ set to the Z mass. The extraction of the effective weak mixing angle from a global fit of the SM parameters to a variety of experimental data [17] yields $\sin^2\theta_W^{\text{eff}} = 0.23146 \pm 0.00012$.

Including 1-loop corrections in the calculation of $\sin^2\theta_W^{\overline{MS}}$ induces a scale dependence [18, 19] which is known as the running of $\sin^2\theta_W^{\overline{MS}}$. The scale dependence is shown in Fig. 2.3 together with experimental results. In the low energy region electron proton scattering is used to measure the weak mixing angle [20]. In the mid energy region neutrino scattering off iron [21] and at the Z mass the LEP [5], Tevatron [22] and LHC [23] experiments measure it.

2.1.3. Quantum Chromodynamics and phenomenology of proton–proton collisions

Quantum chromodynamics (QCD) is the quantum field theory to describe the interaction between color charged objects, i.e. quarks and gluons. There are three kinds of color charges labeled *red, green* and *blue*. QCD color interaction is related to the non abelian SU(3) symmetry group. Consequently, the force carrying gauge bosons, called

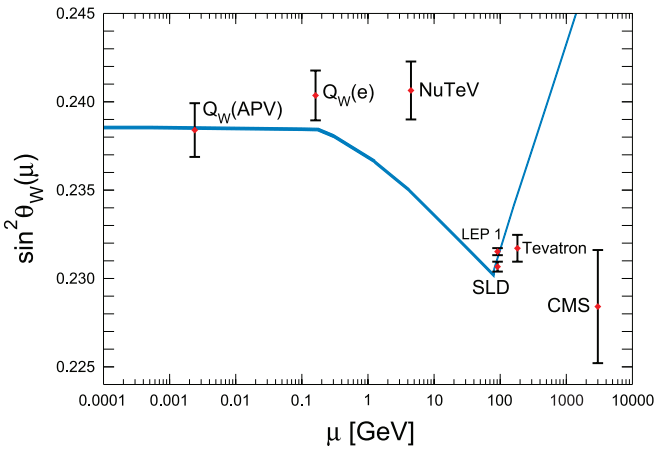

Figure 2.3.: Scale dependence of the weak mixing angle defined in the $\overline{\text{MS}}$ scheme [17]. The minimum of the curve corresponds to $\mu = M_W$. The discontinuities in the curve correspond to various thresholds in the renormalisation procedure, while the size of the theoretical uncertainties is reflected in the thickness of the line. The Tevatron and LHC measurements are dominated by the invariant mass of the final state dilepton pair of $\mathcal{O}(M_Z)$ and are considered additional Z pole data point. However, for clarity the points are shifted horizontally to the right.

gluons, carry color charge themselves and hence interact with each other. The strong coupling constant α_s has a particularly strong scale dependence, often referred to as *running*. For small momentum transfers, i.e. large distances, it is large (≈ 1) whereas it becomes smaller with increasing momentum transfer in the interaction[6]. The fact that the interaction becomes stronger for larger distances leads to the feature of *confinement*, which implies that quarks only exist in bound states of color singlets, also called colorless. On the other hand, for very short distances the coupling between quarks becomes so weak that they behave as virtually free particles. This is called asymptotic freedom and a perturbative treatment of the theory is only possible in this regime. Low energies remained a domain of (quark) models for long time. Only recently ab initio calculations carried out on a discrete space-time lattice ('Lattice QCD') made significant progress [24] in the confinement region.

Although the main topic of this thesis is related to electroweak interactions, QCD is necessary to describe the initial state of the proton–proton collisions for two reasons. First of all, protons are composite objects where the constituents are quarks and gluons. Macroscopic properties of the nucleons can be described by the three valence quarks. In high energy reactions, however, nucleons appear as objects composed of many quark–antiquark pairs in addition, the sea quarks, as well as gluons. While the proton's valence quarks must be either up or down, in general all flavours may contribute to the quark sea. However, the chance to find heavier quarks is suppressed by their larger mass. In fact, top quarks are virtually non existent in protons at the considered energy. As the quarks are moving within the proton their momentum is not well defined. However, it follows a universal probability distribution called parton density function (PDF). PDFs

[6]Note that this is opposite to the much weaker scale dependence of the electromagnetic coupling.

describe the probability of finding a parton of a given flavour with certain momentum fraction x of the total proton momentum. They depend on the scale determined by the involved momentum transfer Q^2. The matrix element describing the collision of two protons can be factorised in a matrix element describing the interaction of two partons at large momentum transfer, called the *hard interaction*, and factors describing the initial state for the hard interaction with the help of a PDF. However, PDFs can not get calculated from QCD but need to be measured. This was done in many experiments, most notably at HERA and the Tevatron. A chart of the mapped (x-Q^2) space is shown in Fig. 2.4. Note that W and Z production at the LHC probes a previously not accessed region, into which the measured PDFs are evolved. The evolution technique is a main difference between different PDFs, next to varying the input data used. In general, PDFs are afflicted with rather large uncertainties in some kinematic regions. A sample PDF is shown in Fig. 2.5. As can be seen, valence quarks carry on average a larger momentum than sea quarks. This is an important feature as it allows to statistically distinguish quarks and antiquarks in the initial state of proton–proton collisions.

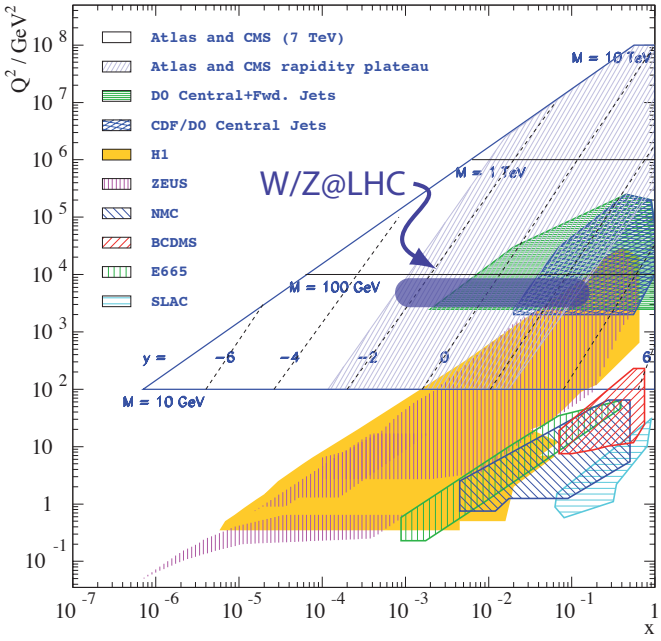

Figure 2.4.: Plotted is the momentum transfer squared Q^2 versus the momentum fraction x of a parton on the proton momentum [25]. Areas probed by experiments are marked as shaded areas. Most of the probed low Q^2 region has been studied by the HERA experiments. The Tevatron experiments probe the region with large x and $10^3\,\mathrm{GeV}^2 < Q^2 < 10^5\,\mathrm{GeV}^2$. The theoretically accessible region by the LHC experiments is indicated by blue line. Accessible by studies using W,Z bosons is the region between $10^{-3} < x < 10^{-1}$ and $Q^2 = M_{W,Z}$, indicated by the blue solid bar.

The second important aspect of the strong interaction in the process $pp \to Z/\gamma^* + X \to \mu^+\mu^- + X$ is the production of additional final state particles due to gluon radiation off quarks. The radiated gluons may carry a significant momentum fraction of the parent quark. In case gluon radiation occurs off the initial state partons the process is called

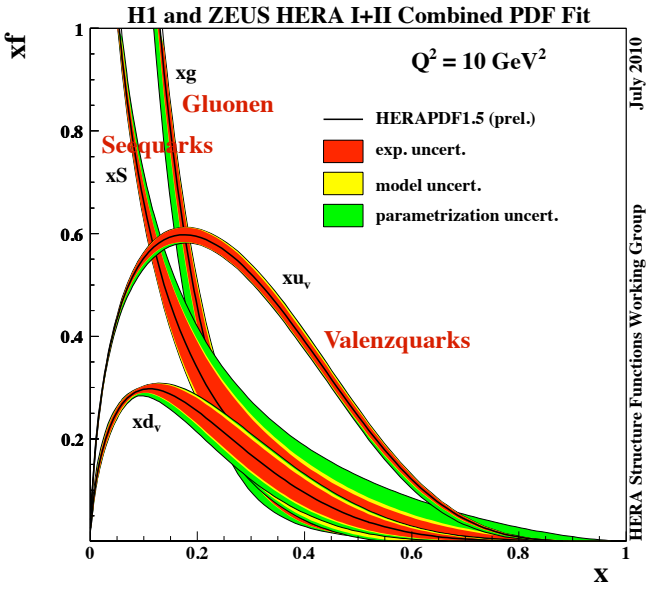

Figure 2.5.: Parton density distribution of the proton, as measured by the HERA collaborations [26]. Plotted is the probability xf to find a parton of a given momentum fraction x on the proton momentum versus the momentum fraction x. Valence quark momenta peak around $x = 0.1$ to $x = 0.2$, whereas sea quarks favour small momenta.

initial state radiation (ISR). Usually the gluons will then split into quark antiquark pairs. These processes lead to the formation of a parton shower. Finally all partons bind into (colorless) hadrons, a process referred to as hadronisation. Experimentally a shower of partons is therefore detected as a collimated bunch of particles which is called jet. The cross section for the production of electroweak bosons with additional jets is interesting in itself, as it is sensitive to the strong coupling. In addition to ISR, gluons can also originate from the hard interaction, yielding the same final state as ISR. In contrast to ISR, gluons participating in the hard interaction may influence the angular distributions of the final state leptons. This is described in more detail in the next section.

The total cross section for QCD reactions in proton–proton collisions at the LHC at $\sqrt{s} = 7\,\text{TeV}$ is 98 mb [27], which is eight orders of magnitude larger than the cross section for the reaction $pp \to Z/\gamma^* \to \mu^+\mu^-$ of 1 nb.

2.2. Angular distributions in $pp \to Z \to \mu\mu$

The focus of this thesis is put on the angular distributions of the final state muons in the reaction $pp \to \mu^+\mu^- + X$ (Drell–Yan process). Several important quantities can be measured using the angular distributions, in particular the weak mixing angle and the spin of the gluon. The link of these quantities to the angular distributions will be given in this section.

For the reaction

$$pp \to Z/\gamma^* + X \to \mu^+\mu^- + X, \tag{2.31}$$

where X denotes additional final state particles (mostly from radiated partons), two types of Feynman diagrams exist in lowest order perturbation theory. One is the so called $2 \to 1$ process, shown in Fig. 2.6, with only leptons in the final state. Additional final state particles can be generated through initial or final state radiation. Note that the intermediate Z/γ^* will undergo a subsequent decay which is not shown in the Feynman diagrams. The other type of diagrams are so called $2 \to 2$ processes[7] involving a gluon in the initial or final state, shown in Figs. 2.7 and 2.8. The principle difference between both types of processes is that if a gluon with its spin $S = 1$ is involved in the process it may lead to transverse polarisation of the intermediate state. Furthermore, the momentum of the the final state parton, against which the Z/γ^* recoils, defines a reference plane together with the initial state partons against which the azimuthal angle ϕ of the final state lepton is defined. A transverse polarisation gives rise to a modulation of the ϕ distribution. Hence the $2 \to 2$ processes are sensitive to the spin of the gluon.

In proton–proton collisions both types of processes are present. Their relative admixture depends on the momentum transfer of the reaction as well as the PDF of the colliding protons. The general form of the differential cross section for the process of Eq. (2.31) is given as [28], [29]:

$$\begin{aligned}\frac{d\sigma}{d\cos\theta d\phi} \propto & \left(1+\cos^2\theta\right) + \frac{1}{2}A_0\left(1-3\cos^2\theta\right) + A_4\cos\theta \\ & + A_1\sin(2\theta)\cos\phi + \frac{1}{2}A_2\sin^2\theta\cos(2\phi) + A_3\sin\theta\cos\phi \\ & + A_5\sin\theta\sin(2\phi) + A_6\sin(2\theta)\sin\phi + A_7\sin\theta\sin\phi\,, \end{aligned} \tag{2.32}$$

where θ and ϕ are the polar and azimuthal angles of the final state lepton[8] in the Collins-Soper frame (CS frame), a special rest frame of the dilepton pair which is explained in section 6.1. In this thesis only 1-dimensional angular distributions are considered, as they contain all relevant information. They are obtained by integrating either over $\cos\theta$ or over ϕ:

$$\frac{d\sigma}{d\cos\theta} \propto \left(1+\cos^2\theta\right) + \frac{1}{2}A_0\left(1-3\cos^2\theta\right) + A_4\cos\theta \tag{2.33}$$

$$\frac{d\sigma}{d\phi} \propto 1 + \frac{2\pi}{16}A_3\cos\phi + \frac{1}{4}A_2\cos(2\phi) + \frac{3\pi}{16}A_7\sin\phi + \frac{1}{4}A_5\sin(2\phi). \tag{2.34}$$

The coefficients A_5 and A_7 are expected to be 0, as shown in [29]. All terms but one are symmetric in $\cos\theta$. The exception is $A_4\cos\theta$ in Eq. (2.33) which leads to a forward–backward asymmetry (A_{fb}), the magnitude of which is determined by the coefficient A_4 ($A_{fb} = \frac{3}{8}A_4$). An event is called forward if $\cos\theta \geq 0$ and backward otherwise. The forward–backward asymmetry is hence defined as

$$A_{fb} := \frac{\int_0^1 \frac{\mathrm{d}\sigma}{\mathrm{d}\cos\theta}\,\mathrm{d}\cos\theta - \int_{-1}^0 \frac{\mathrm{d}\sigma}{\mathrm{d}\cos\theta}\,\mathrm{d}\cos\theta}{\int_{-1}^1 \frac{\mathrm{d}\sigma}{\mathrm{d}\cos\theta}\,\mathrm{d}\cos\theta}\,. \tag{2.35}$$

[7] $2 \to 2$ processes are one order higher in the perturbation series of α_s as the $2 \to 1$ process and should hence be referred to as next-to-leading order (NLO) processes. However, in some literature both are denoted leading order processes. To avoid confusion they will be referred to as $2 \to 1$ and $2 \to 2$ processes in the following.

[8] All angles are given w.r.t. the negatively charged final state lepton. The positively charged lepton is not considered.

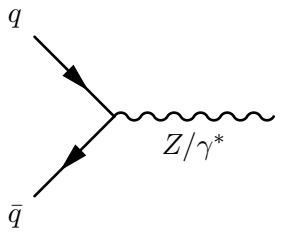

Figure 2.6.: Annihilation diagrams for Z-boson production belonging to the category of $2 \to 1$ processes.

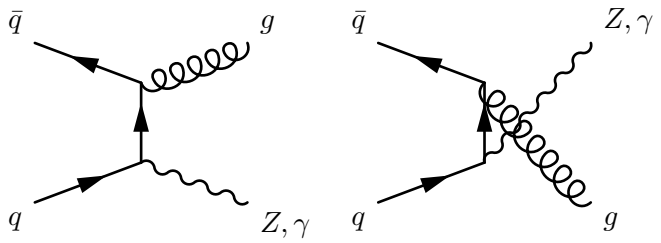

Figure 2.7.: Annihilation diagrams for Z-boson production with an additional gluon in the final state, belonging to the category of $2 \to 2$ processes.

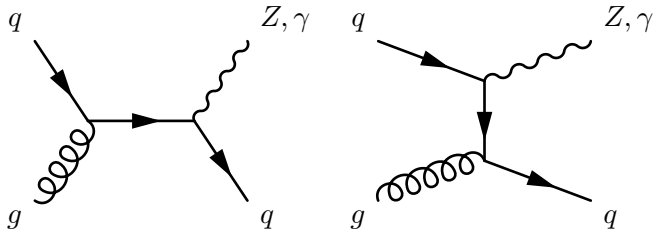

Figure 2.8.: Compton-like diagrams for Z-boson production with an additional quark in the final state, belonging to the category of $2 \to 2$ processes.

This asymmetry is sensitive to the weak mixing angle, as is shown in the following. For a specific quark flavour q in the initial state it can be calculated as

$$A_{fb}(M_{\mu\mu}, y) = \frac{3}{4}\frac{F_1^q(M_{\mu\mu}, y)}{F_0^q(M_{\mu\mu}, y)} \tag{2.36}$$

with $M_{\mu\mu}$ being the invariant mass of the dimuon pair and y its rapidity. The functions F^q are defined as

$$\begin{aligned} F_0^q &= Q_q^2 Q_l^2 + 2\,\mathrm{Re}\{\chi(M_{ll})\} Q_q Q_l g_V^q g_V^l \\ &\quad + |\chi(M_{ll})|^2 \Big((g_V^q)^2 + (g_A^q)^2\Big)\Big((g_V^l)^2 + (g_A^l)^2\Big) \qquad (2.37) \\ F_1^q &= 2\,\mathrm{Re}\{\chi(M_{ll})\} Q_q Q_l g_A^q g_A^l + 4\,|\chi(M_{ll})|^2\, g_V^q g_A^q g_V^l g_A^l\,, \qquad (2.38) \end{aligned}$$

where Q is the electric charge of the involved fermion and $g_{V,A}$ is the vector/axial vector coupling as defined in (2.25) and (2.26). χ is the Breit–Wigner amplitude of the Z resonance

$$\chi(M) = \frac{G_F m_Z^2}{2\sqrt{2}\pi\alpha} \cdot \frac{M^2}{M^2 - m_Z^2 + i\Gamma_Z M^2/m_Z}\,, \tag{2.39}$$

with G_F being the Fermi constant, α the electromagnetic coupling constant, m_Z the Z boson mass and Γ_Z its width. A derivation of the relation (2.36) is found, e.g., in [30]. The weak mixing angle enters the asymmetry via the vector coupling g_V. As all other parameters are known to a good precision the weak mixing angle can be determined by measuring the forward–backward asymmetry in the vicinity of the Z resonance. This measurement is described in section 6. In proton–proton collisions a complication arises due to the substructure of the protons. Associated with up and down quarks in the initial state are different asymmetry distributions, due to their different electric charge. To get the total asymmetry, the structure functions have to be summed over all quark flavours, appropriately weighted with the probability to find a certain quark flavour q with momentum x in the reaction with momentum transfer $Q^2 = M_{\mu\mu}^2$. Hence, all simulation predictions of the angular distributions and, in particular, the forward–backward asymmetry will depend on the PDFs.

In addition to the asymmetry the coefficients A_0 and A_2 are of particular interest, i.e. their dependence on the transverse momentum of the final state dilepton pair $p_\mathrm{T}(Z)$. The so called *Lam-Tung* relation [31] states that the coefficient functions $A_0(p_\mathrm{T})$ and $A_2(p_\mathrm{T})$ are identical for all p_T: $A_0(p_\mathrm{T}) = A_2(p_\mathrm{T})$, if the spin of the gluon equals $S(g) = 1$. In case of a scalar gluon this relation is badly broken [32]. The measurement of both coefficients and the determination of the spin of the gluon is presented in chapter 7.

Different angular distributions are expected for annihilation (Fig. 2.7) and Compton-like processes (Fig. 2.8). In the vicinity of the Z-pole the leading order prediction of the p_T dependence of $A_{0,2}$ for a gluon of $S(g) = 1$ are given by [33–35]:

$$A_{0,2} = \frac{p_\mathrm{T}^2}{p_\mathrm{T}^2 + M_{ll}^2} \qquad \text{for annihilation processes,} \tag{2.40}$$

$$\text{and} \quad A_{0,2} = \frac{5p_\mathrm{T}^2}{5p_\mathrm{T}^2 + M_{ll}^2} \qquad \text{for Compton} - \text{like processes.} \tag{2.41}$$

Calculations at NLO show corrections of up to 20% on $A_2(p_T)$, whereas A_0 remains nearly unchanged. Hence the relation $A_0(p_T) = A_2(p_T)$ is only valid to the 20% level [29].

In addition to the difference $A_0(p_T) - A_2(p_T)$ also the dependence of each coefficient A_i on the transverse momentum is of interest, since different simulation programs predict different dependences. The reason for this is that initial state gluon radiation (ISR), which is simulated by means of parton shower algorithms, has the same final state as a hard $2 \to 2$ process with a gluon in the final state. In the latter case the gluon is included in the matrix element of the hard interaction and spin effects are taken into account. Contrary, in case of ISR the radiated gluon will not alter the polarisation of the intermediate gauge bosons. Hence, the resulting angular distributions will be different. Note that this particular effect does not alter the forward–backward asymmetry. However, as angular distributions are important observables when studying new particles it is interesting to investigate which MC generators are most accurate in describing known SM processes. A comparison of various generators with the measured angular distributions is therefore presented in chapter 7.6.

3. Monte–Carlo Event Generation and Detector Simulation

Experimental observations of final state particles are often compared to predictions of theoretical models at the level of quarks and gluons (partons). To allow for such a comparison the process of interest as well as the detector response to the final state particles is simulated. This chapter presents an overview of the software tools used for event simulation, which is divided into the MC event generation, detector simulation, digitisation and, eventually, the reconstruction of the events. The event generation is discussed in the next section. An overview of the used generators is given as well. Detector simulation and digitisation (sec. 3.2) as well as the event reconstruction (sec. 3.3.1) is identical for all used generators. All MC event samples used in this thesis are listed in Tab. A.2.

3.1. Event generation

Event generators are software tools that model the complex physics processes occurring in collisions of high energy particle beams. Specialised software exists for a variety of beam types and physics processes. For hadron collisions and in particular for proton–proton collisions the event generation follows few general steps [36]. This is illustrated for a specific example in Fig. 3.1.

First, the interaction of a pair of partons originating from the incident protons is simulated. This interaction of the two initial state partons is called the *hard process*. Usually only a few hard processes of interest are simulated at a time, an example is $q\bar{q} \to Z/\gamma^* \to \mu^+\mu^-$. The partonic composition of the colliding protons is modelled by the parton density functions (PDFs). The hard process is described by a matrix element corresponding to one or several Feynman diagrams representing the parton–parton interaction. The order of the generator is defined by the power of a coupling constant present in the calculation of the matrix element. Where the most basic form of a given process is referred to as leading order (LO) process[1]. If not noted otherwise the strong coupling constant α_s is referred to in this context. The process given in the example above is hence a LO process, both in QED and QCD.

Higher order QCD effects not accounted for in the matrix element are added in the next stage of the simulation, the so called *parton-shower*. In this step all partons participating in the hard process, including the initial state partons, are allowed to split ($g \to gg$, $q\bar{q}$) or to radiate gluons ($\overleftarrow{q} \to \overleftarrow{q}g$). The resulting partons are allowed to branch again, thus leading to a whole shower of partons. This process gives rise to transverse momentum of the hard interaction. A principle difference between gluon radiation simulated in the parton shower and calculated in the matrix element of the hard interaction is that in the latter case also spin interactions and interference effects are taken into account,

[1] Note that some processes are forbidden in leading and hence only occur in higher orders.

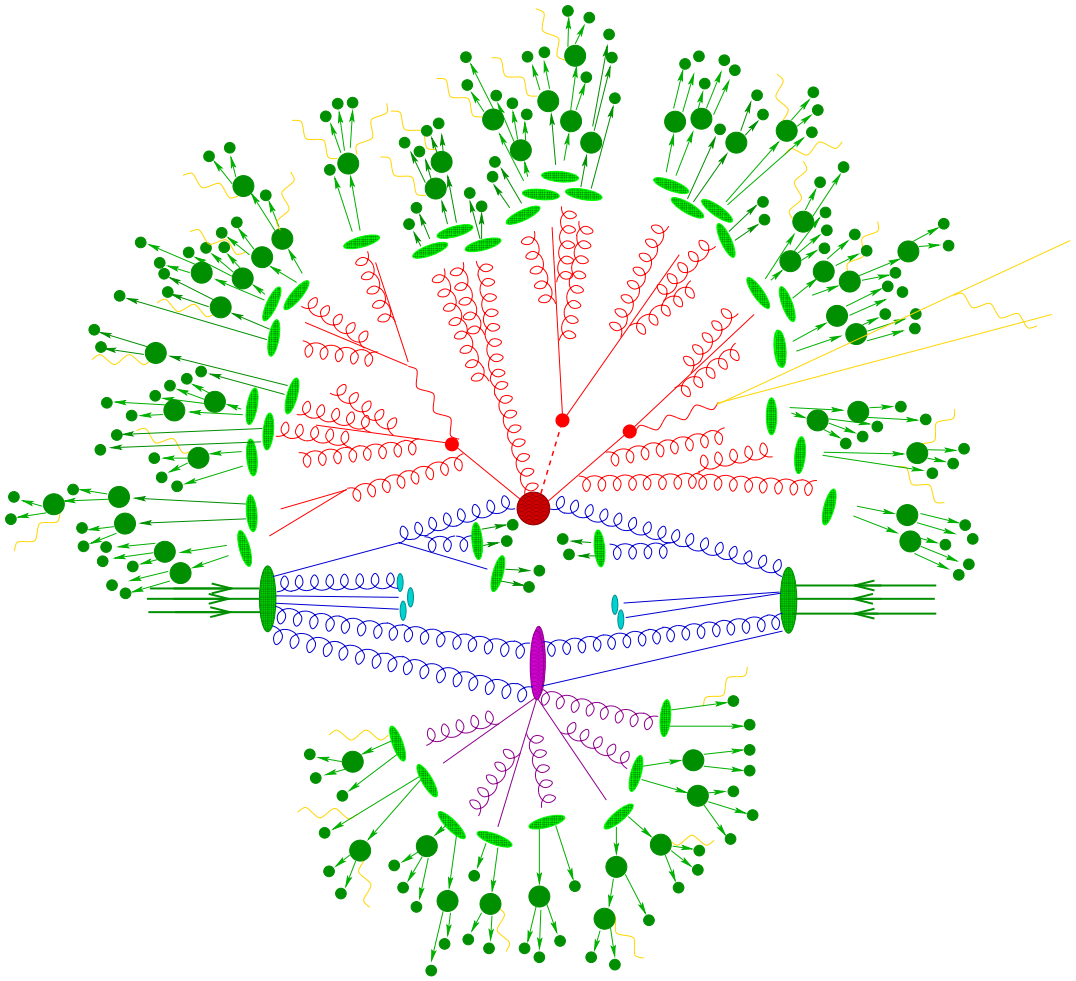

Figure 3.1.: Sketch of a proton–proton collision at high energy [37]. In the upper hemisphere of the figure partons from the initial protons (large green ellipses) radiate gluons and eventually interact in the hard interaction (red blob). The products of the hard interaction produce a parton shower, depicted in red, which eventually hadronizes (the green blobs represent hadrons) which subsequently decay into the final state particles, all shown as small green circles. The lower hemisphere of the figure depicts the underlying event, starting from some gluons radiated off the protons, which interact producing a parton shower as well (purple). Also the beam remnants, shown as light blue blobs, are considered part of the underlying event. Photon radiation occurs at all stages in the event generation (indicated as yellow lines).

which are neglected in the parton shower. Hence the angular distributions of the final state particles will be affected by the number of additional partons used in the hard process, usually defined by the order of the generator. Particularly difficult to model is the transition between the treatment of partons in the matrix element and in the parton shower. Different approaches are implemented in different generators. Also higher order radiative QED effects are modelled in electromagnetic showers. However, effects of loop diagrams can only be calculated within the matrix element but they are of less significance compared to radiative effects treated in the parton shower.

In the next step of the simulation all colored objects are combined into colorless hadrons. This procedure, called *hadronisation*, results in many short lived resonances which are subsequently allowed to decay. Finally, the colored remnants of the initial protons are allowed to interact, forming the *underlying event*.

The default event generator used in this thesis is PYTHIA [38]. However, the signal event sample has been generated using a variety of generators to allow a comparison of generators and their specific features. Background processes are simulated using a generator suitable for the process considered. All but the MadGraph simulation are processed within the ATLAS common analysis framework called *Athena*. A tuned set of parameters is applied within Athena to the generators denoted as ATLAS MC11 tune [39]. The MadGraph samples are generated (privately) with the default tune of the MadGraph package. Some details on all generators used are given in the following sections.

3.1.1. PYTHIA

PYTHIA [38] (used in version 6.4) is a general purpose LO generator, both in QCD and QED diagrams, which can be used for p–p, e–p and e^+–e^- collisions. It contains all previously described elements of the event generation process including the simulation of the underlying event. This feature is also used for the simulation of multiple collisions occurring simultaneously with the process of interest[2]. Several specific features made PYTHIA the generator of choice for this thesis:

- The running of α_{em} is taken into account.
- The value assumed for the weak mixing angle can easily be changed. This is essential for the applied method to measure $\sin^2\theta_W^{\text{eff}}$ as presented in chapter 6.
- Effects of higher order QED radiation are taken into account by the program PHOTOS [40] which is interfaced to PYTHIA.
- The PYTHIA simulation is reasonably well tuned to the measured ATLAS data in the used MC11 tune [39]. An exception is the simulation of the transverse momentum of the Z/γ^* (p_{T}^Z), which was correct in the previous tune (MC10), but not in MC11. Hence the simulated events are reweighted to follow the p_{T}^Z distribution of the MC10 tune.

Also a reweighting of the simulated events to different PDF sets is straightforward as the initial state always consists of a quark-antiquark pair. Despite all these advantages over most other generators, PYTHIA does not simulate the full angular distributions in $pp \to Z + X \to \mu^+\mu^- + X$ events correctly, as additional final state partons are

[2] Called *pileup events*.

not calculated in the matrix element of the hard process but are solely simulated in the parton shower. This shortcoming does, however, not affect the forward–backward asymmetry which is fully determined by the parity violation in Z boson production and decay.

The method to measure the effective weak mixing angle presented in chapter 6 requires the variation of the value of $\sin^2\theta_W^{\text{eff}}$ in the simulation. This parameter is directly accessible in PYTHIA. In the used ATLAS tune for PYTHIA [39] α_{em} is allowed to run and $\sin^2\theta_W^{\text{eff}}$ is fixed in all calculations to the specified value[3].

PYTHIA performs electroweak calculations within the $\overline{MS}$ renormalisation scheme [16]. The vector and axialvector couplings (g_V and g_A) are defined in this scheme as presented in Eq. (2.28). However, in the PYTHIA simulation the parameter $\sqrt{\rho}$ is set to 1 instead of its nominal value in the $\overline{MS}$ scheme, $\sqrt{\rho} = 0.9981$. As the influence of $\sqrt{\rho}$ on $\sin^2\theta_W^{\text{eff}}$ cancels, as is shown in Eq. (2.27), the determination of the weak mixing angle is not affected[4] by the slight deviation of $\sqrt{\rho}$ in the PYTHIA simulation. Hence, the determined value for $\sin^2\theta_W^{\text{eff}}$ in chapter 6 can directly be interpreted as the effective weak mixing angle.

3.1.2. AlpGEN

AlpGEN [41] is a LO generator for SM processes with a special emphasis on multijet final states. It explicitly takes helicity correlations of itermediate gauge bosons and final state particles into account, thus reproducing a more accurate description of the angular distributions than PYTHIA. Parton showers and hadronisation have to be computed by external programs. In the ATLAS setup the programs HERWIG+JIMMY [42] are used to do this.

3.1.3. HERWIG

HERWIG [43] is a general purpose event generator for SM and supersymmetric processes at hadron and lepton colliders similar to PYTHIA. Included is initial and final state radiation via its own parton shower algorithm, hadronisation and hadron decay as well as the simulation of the underlying event. It features full spin correlations between initial and final states. A major difference w.r.t. PYTHIA is the use of a different hadronisation algorithm referred to as 'cluster fragmentation'.

3.1.4. MC@NLO

MC@NLO [44] calculates the hard processes in NLO of α_s. However, concerning electroweak diagrams the calculations are in LO. Spin correlations and mass effects are included in nearly all processes. MC@NLO provides its own parton shower algorithm.

3.1.5. MadGraph

MadGraph [45] follows a different concept compared to the other generators described. In a first step the Feynman diagrams for a given, arbitrary process are created together

[3] $\sin^2\theta_W^{\text{eff}}$ is set via the configuration option *pru(102)* and the option *MSTP(8)* is set to 0

[4] Note that the influence on the forward–backward asymmetry cancels exactly only at the Z-pole. However, deviations due to higher order effects are much smaller than the precision of this analysis in the vicinity of the Z-pole.

with some source code to compute the corresponding matrix elements. In principle this can be done to any order in QED and QCD. However, with increasing order the number of diagrams rapidly grows to inconvenient levels. In a second step the generated code is used to simulate events for the requested process. PDFs can be used to model the phenomenology of the proton–proton initial states. Parton shower, hadronisation and underlying event calculations have to be carried out in external programs, e.g. PYTHIA.

As MadGraph generates code for the evaluation of the matrix elements on the fly, it is easily possible to change the properties of the participating particles (e.g. the gluon) and such the physics of the interaction. This has been utilised to predict the angular distributions for the case of a gluon with spin zero ($S(g) = 0$). This is explained in the following.

MadGraph uses different *models* when generating the Feynman diagrams. A model contains all existing particles and their properties, possible vertices in the Feynman diagrams (i.e. the interactions between particles) as well as the Lorentz structure of each allowed vertex which eventually defines the interaction of a given vertex. Finally, a set of couplings is included in the model, used to describe the strength of the allowed interactions. The MadGraph model describing the SM is used as the starting point for the construction of a model with a gluon of spin $S(g) = 0$. Two modifications are made to the original model:

1. The particle definition of the gluon is altered from $S(g) = 1$ to $S(g) = 0$.
2. Vertices containing only gluons or gluons and quarks are changed to obey the Lorentz structure of a scalar gluon. The appropriate Lorentz structure is already defined for the usage in vertices containing a scalar Higgs boson. The coupling constant used in conjunction with gluons is not altered, nor is the allowed set of vertices including gluons.

In the private simulation only the matrix elements are calculated. As no parton shower simulation is added the simulation can not describe the low transverse momentum region of the intermediate state. Hence a minimum transverse momentum of $p_{\mathrm{T}}(Z/\gamma^*) > 10\,\mathrm{GeV/c}$ is required for events simulated by MadGraph. The predictions of the angular distributions from MadGraph 5 (version 1.3.32) using this model are compared to the SM prediction and the measured angular distributions in chapter 7.

3.2. Detector simulation

The generated events are passed to the detector simulation. It simulates the physical response of long lived[5] particles traversing through and interacting with the material of the detector. For this purpose an accurate model of the ATLAS detector is implemented using the GEANT4 toolkit. The detector description includes maps of the magnetic field as well as measured misalignments of the tracking detectors. All particles are stepped through the material, calculating multiple scattering, energy loss and charge deposition in the detector material. Also nuclear reactions are simulated to obtain a realistic behaviour of particles showering in the calorimeters.

In a next step the deposited charge in the active detector elements is fed into a simulation of the readout electronics and data acquisition system of the real detector.

[5]Long lived in this context means that the particles traverse a macroscopic portion of the detector before decaying.

At this stage also noise is introduced into the simulation. Taking into account timing constraints of the real system a set of *hits* is obtained from the detector simulation which is passed to the event reconstruction software. The same software is also used for reconstructing real, measured events without any changes of settings.

The detector simulation is a very computation intensive task. Simulation of millions of events is only feasible using massive parallel computing and usually performed on the GRID [46].

3.3. Data processing and object reconstruction

Physical objects are reconstructed using identical algorithms for simulated and measured events. The measured events, however, undergo additional treatment before and after reconstruction.

Before the properties of physical objects (e.g. muons) are reconstructed from the measured data, calibration factors have to be applied to the measurements. These are determined from events routed to a dedicated stream, called *express*-stream, which is analysed immediately. Reconstruction of the rest of the measured events is started with a 36 h delay, to allow the proper determination of the calibration constants and the beam spot position and the identification of noisy detector channels. After reconstruction the quality of the obtained data is categorised in terms of *data quality flags* [47] which state if a given subdetector or reconstruction algorithm is working within normal parameters. This information is available once per luminosity-block[6]. So called good run lists (GRLs) are generated from the data-quality flags, listing all luminosity blocks fulfilling the required criteria on the detector operation for a given data taking period. These lists are used for easy preselection of useful events. Whenever a significant amount of data is collected it is processed by performance groups (e.g. the Muon Combined Performance (MCP)). They provide corrections to be applied to the simulated event samples to match their properties (e.g. energy / momentum scales, resolution and reconstruction efficiencies) to the measured data.

The reconstructed final state particles used in this thesis are exclusively muons. Some details of the muon reconstruction are discussed in the next section.

3.3.1. Muon reconstruction

Muons are measured in both tracking systems of the detector, inner detector (ID) and muon spectrometer (MS). This allows for several definitions of a muon as objects reconstructed from the measurements.

Stand-alone muon (SA): The muon trajectory is only reconstructed in the MS. The muon momentum measured in the MS is corrected for the parametrized energy loss of the muon in the calorimeter to obtain the muon momentum at the interaction point. The direction of flight and the impact parameter of the muon at the interaction point are determined by extrapolating the spectrometer track back to the beam line.

[6] The recorded data is divided into luminosity-blocks. One block usually correspond to a fixed timespan of data taking in the order of minutes.

Segment tagged muon (ST): A track in the inner detector is identified as a muon if the track extrapolated to the muon spectrometer is associated with straight track segments in the precision detectors of the MS. All track parameters are reconstructed from the inner detector measurement.

Combined muon (CB): Track reconstruction is performed independently in the ID and the MS. A track is formed from the combination of both measurements.

Calorimeter tagged muons: An ID track is identified as a muon by the characteristic energy loss in the calorimeters. This definition has a poor purity and is not used in the analyses of this thesis.

Combined muons are the muon candidates with the highest purity and are used for all analyses in this thesis. Their reconstruction efficiency is determined mostly by the probability to reconstruct a track in the MS. This probability, and hence the reconstruction efficiency, varies with pseudorapidity (η) and azimuthal angle (ϕ), mostly apparent in two regions:

- At $\eta \sim 0$ the MS is only partially equipped with muon chambers to provide space for services of the ID and the calorimeters.
- In the transition region between the barrel and the end caps at $|\eta| \sim 1.2$ only one chamber is traversed by muons in the MS due to staged end-cap chambers. Hence no stand-alone momentum measurement is available and the combined muon efficiency and resolution are reduced.

For details on the different detector regions see section 4.2.3. The drop of the reconstruction efficiency in the transition region can be recovered by using segment-tagged muons. As segment-tagged muons do not require an independent momentum measurement in the muon spectrometer also muons which cross only one layer of the MS, e.g. low p_{T} muons, are reconstructed [48].

ATLAS uses two algorithm chains for reconstructing combined and segment-tagged muons simultaneously which are labelled Staco and Muid. They follow different pattern recognition strategies, described in [49], and define the combined muon in slightly different ways [50]. In Staco it is required that the muon momentum is measured in both, the ID and the MS. The momentum of the combined muon is then calculated as the weighted average of the ID and the MS stand-alone momentum measurements. The ID dominates the momentum measurements up to $p_{\mathrm{T}} \sim 50\,\mathrm{GeV/c}$. For $50\,\mathrm{GeV/c} < p_{\mathrm{T}} < 100\,\mathrm{GeV/c}$ the ID and MS measurements have similar weight and the MS dominates the measurement for $p_{\mathrm{T}} > 100\,\mathrm{GeV/c}$. In Muid, instead of this statistical combination, a combined track fit to all muon hits in the ID and the MS is performed. This makes it possible to include also hit configurations in which no muon momentum measurement is possible in the MS alone. As a consequence, more combined muons at $|\eta| \sim 1.2$ are found in Muid than in Staco.

The analyses presented in chapter 6 and 7 will use combined Muid muons.

4. The LHC and the ATLAS detector

4.1. The Large Hadron Collider (LHC)

The LHC [2] accelerates and collides two beams of protons or heavy ions at the highest currently achievable energies. It is installed in the 27 km long circular tunnel which previously housed the Large Electron Positron Collider (LEP) at the 'Centre Européenne pour la Rechere Nucléaire' (CERN) in Geneva, Switzerland. At the design luminosity for proton operation of $10^{34}\,\mathrm{cm^{-2}s^{-1}}$, two bunches containing $1.1 \cdot 10^{11}$ protons collide every 25 ns. On average about 25 proton–proton interactions happen during the collision of two such bunches at a nominal center-of-mass energy of 14 TeV. Currently the LHC is operating at a center-of-mass energy of 7 TeV with collisions happening every 50 ns. A peak instantaneous luminosity of $8 \cdot 10^{33}\,\mathrm{cm^{-2}s^{-1}}$ is reached. In heavy ion mode, the design energy is 2.76 TeV per nucleon in case of Pb ions at an instantaneous luminosity of $10^{27}\,\mathrm{cm^{-2}s^{-1}}$. Mainly fully stripped lead atoms are used in heavy ion collisions. A schematic overview of the full accelerator complex at CERN is shown in Fig. 4.1.

First proton–proton collisions at a center-of-mass energy of 7 TeV were created end of march 2010 with an initial instantaneous luminosity of $2 \cdot 10^{27}\,\mathrm{cm^{-2}s^{-1}}$. During the operation in 2010, which was essentially devoted to the development of the machine, the instantaneous luminosity already reached $10^{32}\,\mathrm{cm^{-2}s^{-1}}$. In 2011 the operation focused on providing a large data sample for the experiments still at the same energy. About $5.6\,\mathrm{fb^{-1}}$ of proton–proton collisions have been delivered by the LHC at a peak instantaneous luminosity of $4 \cdot 10^{33}\,\mathrm{cm^{-2}s^{-1}}$ with proton bunches colliding every 50 ns.

Six experiments are installed at the four interaction points of the proton beams of the LHC. (cf. 4.1). Two general purpose detectors, ATLAS [3] and CMS [4], are designed to record as much information as is technically possible about the proton–proton collisions with the aim to look for any sign of new physics. These two are the largest experiments at the LHC. LHCb [51] is a single sided forward spectrometer specifically designed to investigate the physics of b quarks and B hadrons. ALICE [52] is designed to investigate the collisions of heavy ions. Its strength is the reconstruction of a huge number of tracks, up to several thousand, in each collision. The aim is to study exotic states of matter in very high densities, such as a quark–gluon plasma. Two smaller experiments, TOTEM [53] and LHCf [54], are placed at some distance to the interaction points to investigate particles produced at very small angles in the collisions. This is a region experimentally not accessible by the other detectors. TOTEM focuses on the measurement of the total elastic and diffractive cross section of proton–proton interactions. LHCf uses the high energy particles to study the reaction chains induced by cosmic rays in the atmosphere.

The dataset used in this thesis is recorded with the ATLAS detector during the year 2011 and corresponds in total to an integrated luminosity of $4.7\,\mathrm{fb^{-1}}$ of proton–proton collisions at a center-of-mass energy of $\sqrt{s} = 7\,\mathrm{TeV}$.

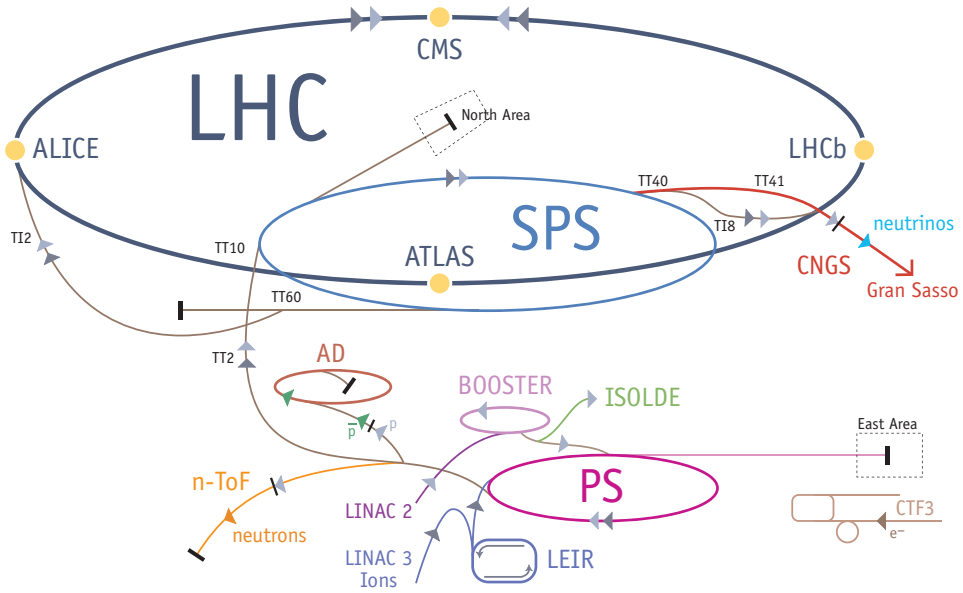

Figure 4.1.: The CERN accelerator complex [55]: Protons are fed into the LHC via a chain of accelerators: Linac2, Booster, PS and SPS. The four large experiments using the LHC are located at the interaction points of the two circulating beams, marked as yellow dots.

4.2. The ATLAS detector

ATLAS is the name of a titan from Greek mythology who carries the celestial sphere. It also is an acronym for '**A** **T**oroidal **L**HC **A**pparatu**S**' which is one of the four large experiments at the LHC and is located at the interaction point 1. The detector is designed as a general purpose instrument. As such it should be able to reconstruct all products of the proton–proton collisions, even in the high luminosity environment at the LHC with more than twenty proton–proton interactions happening simultaneously in a single collision of two bunches of protons. For this purpose the tracks of charged particles and their associated momenta have to be measured with great accuracy and a time resolution of a single bunch crossing, i.e. 25 ns, or better.

ATLAS is designed as a magnetic spectrometer following a cylindrical symmetry. All subdetectors are divided into a central part called *barrel* and a forward section on each side, called *endcap*. It features two sets of tracking detectors to measure the momenta of charged particles. One is located in the innermost region of the detector within a solenoidal magnetic field. It is referred to as inner detector (ID) (cf. sec. 4.2.1). The second one covers the outermost volume of ATLAS and is placed within a toroidal magnetic field, thus giving a completely uncorrelated momentum measurement w.r.t. the ID. This spectrometer is capable of identifying muons, as they are the only charged particles reaching this detector, and hence is called muon spectrometer (MS). It can measure momenta up to the TeV region (cf. sec. 4.2.3). Also a subdetector belonging to the ID is used for particle identification: the transition radiation tracker (TRT). It can distinguish electrons from other charged particles by means of transition radiation. Two calorimeters, an electromagnetic and a hadronic one, are placed between the ID and the MS to measure the energy of particles leaving the collision (cf. sec. 4.2.2). To be able to infer the presence of neutral particles not interacting with the detector material, e.g. neutrinos or hypothetical dark matter particles, the energy of all particles leaving the collision must be measured. Therefore the calorimeters enclose the interaction point as much as technically possible. A schematic view of ATLAS is shown in Fig. 4.2. With outer dimensions of 46 m in length and 25 m in diameter, it is the biggest detector at the LHC.

The coordinate system used in ATLAS is introduced in the following to allow the precise definition of the acceptance ranges for the individual subdetectors later on. It is aligned with the beam circulating counter clock wise, which defines the z-axis at the nominal interaction point. The x-axis points towards the center of the accelerator ring and, consequently, the y-axis upwards. The direction of a particle trajectory is parametrized by the azimuthal angle ϕ, defined as the angle between the projection of the trajectory on the $(x-y)$ plane and the x-axis, and by the polar angle θ, defined as the angle between the trajectory and z-axis. Usually the pseudorapidity $\eta = -\ln\tan(\theta/2)$ is used instead of θ. R denotes the radial distance to the nominal interaction point in the $(x-y)$ plane and ΔR is the distance in $(\eta-\phi)$ space defined as $\Delta R = \sqrt{(\Delta\eta^2 + \Delta\phi^2)}$.

The following sections discuss briefly the subsystems of the detector, based on references [3] and [56], and conclude with the trigger system presented in section 4.2.4.

4.2.1. Inner Detector

The inner detector (ID) is designed to measure the trajectory of charged particles with great precision. A particularly important task is the position determination of the col-

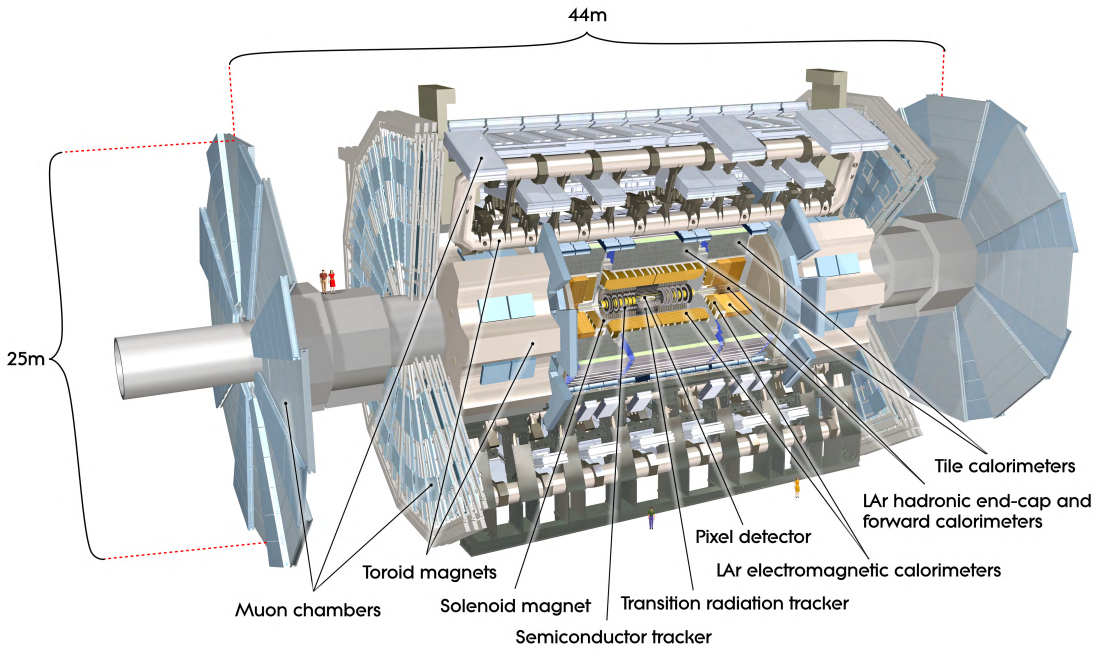

Figure 4.2.: Schematic overview of the ATLAS detector [57].

lision vertex (called primary vertex (PV)) and any secondary vertices as well as the determination of the impact parameter[1] of a particle trajectory w.r.t. a vertex. Secondary vertices occur when relatively long lived particles like τ-leptons and b-hadrons decay. The reliable reconstruction of secondary vertices is essential for the tagging of jets originating from a b-quark.

The ID itself is based on three subdetectors, all placed within a solenoidal magnetic field of 2 T oriented parallel to the beam axis. The subdetectors are arranged as cylindrical layers in the central region, and several disk or wheel like structures in the forward and backward regions. From the in- to outside the subsystems are: three layers of silicon pixel sensors (PIX), four layers of silicon strip detectors (SCT) and a straw tube tracker (TRT). In total the ID extends 6.2 m in length, 2.1 m in diameter and covers a pseudorapidity range of $|\eta| < 2.5$. For a central track with $p_{\mathrm{T}} = 5\,\mathrm{GeV/c}$ the relative resolution on the measured transverse momentum is around 1.5 % [3]. A schematic drawing of the ID is presented in Fig. 4.3. To minimise the effects of radiation on the silicon detectors they are operated at a temperature of $-5\,^{\circ}\mathrm{C}$ to $-10\,^{\circ}\mathrm{C}$. The TRT is operated at room temperature.

The Pixel detector (PIX) features 80 M readout channels, which is about 80% of the total number of readout channels in all of ATLAS. Pixels are grouped in 1744 modules à 46 k pixels each where every pixel is a readout channel. Each module is divided into 16 readout chips which are directly connected to the sensor substrate via bump-bonds in every pixel. The pixel dimensions are 50 μm times 400 μm and allow for a single hit resolution of $\sim 10\,\mu$m in the $(R-\phi)$ plane and 115 μm in z (barrel) / R (end-cap). The innermost layer has a radius of 5.05 cm, the

[1]The impact parameters denoted the minimal distance between a particle trajectory and a reference point, usually the associated vertex.

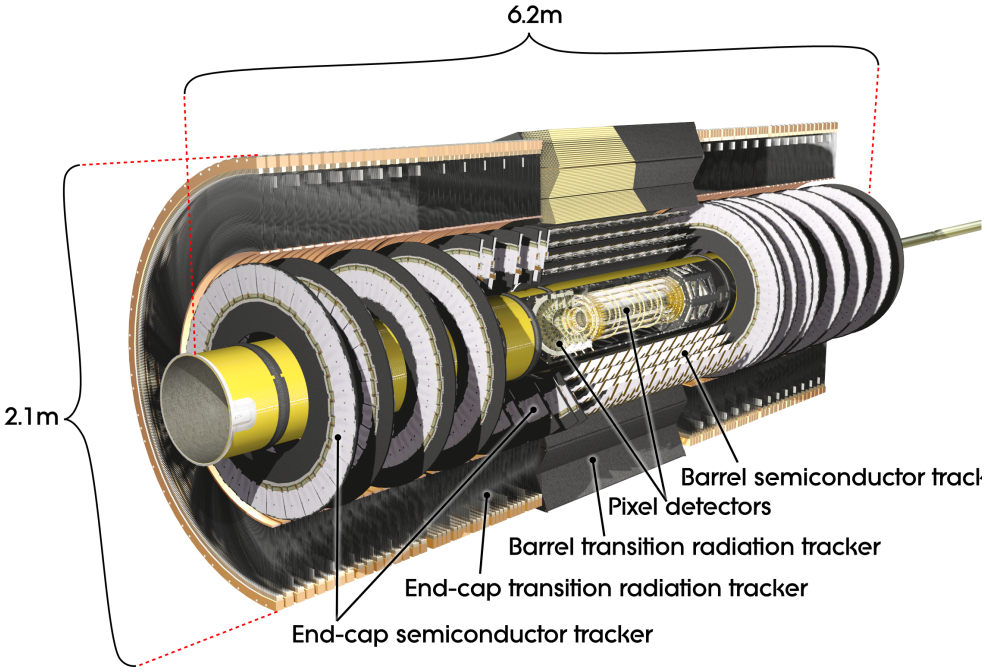

Figure 4.3.: Schematic drawing of the inner detector of ATLAS [58]. From in- to outside the subsystems are: 3 layers of silicon pixel sensors, 4 layers of silicon strip sensors and a straw tube tracker with transition radiation capability.

outermost 12.2 cm. With this layout a resolution of the vertex position of $\sim 30\,\mu$m is achieved in the transverse plane and about $50\,\mu$m in the longitudinal direction [59]. The detector can be triggered with a maximum rate of 100 kHz.

The tuning of the pixel detector is a complex task as each pixel has two individual settings, one defining the charge threshold for a hit to be recognised, and one for calibrating the charge measurement. Besides this fine tuning the coarse range of these parameters can be set individually for each readout chip. For the tuning of these approximately 160 M parameters to be completed on a reasonable time scale, a massive parallelisation of the task is necessary. This is achieved by using the processing power installed on the off-detector readout electronics, which provides around four digital signal processors per 24 detector modules. The implementation was partly done during the service work performed prior to the analysis presented in this thesis. It is documented in [60] and [61].

The Silicon Strip Detector (SCT) is divided into four barrel layers and nine end-cap disks on each side with a total of 4088 modules. Each module consists of four sensors, two being daisy chained and glued back to back to the other two providing a stereo angle of 40 mrad between them. In total each barrel module contains 786 12 cm long strips with $80\,\mu$m pitch. The strips are aligned along the beam axis which corresponds to the direction of the magnetic field. In the end-cap modules the strips are oriented radially with varying pitch over a module. With this layout typically eight measurements are provided per charged particle track with an intrinsic resolution of $17\,\mu$m in the $(R-\phi)$ plane and $580\,\mu$m in z / R.

The Transition Radiation Tracker (TRT) consists of approximately 280 k proportional drift tubes (straws) of 4 mm diameter. About 50 k axially aligned tubes with split anodes and two sided readout make up the central (barrel) part of the detector in the range $|\eta| < 1$. On both sides of the barrel nine wheel-like structures with radially oriented straws cover the range $1.0 < |\eta| < 1.96$. The layout is chosen such that a particle trajectory with $p_{\mathrm{T}} > 0.5\,\mathrm{GeV/c}$ crosses about 36 straws. This provides a continuous tracking in the TRT volume with the possibility to measure the energy loss of a particle along its path. In addition, the TRT provides electron identification via transition radiation from polypropylene fibers (barrel) or foils (wheels) interleaved with the straws. Transition radiation photons are identified by their much larger energy deposition of about 6 keV compared to the few hundred eV deposited by a minimum ionizing particle.

4.2.2. Calorimeters

The calorimeters are designed to provide a precise measurement of the energy of all particles leaving the interaction, except for neutrinos and muons which are not absorbed in the calorimeter. To be able to estimate the amount of energy escaping the detector unrecognised (E_T^{miss}), a maximum coverage of the solid angle is desirable. In ATLAS the calorimeters cover the full azimuth and the pseudorapidity range of $|\eta| < 4.9$ corresponding to $0.85° < \theta < 179.15°$. Two types of calorimeters are distinguished: the electromagnetic calorimeter used to measure the energy of photons and electrons and the hadron calorimeter used to measure the energy of hadrons. The geometrical layout of both is similar to the layout of the ID, consisting of a central barrel and end-caps. The forward calorimeters cover the pseudorapidity range of $3.1 < |\eta| < 4.9$. The design specification for the electromagnetic calorimeters states an energy resolution of $\sigma_E/E = 10\%/\sqrt{E} \oplus 0.7\%$ with E given in GeV. For the hadron calorimeters the design goal is a jet energy resolution of $\sigma_E/E = 50\%/\sqrt{E} \oplus 3\%$ in the region $|\eta| < 3.2$ and $\sigma_E/E = 100\%/\sqrt{E} \oplus 10\%$ in the forward region [3].

The electromagnetic calorimeter is a high granularity sampling calorimeter. It uses liquid argon (LAr) as active medium and accordion shaped lead plates as absorber. The accordion shape enables a constant distance between the absorber layers throughout the detector. A total thickness of more than 22 radiation lengths (X_0) is reached in the barrel part ($|\eta| < 1.8$) and more than $24\,X_0$ in the end-cap region.

The hadron calorimeter, also implemented as a sampling calorimeter, uses different technologies in different detector regions. In the barrel region plastic scintillators are used as active medium in conjunction with absorber plates made out of steel, reaching a thickness of 7.4 interaction lengths. The end-cap ($1.5 < |\eta| < 3.2$) part uses copper as absorber and liquid argon (LAr) as active material to withstand the high particle fluxes there.

The forward calorimeters ($3.1 < |\eta| < 4.9$) consist of three layers, all equipped with LAr as active material and a total thickness of 10 interaction lengths. The inner layer, primarily used as electromagnetic calorimeter, uses copper as absorber whereas the outer layers use tungsten to achieve a large absorption of stray particles.

4.2.3. Muon Spectrometer

The outer most part of the ATLAS detector is covered by a standalone muon spectrometer (MS) which accounts for most of the volume of the entire detector. It is designed to detect charge particles leaving the calorimeters and measure their momentum with a precision of 10% at a momentum of 1 TeV. The magnetic field needed for momentum measurement is created by three air-core superconducting toroidal magnet systems, one large barrel torroid and two end-cap magnets. They provide a field of about 0.5 T in the barrel region and 1 T in the end-cap region. The transition region between the barrel and the end-cap systems provides an irregular magnetic field which is a challenging situation for the momentum reconstruction.

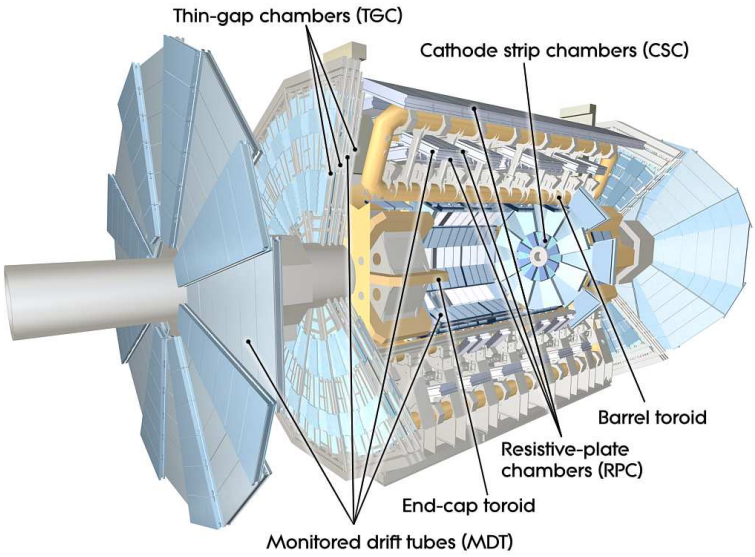

Figure 4.4.: Schematic overview of the muon spectrometer and its magnet system [62].

The detectors are separated into a barrel part ($|\eta| < 2.0$) and end-cap wheels on both sides of the barrel, covering the range $2.0 < |\eta| < 2.7$. A schematic overview of the MS is presented in Fig. 4.4. The barrel consists of three layers, the end-caps of three wheels. All barrel layers and the two outer most wheels are equipped with monitored drift tubes (MDTs) as precision detectors. The MDT chambers consist of eight layers of drift tubes operated at an absolute pressure of 3 bars. A position resolution of 80 μm per tube and 35 μm per chamber is achieved. The innermost end-cap wheels use cathode strip chambers (CSCs) instead to cope with the high particle flux. The CSCs are multiwire proportional chambers with cathode planes segmented orthogonal to the wires, thus allowing both coordinates to be measured. A resolution of 40 μm in the bending plane and 5 mm in the non-bending plane is reached. In addition all barrel layers are quipped with resistive-plate chambers (RPCs) which measure the trajectory position in the non-bending plane of the magnetic field and have fast trigger capability. The end-cap wheels use thin-gap chambers (TGCs) for the same purpose. RPCs and TGCs only cover the range in pseudorapidity up to $|\eta| < 2.4$, which is the acceptance limit of all muon triggers. All chambers exist in two widths, large and small, which are installed in alternating order (see Fig. 4.5, left).

The muon system has some holes which are needed for services to the calorimeters

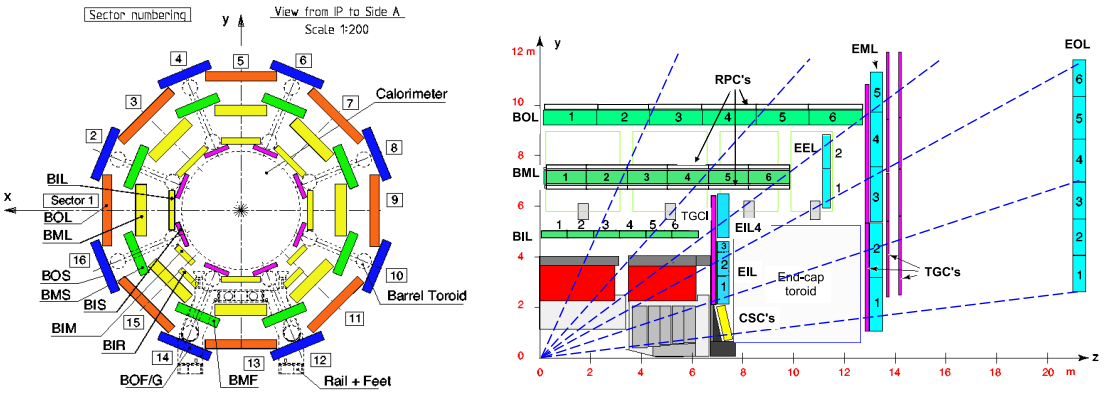

Figure 4.5.: Schematic cross section of the muon spectrometer [3]. Left: non-bending $(x-y)$ plane. Right: bending $(z-y)$ plane.

and support structures. Most pronounced are the regions around $|\eta| \lesssim 0.05$ and at the position of the detector feet. This leads to a non uniform acceptance in $(\eta - \phi)$ space. Furthermore, a varying efficiency of the muon spectrometer within its acceptance is observed due to the use of the different types of detectors as well as the different geometries of the detector modules . To account for these effects in the efficiency determination, regions in $(\eta - \phi)$ space are grouped such that they represent the geometrical configuration of the muon system. Ten different regions are defined, corresponding to ten different physical regions in the MS (see Fig. 4.6). The regions are labelled and described below:

- Barrel large: only large barrel chambers.
- Barrel small: only small barrel chambers.
- Barrel overlap: overlap between small and large barrel chambers.
- Feet: region of the feet supporting the detector; some chambers are missing in this region which makes the muon reconstruction more difficult.
- Transition: transition region between the barrel part and the end-cap wheels. Most trajectories in this region only pass two instead of three muon stations. Additionally the magnetic field has a complex geometry in this region which makes the muon reconstruction more difficult.
- End-cap small: small end-cap sectors, MDTs.
- End-cap large: large end-cap sectors, MDTs.
- BEE: sectors containing specialized MDT chambers which are mounted on top of the end-cap toroid cryostat (Barrel–endcap endcap region). In this area only part of the azimuthal range is covered.
- CSC small: small end-cap sectors, CSCs, outside TRT acceptance.
- CSC large: large end-cap sectors, CSCs, outside TRT acceptance.

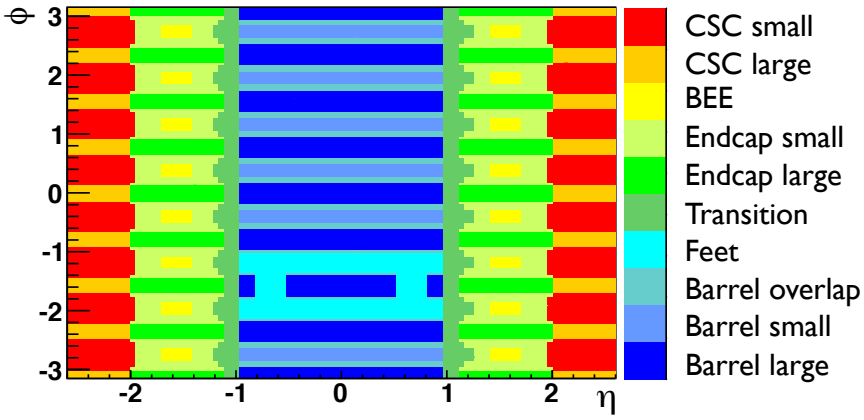

Figure 4.6.: Illustration of the detector regions defined in $(\eta - \phi)$ space. The regions correspond to the physical layout of the muon spectrometer.

To achieve a momentum resolution of better than 10% on a trajectory with a momentum of 1 TeV the sagitta of 500 μm has to be measured with an accuracy better than 50 μm. To reach this goal the position of the MDT and CSC wires along the muon trajectory have to be known to a precision better than 30 μm. For this purpose a high-precision optical alignment system is installed. Additionally, the geometry is measured in situ using dedicated alignment runs where data is recorded without magnetic field.

The efficiency measurement of the muon spectrometer is presented in more detail in chapter 5.

4.2.4. Triggering

At the design specifications of the LHC two bunches of protons collide every 25 ns, producing 25 proton–proton interactions on average. This corresponds to an event rate of about 1 GHz. But only a tiny fraction of these events contains interesting information. The maximum rate at which events can be stored to mass storage is limited to 300 Hz. Hence, a real-time selection of interesting events is necessary. This is performed by the trigger system. Event classification and selection is done in three stages which are explained in the following.

The first trigger stage, called level-1, operates at a nominal rate of 75 kHz. It only uses coarse information from fast detectors. These are RPC and TGC chambers of the muon system, calorimeter trigger towers[2], accelerator information and in special cases the TRT. Simple algorithms, implemented in custom made hardware, process these information for signs of muons, electrons, jets, missing energy and some other properties. Furthermore, momentum thresholds can be applied to these objects. Many different criteria can be defined to classify an event as interesting. Each criterion is an entrance to a trigger chain. Many chains are run in parallel to classify events in categories, already at this initial stage. Eventually, events are sorted by their classification into different so called *streams*. For example, all events passing a muon trigger end up in a specific stream.

If an event is accepted by the level-1 trigger, all subdetectors will be read out, but only in regions of interest defined by the level one trigger. The data of those regions

[2]Trigger towers are groups of calorimeter cells with varying size in $(\eta - \phi)$ space.

correspond to $\sim$ 2% of the full phase space. It is reconstructed using dedicated fast algorithms, after which information about particle trajectories and particle identification is available as well as some calorimeter based information. This information is processed by the level-2 trigger algorithms which reduces the event rate to $\sim 3.5\,\mathrm{kHz}$. The average event treatment time is 10 ms at this stage.

Events passing the level-2 decision stage trigger the read out of the full detector. They are then reconstructed completely using the standard off-line algorithms and some preliminary calibration. The fully reconstructed events are passed to the level-3 decision stage, also called event filter (EF). The large processing rate can only be achieved by the massive usage of parallel computing, as reconstruction and decision taking by the EF requires several seconds. The EF ultimately assigns events to the output streams. The acceptance rate is kept constant around 300 Hz by adjusting the prescaling[3] of trigger chains to the instantaneous luminosity.

Names of trigger chains follow the convention: <Trigger Level>_<stream>_<momentum threshold>_<optional specifications>. An example is *EF_mu_18_medium*, which corresponds to events selected by the EF with at least one muon with $p_{\mathrm{T}} > 18\,\mathrm{GeV/c}$. In this case the addition *medium* defines which level-1 seed is used, in this case *L1_mu_10* with a momentum threshold of $p_{\mathrm{T}} > 10\,\mathrm{GeV/c}$.

[3]High rate trigger chains are prescaled by a variable factor n which means that only every n^{th} event passing this trigger is recorded.

5. Measurement of the Muon Reconstruction Efficiency

When analysing processes with muon final states, it is essential to know the reconstruction efficiency of the muons. Of particular interest is the reconstruction efficiency with respect to the position of the trajectory in the detector and the momentum of the muon in question. This information is useful e.g. to spot malfunctions in the muon detectors and essential to measure differential cross sections or, in general, for precision measurements.

The reconstruction efficiencies are determined using the so-called *tag-and-probe* method on muon pairs produced in the decays of Z bosons. The idea of this method is to select events containing two muons without requiring two reconstructed muons in the event selection. An obvious candidate for such events are Z bosons decaying into two muons. They are identified in two steps. First, one (or more) well reconstructed muon(s) is required in the event. This tags the decay into muons. Then a well reconstructed track from the ID is required, which yields an invariant mass very close to the mass of the Z boson when combined with the muon. This track is called *probe*. The selected events contain only very little background. Hence, all probe tracks are assumed to be muons from Z decays. The reconstruction efficiency, w.r.t. the efficiency of the ID, is then given by the number of probe tracks which are matched to a reconstructed muon divided by all selected probes. As the ID efficiency is 1 for the considered muons, the measured efficiencies correspond to the absolute reconstruction efficiencies. The results are compared to simulation, and correction factors are provided for different geometrical and kinematic regions.

The muon reconstruction efficiency is measured using the initial collision data from the start-up phase of the LHC, in close collaboration with the ATLAS Muon Combined Performance (MCP) group, and published in [63]. It uses the data sample of proton-proton collisions recorded in 2010 at a centre of mass energy of 7 TeV, corresponding to an integrated luminosity of $42\,\mathrm{pb}^{-1}$. The efficiencies of both independent muon reconstruction algorithm chains in the prompt reconstruction of p-p collision data, Staco and Muid, are studied.

As will be explained in detail in the next sections the muon reconstruction efficiency is found to be well above 92%, as predicted by the Monte–Carlo (MC) simulation. The average scale factor (SF)[1] between experimental data and MC simulation for combined muons from Z boson decays is found to be 0.9806(31) for Staco and 0.9918(28) for Muid. Differentially in the transverse momentum (p_{T}), deviations from the average are within one standard deviation. Studying the efficiency w.r.t. different detector regions reveals three distinct regions where the efficiencies measured in the recorded data are significantly lower than expected from the simulation. In the transition region both reconstruction algorithms show lower efficiencies than expected. In the feet and BEE

[1] SF is defined as the ratio of an efficiency in simulation and data, and is commonly used in physics analyses to correct the simulation to match the conditions found in data.

regions[2] only Staco is affected. More details are given later in this chapter.

Results from the tag-and-probe efficiency determination are used in all physics groups analysing muon final states. For this purpose the MCP group provides up-to-date efficiencies with the increasing amount of recorded data. All further studies presented in this thesis use the efficiency SFs which are determined from the data sample used in the corresponding study.

In the following sections the muon reconstruction and the tag-and-probe method is explained. The method is then applied to simulated and experimental data, including a discussion of systematic uncertainties on the efficiency measurements.

5.1. The tag-and-probe method

In general, tag-and-probe refers to the method of tagging an object, e.g. an event, which fulfils certain properties, in order to allow a prediction of some sort. Once tagged, it can subsequently be probed if the prediction is true. This approach is commonly used to determine efficiencies of all kinds. In the particular case considered here, the goal is to select events containing a muon, without requiring this muon to be identified as a muon and without introducing any bias on the muon reconstruction. This is best achieved using events where a Z boson decays into two muons. These events are selected by requiring one well reconstructed muon and one charged particle track measured by the ID which must yield an invariant mass close to the Z boson mass when combined with the muon. Furthermore, both tracks must have opposite charges. The ID track is the *probe*. It is tagged as a muon by the selection of a Z decay topology in addition with a well reconstructed muon (called *tag*) in the final state. All tag muons are required to trigger the data acquisition to avoid any bias caused by other triggers. The reconstruction efficiency is determined from the fraction of probes which are reconstructed as muons divided by the number of all selected probes. This results in a relative efficiency measurement w.r.t. the efficiency of the ID. As the latter one is 100% within less than 1% statistical uncertainty [64] all obtained efficiencies are taken to be absolute. The tag-and-probe method is well established and in [49] it is shown that it reproduces the efficiency in simulated $Z \to \mu\mu$ events correctly.

Due to the limited size of the used data sample some bins in the efficiency spectrum have low statistics. To avoid unphysical results, especially concerning the calculated uncertainties, the efficiencies are calculated with the Bayesian approach for a binomial distribution using a minimally informative (flat) prior. Flat prior means that a priori all efficiencies in the interval $\varepsilon \in [0 : 1]$ are equally probable [65]. Accordingly, the efficiencies are calculated as:

$$\varepsilon_{\text{reco}} = \frac{\#\text{ successful matches } + \ 1}{\#\text{ trials } + \ 2}.$$

Note that the addends +1 and +2 enter due to the use of a Bayesian ansatz.

5.2. Selection of tag-and-probe pairs

The cut based selection is performed in three steps: selection of collision events, tag selection and probe selection. These steps are discussed in the next subsections. A detailed overview of all cuts is given in table 5.1.

[2] See section 4.2.3 for details on the detector regions.

All tracks considered in the analysis must have a minimum number of hits in the silicon detectors. Within the geometrical acceptance of the TRT a successful extension of the muon trajectory into that detector is enforced by requirements on the numbers of TRT hits associated to the track and TRT outliers. TRT outliers appear in two forms in the track reconstruction: as drift tube signals without a near-by track or as a set of TRT measurements which fail to form a smooth trajectory together with the Pixel and SCT measurements. These quality cuts suppress fake tracks and discriminate muons from hadrons.

5.2.1. Collision event selection

To ensure the event is a p-p collision at least one reconstructed primary vertex with at least three associated tracks is required. Only events are considered where the ID and MS, including their magnet systems, have been fully operational. This information is provided on a per luminosity block basis in so called GRL provided by the Data Quality Group, see also section 3.3. Events must furthermore pass the muon trigger with the lowest available transverse momentum threshold which was unprescaled. The p_{T} threshold of the trigger was well below the p_{T} threshold of the tagged muon in the analysis.

5.2.2. Tag muon selection

Tags are defined as combined muons, separately for each of the two reconstruction chains. A combined muon has to pass the following cuts:

- ID track quality criteria listed in table 5.1 applied on the ID track associated with the combined muon,
- transverse momentum (p_{T}) greater than 20 GeV/c,
- $|\eta| < 2.4$, limited to the acceptance of the muon trigger system,
- longitudinal distance from primary vertex $|z_0| < 10\,\mathrm{mm}$,
- additional muon quality requirements are imposed to remove a part of the background from decays in flight:
  - χ^2 of the MS-ID match lower than 150 for 5 degrees of freedom,
  - if the momentum measured in the MS (p^{MS}) is below 50 GeV/c, the difference between p^{ID}, the momenta measured in the ID, and p^{MS} normalized by p^{ID} must be larger than -0.4,
- trigger of the data acquisition,
- isolation: $\sum p_{\mathrm{T}}(\Delta R < 0.4)/p_{\mathrm{T}}(\mathrm{muon}) < 0.2$ (with $\Delta R := \sqrt{\Delta\eta^2 + \Delta\phi^2}$), where the sum extends over all charged particle track momenta within a cone of 0.4 around the tag, excluding the charged particle track on which the tag is based.

The muon quality requirements are applied only for Staco which has had a looser selection of combined muon candidates during the commissioning phase with 2010 pp collision data. Note that these cuts are no longer needed with the Staco configuration used in 2011.

5.2.3. Probe selection

Probes are defined as tracks measured by the ID which pass the following criteria:

- ID track quality criteria listed in table 5.1,
- p_{T} greater than $20\,\mathrm{GeV/c}$,
- $|\eta| < 2.5$, limited to the coverage of the ID,
- longitudinal distance from primary vertex $|z_0| < 10\,\mathrm{mm}$,
- isolation: $\sum p_{\mathrm{T}}(\Delta R < 0.4)/p_{\mathrm{T}}(\mathrm{muon}) < 0.2$, where the sum extends over all charged particle track momenta within a cone of 0.4 around the probe, excluding the probe itself,
- associated with the same vertex as the tag,
- azimuthal distance between tag and probe tracks $\phi > 2.0$,
- the invariant mass of the tag-and-probe pair is close to the nominal Z boson mass: $|m_{\mathrm{Z}} - m_{\mathrm{TP}}| < 10\,\mathrm{GeV/c^2}$,
- probe and tag oppositely charged.

5.2.4. Probe - Muon matching

After selecting all tag-and-probe pairs an attempt is made to match the probe tracks to muons in the event. A match is considered successful if both have the same measured charge and are close in (η, ϕ) space: $\Delta R \leq 0.01$.

Collision Event Selection	
Data quality	muon Good Run List [48]
Primary Vertex with $\geq$ 3 tracks	$\geq$ 1
ID Hit Requirements for all Tracks	
ID Si hit requirement	number of pixel hits $\geq$ 1, SCT hits $\geq$ 6
TRT hit requirements: $\lvert\eta\rvert \leq 1.9$	hits + outliers > 5 & $\frac{\text{outliers}}{\text{hits+outliers}} < 0.9$
TRT hit requirements: $\lvert\eta\rvert > 1.9$	if (hits + outliers > 5): $\frac{\text{outliers}}{\text{hits+outliers}} < 0.9$
Tag Selection	
Kinematics	$p_{\mathrm{T}} \geq 20\,\mathrm{GeV/c}$ & $\lvert\eta\rvert \leq 2.4$ & $\lvert z_0\rvert < 10$ mm
Isolation	$\sum_{\text{tracks}} p_{\mathrm{T}}^{ID} \,/\, p_{\mathrm{T}} < 0.2$ inside cone of 0.4 around tag
Muon Quality (only Staco)	$\chi^2_{\text{match}} < 150$
	if ($p^{\mathrm{MS}} < 50\,\mathrm{GeV/c}$): $\frac{p^{\mathrm{MS}} - p^{\mathrm{ID}}}{p^{\mathrm{ID}}} > -0.4$
Trigger:	
Period A-D	$p_{\mathrm{T}} > 10\,\mathrm{GeV/c}$ at level 1
Period E-F	$p_{\mathrm{T}} > 10\,\mathrm{GeV/c}$ at the Event Filter
Period G-H	$p_{\mathrm{T}} > 13\,\mathrm{GeV/c}$ at the Event Filter
Period I	$p_{\mathrm{T}} > 13\,\mathrm{GeV}$ at the Event Filter
Probe Selection	
Kinematics	$p_{\mathrm{T}} \geq 20\,\mathrm{GeV/c}$ & $\lvert\eta\rvert \leq 2.5$ & $\lvert z_0\rvert < 10$ mm
Isolation	$\sum_{\text{tracks}} p_{\mathrm{T}}^{ID} \,/\, p_{\mathrm{T}} < 0.2$ inside cone of 0.4 around probe
Charge	$\text{charge}_{\text{Tag}} \cdot \text{charge}_{\text{Probe}} < 0$
$\Delta\phi$(Tag, Probe)	> 2.0
Invariant mass	$\lvert m_{\mathrm{Z}} - m_{\mathrm{TP}}\rvert < 10\,\mathrm{GeV/c}$
same vertex as Probe	$\lvert z_{0_{\text{Tag}}} - z_{0_{\text{Probe}}}\rvert < 3$ mm
Probe - Muon matching	
ΔR	< 0.01
Charge	same

Table 5.1.: Summary of all cuts used in the efficiency measurement to select the tag-and-probe pairs and to match probes to muons. The measured data is divided in periods A–I with similar beam conditions and the p_{T} threshold of the trigger is adjusted accordingly.

5.3. Expectations from Monte–Carlo simulation and background estimation

Many physics analyses compare their results to predictions from MC simulation. Here the deviation of the reconstruction efficiency found in the measured data compared to the simulated one is of interest rather than the absolute efficiency. For this reason scale factors are calculated, defined as the ratio between the efficiencies in data and MC simulation. Furthermore simulated event samples are used to estimate the influence of background processes on the efficiency measurement, which is discussed in the following.

The MC samples used for these studies are generated with PYTHIA [38] using the *ATLAS MC09* tune [66]. In these samples only a single interaction is simulated per bunch crossing. Six background channels were considered: $Z \to \tau\tau$, $W \to \mu\nu$, $W \to \tau\nu$, and production of $b\bar{b}$, $c\bar{c}$, and $t\bar{t}$ pairs. For the two QCD background channels a scale factor of 0.58 is applied to the generator cross section. This factor is measured in [67].

The background events can be split into two categories:

- Cat. 1: Events in which the probe track is a muon. These background events do not bias the efficiency measurement.

- Cat. 2: Events in which the probe track is not a muon. These events lead to an apparently reduced muon reconstruction efficiency. The measured reconstruction efficiency has to be corrected for the rate of these events.

The number of all probe tracks and those which are reconstructed as a muon are calculated from the simulated $Z \to \mu\mu$ signal and each of the six considered background samples individually. The obtained numbers are summed, weighted by the integrated luminosity of the corresponding sample, and eventually used to calculate the reconstruction efficiency $\varepsilon_{\text{reco}}$ including the background (bg) effects. The influence of bg on $\varepsilon_{\text{reco}}$ is calculated by subtracting the efficiency obtained from the simulated signal sample alone.

If only the signal sample is considered, the efficiency is independent of the muon p_{T} in the region under study. In the different detector regions (see Fig. 5.1), the combined muon efficiencies vary between 90% and 98% in Staco and between 96% and 99% in Muid. Only the barrel regions equipped with large muon chambers show a lower efficiency of only 92%. These areas suffer most from the gap in the muon system around $\eta \approx 0$ [3] which reduces the acceptance of the muon system. If the region $|\eta| < 0.1$ is excluded from the efficiency calculation the measured efficiency in the barrel regions rises significantly. However, current physics analyses do not remove the central η region in their event selection. Hence, this cut is not considered further in the efficiency determination.

When background contamination is taken into account, the calculated efficiency is lowered by $\sim$ 1% in total. The efficiency results for signal only and signal plus bg are shown in Fig. 5.1. The drop in the efficiency is most pronounced in the low p_{T} bins, as displayed in Fig. 5.1 (c, d). To quantify the impact of category 2 background events from different processes on $\varepsilon_{\text{reco}}$, the number of probe tracks which are not reconstructed as a muon are compared to the number of probes in the $Z \to \mu\mu$ signal sample. The obtained fractions are summarized in table 5.2.

Overall the contamination of the selected event sample with background events is only 0.7%, which is small but not negligible, in particular as the background contributions from charm and bottom decays, referred to as QCD events, are mainly found for low

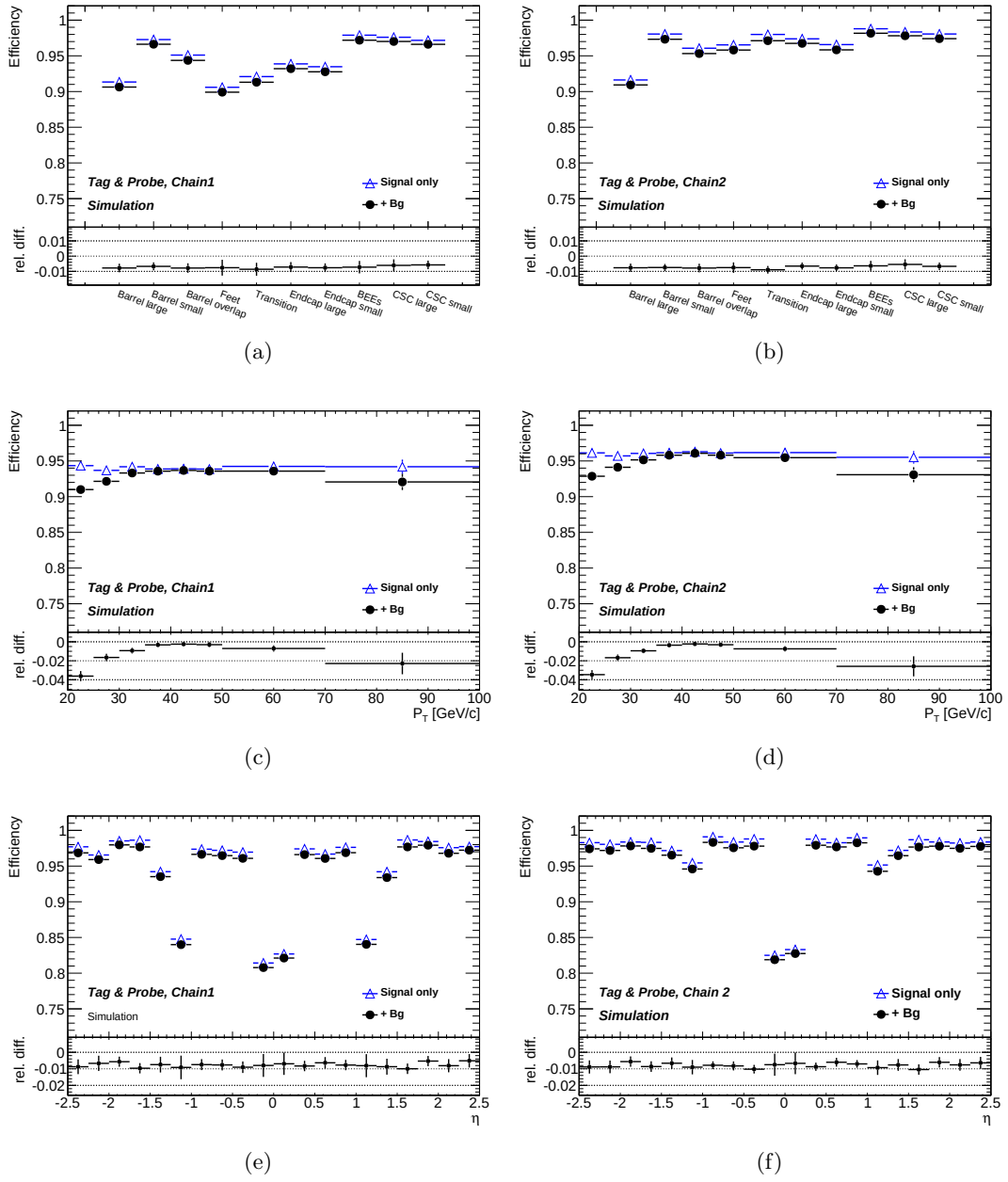

Figure 5.1.: Efficiencies for combined muons, determined from simulated events, are presented differentially w.r.t. detector region (a, b), transverse momentum (p_{T}) (c, d) and pseudorapidity (η) (e, f) of the muon for the reconstruction algorithms Staco (left) and Muid (right). Triangles correspond to signal only. Black dots correspond to signal plus all studied background contributions.

bg channel	$Z \to \tau\tau$	$W \to \mu\nu$	$W \to \tau\nu$	$b\bar{b}$	$c\bar{c}$	$t\bar{t}$	Total
cat. 2 bg fraction [%]	0.02	0.30	0.07	0.22	0.08	0.03	0.72

Table 5.2.: Fraction of category 2 bg events in the final data sample after all selection cuts.

muon p_{T}. As a consequence the measured efficiency drops significantly towards lower p_{T}. The largest background contributions are due to W, b and c decays.

A cross check on the amount of simulated background events has been made by selecting like-charge tag-and-probe pairs. In simulation 91 $\pm$ 6 and in data 75 $\pm$ 9 pairs have been found. The ratio of like-charge to opposite-charge tag-and-probe pairs agrees very well between simulation (0.38%) and data (0.40%).

5.4. Results on experimental data

The muon reconstruction efficiencies are determined using the full proton-proton data sample recorded in 2010. The data corresponds to $42\,\mathrm{pb}^{-1}$ for which the MS and ID are fully operational and is divided into nine data taking periods, labeled A-I, of approximately one month length each. These coincide with periods of similar beam conditions in the LHC.

5.4.1. Efficiencies for combined muons.

Fig. 5.2 shows the efficiency for combined muons as a function of p_{T} and detector region for data and simulation. The simulation includes all background channels listed in the previous section. The scale factor defined as the ratio between data and Monte–Carlo is displayed in the lower panel of each plot. It is on average 0.9806 ± 0.0024 for Staco and 0.9918 ± 0.0020 for Muid, where the errors are only statistical. The largest deviation is found to be in the transition region with a scale factor of 0.902 for Staco and 0.971 for Muid. For Staco also the feet and the BEE region show significantly lower efficiencies compared to the simulation with scale factors of 0.959 and 0.958, respectively. These efficiency drops are understood to arise from a poor alignment in both areas. The efficiency drop in the transition region is attributed to the limited accuracy of the magnetic field map used in the first-pass reconstruction of the ATLAS data in this region, which leads to a small mis-measurement of the standalone muon momentum. The efficiency drops can be recovered by using muons which are tagged by only one muon station as is described in detail in the next section.

The scale factors determined in bins of p_{T} while averaging over η and ϕ agree within 1.5 standard deviations with the average scale factor of the algorithm in question. Hence it is sufficient to only consider the dependence on the different detector regions when applying the scale factors in a physics analysis. The background corrected efficiencies for combined muons are shown in Fig. 5.3. The background is estimated from Monte–Carlo, as described in the previous section. It is subtracted for every bin individually. Tab. 5.3 summarises the background corrected efficiencies measured from data for the different data taking periods. The efficiencies as a function of time agree within the statistical uncertainties.

	Period	A-D	E	F	G	H	I
CB	$\varepsilon_{\mathrm{Muid}}$	0.946(19)	0.950(8)	0.960 (6)	0.945(4)	0.955(4)	0.955(2)
	$\varepsilon_{\mathrm{Staco}}$	0.933(21)	0.896(10)	0.916(7)	0.919(5)	0.922(4)	0.925(3)
CB+ST	$\varepsilon_{\mathrm{Muid}}$	0.971(15)	0.985(5)	0.987(4)	0.979(3)	0.977(3)	0.980(1)
	$\varepsilon_{\mathrm{Staco}}$	0.971(15)	0.976(7)	0.974(5)	0.977(3)	0.974(3)	0.978(2)

Table 5.3.: Background corrected reconstruction efficiencies for individual data taking periods. For each chain and muon definition the efficiency is consistent with being stable over the full run period. The statistical errors are shown in brackets.

5.4.2. Efficiencies for combined plus segment tagged muons.

The capability to recover a part of the muon efficiency in the difficult detector regions[3] by means of segment tagging is studied by measuring the efficiency for combined plus segment-tagged muons [63][4]. The tag-and-probe method described in section 5.1 is used with the only difference that the probe is matched to a combined or segment-tagged muon. As combined muons are also reconstructed as segment-tagged muons, combined muons which are rejected by the additional quality cuts[5] for Staco enter the combined plus segment-tagged muon sample as tagged muons. Fig. 5.4 shows the gain in efficiency when using segment-tagged muons in addition to the combined muons. The largest gains are in the feet (12 %) and transition (18 %) regions of the detector for Staco. For the Muid algorithm the gain is 3 % in the feet and 5 % in the transition region. In Fig. 5.5 the efficiency for combined plus segment-tagged muons measured from data is compared to the MC expectations and scale factors are derived. The scale factors for combined plus segment-tagged muons are 0.9990(16) for Staco and 1.0006(15) for Muid after background correction. The increase of the scale factor compared to the ones for combined muons only is 1.8 %for Staco and 0.9 % for Muid.

5.5. Systematic uncertainties

Background contributions and the finite resolution of the detector lead to systematic uncertainties. Contributions from the latter are estimated by varying the selection cuts when determining the efficiency from Monte–Carlo. The cuts on the mass window around the Z mass and the cut on the transverse momentum of the tag are each varied within their resolution. Other cuts are varied by ± 10 % representing a conservative estimate on their precision. The resulting change in the scale factors is quoted as systematic uncertainty. The amount of simulated background is varied by ± 10 % and the resulting differences in the scale factors are considered as additional systematic uncertainties. A variation of ± 10 % is chosen as it corresponds to the statistical uncertainty of the measurement of like-charge tag-and-probe pairs presented in section 5.3. Furthermore, the uncertainty of the measurement of electro-weak and QCD background contributions in [68] also state an uncertainty of ~ 10 %.

The systematic uncertainties on the total scale factors for combined muons are summarised in Tab. 5.4. The individual systematic uncertainties are considered to be uncorrelated and are added in quadrature to obtain the total systematic uncertainty. For values which result from an up- and downward variation the larger value is quoted and used. The largest deviation arises from the variation of the mass window followed by the variation of the background contamination and the variation of the probe isolation.

As the same tag-and-probe selection is used for the measurement of the CB+ST muon efficiency, the same systematic uncertainties are expected for the corresponding scale factors.

[3] Feet, transistion and BEE region

[4] Results obtained by E. Le Ménédeu in collaboration with the MCP group

[5] The Staco quality cuts (cf. sec. 5.2) are necessary to suppress secondary muons from decays in flight which are picked up by Staco in 2010 data. These cuts are no longer needed with the improved configuration of Staco in 2011.

Cut	Variation	absolute difference of SF from nominal	
		Staco SF = 0.9806	Muid SF = 0.9918
Probe isolation	0.2 → 0.18	0.0009	0.0009
Mass window	$10\,\mathrm{GeV/c^2}$ → $8\,\mathrm{GeV/c^2}$	0.0014	0.0013
$\Delta\phi$	2.0 → 2.2	0.0003	0.0003
p_{T}(tag)	$20\,\mathrm{GeV/c}$ → $22\,\mathrm{GeV/c}$	0.0006	0.0006
Probe TRT outlier frac.	0.9 → 0.7	0.0001	0.0001
MC Background	+ 10%	0.0007	0.0008
Total		**0.0020**	**0.0019**

Table 5.4.: Contributions to the total systematic uncertainty in the CB muon efficiency measurement. For the total uncertainty only the largest deviation of an upward/downward variation is considered. The individual uncertainties are treated as fully uncorrelated and are added in quadrature.

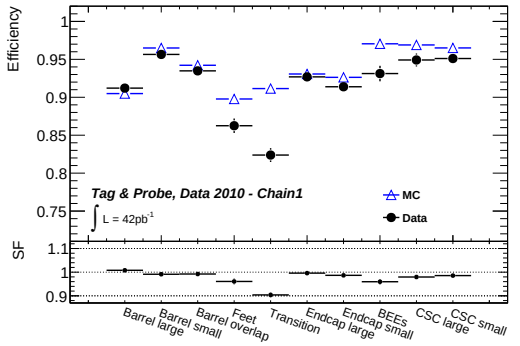

(a) Staco efficiency in different detector regions

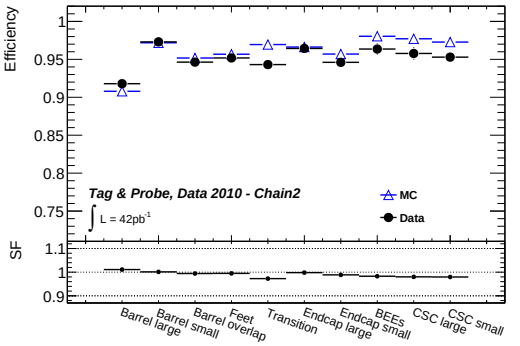

(b) Muid efficiency in different detector regions

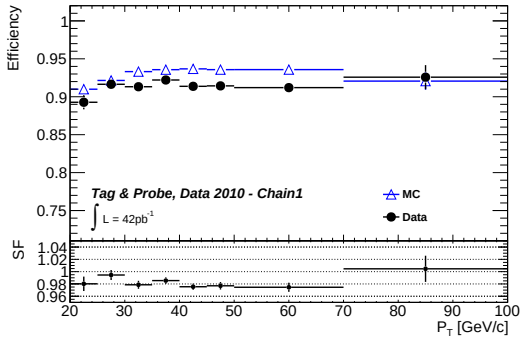

(c) Staco efficiency as a function of $p_{\mathrm{T}}(\mu)$

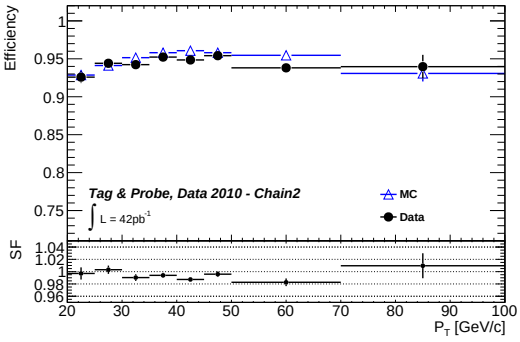

(d) Muid efficiency as a function of $p_{\mathrm{T}}(\mu)$

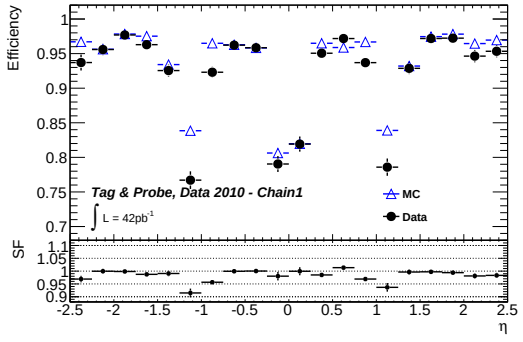

(e) Staco efficiency as a function of $\eta(\mu)$

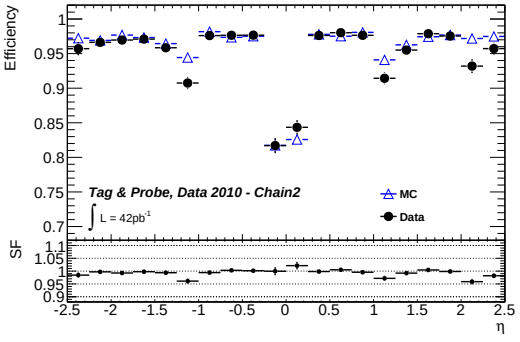

(f) Muid efficiency as a function of $\eta(\mu)$

Figure 5.2.: Reconstruction efficiencies and scale factors for combined muons. The efficiency for the two reconstruction chains Staco (left) and Muid (right), obtained from data (dots) and Monte–Carlo (open triangles) including backgrounds, are shown in the upper part of each figure. The corresponding scale factors (SF) are shown in the lower part.

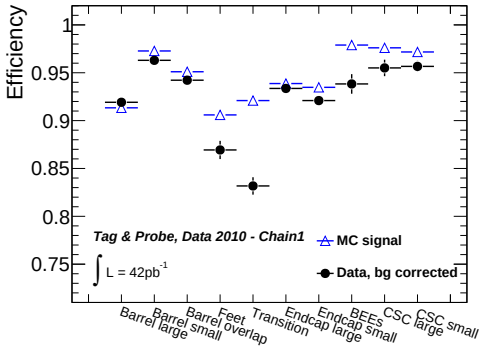

(a) Staco efficiency for the different detector regions

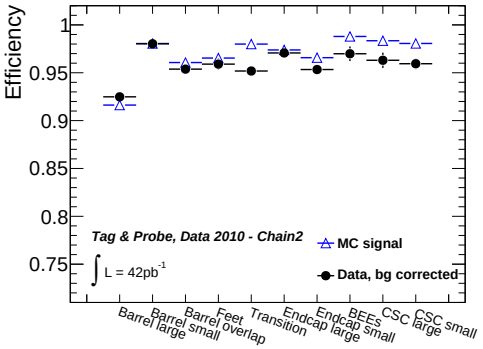

(b) Muid efficiency for the different detector regions

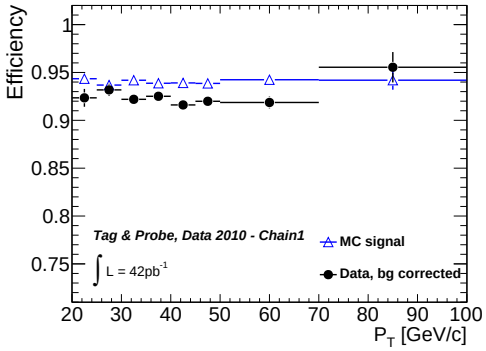

(c) Staco efficiency as a function of $p_{\mathrm{T}}(\mu)$

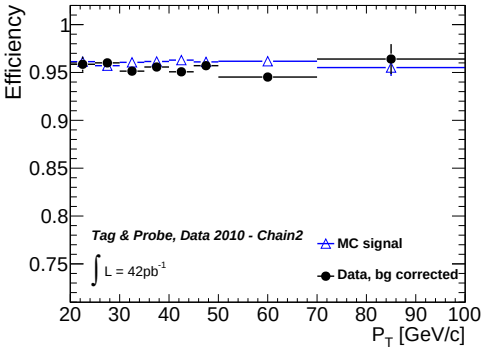

(d) Muid efficiency as a function of $p_{\mathrm{T}}(\mu)$

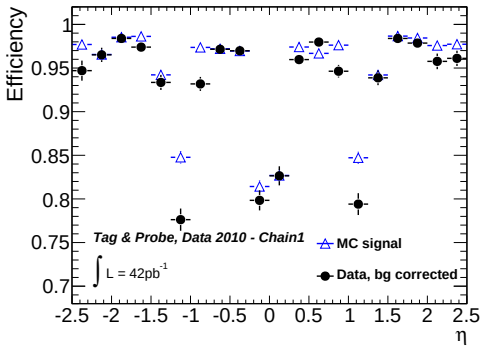

(e) Staco efficiency as a function of $\eta(\mu)$

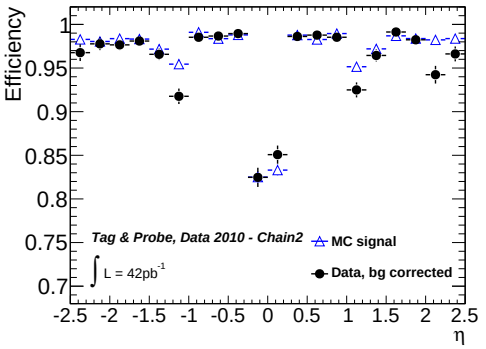

(f) Muid efficiency as a function of $\eta(\mu)$

Figure 5.3.: Background corrected efficiencies for combined muons for the two reconstruction chains Staco (left) and Muid (right), obtained from data (dots) and Monte–Carlo (open triangles).

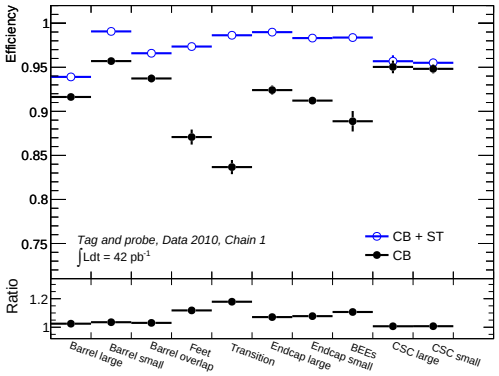

(a) Staco efficiency for the different detector regions

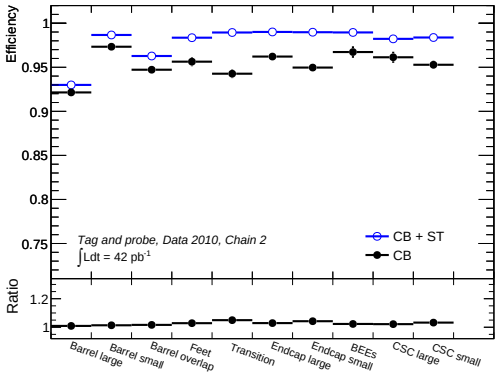

(b) Muid efficiency for the different detector regions

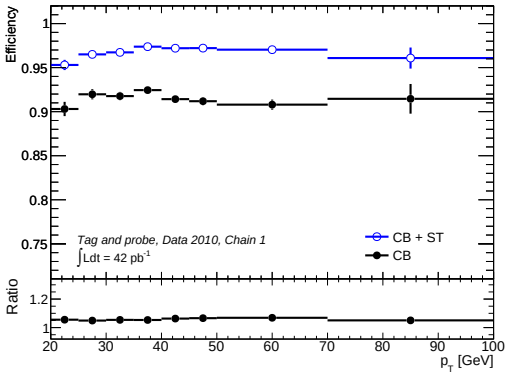

(c) Staco efficiency as a function of $p_{\mathrm{T}}(\mu)$

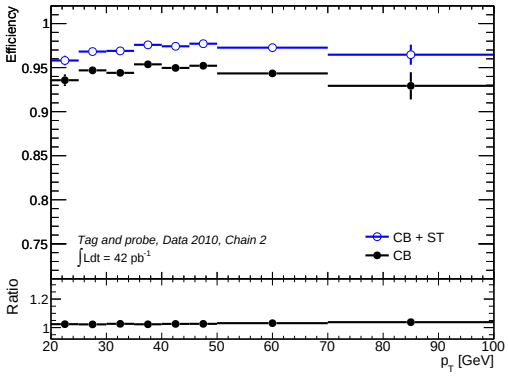

(d) Muid efficiency as a function of $p_{\mathrm{T}}(\mu)$

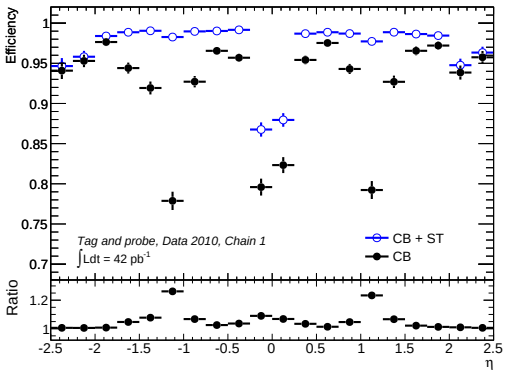

(e) Staco efficiency as a function of $\eta(\mu)$

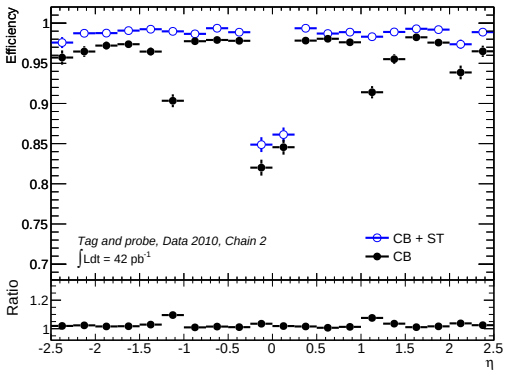

(f) Muid efficiency as a function of $\eta(\mu)$

Figure 5.4.: Efficiencies for combined plus segment-tagged muons (open circles) in comparison to those for combined muons only (dots) for the two reconstruction chains Staco (left) and Muid (right). The relative gain is shown in the lower part of each figure.

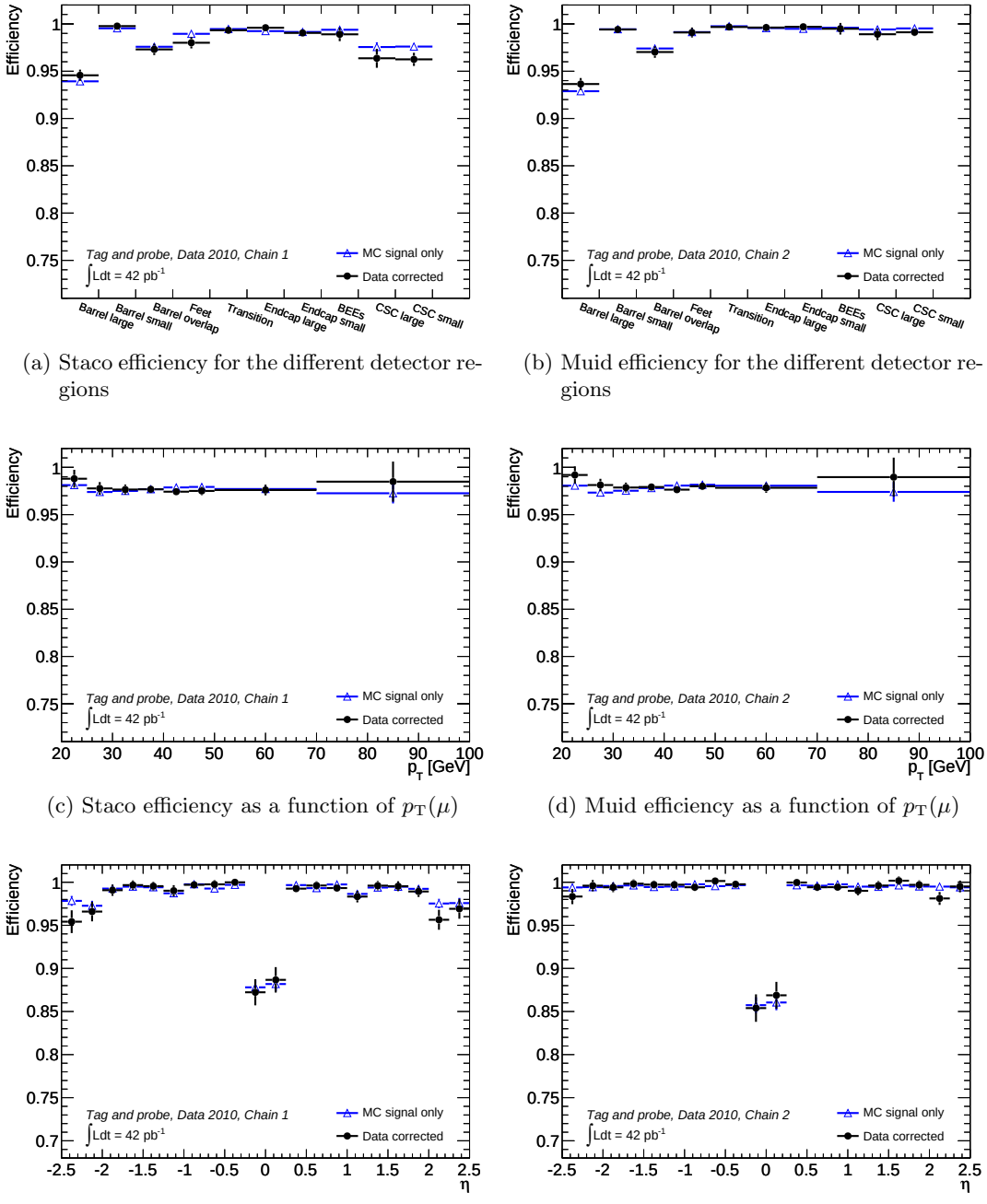

(a) Staco efficiency for the different detector regions

(b) Muid efficiency for the different detector regions

(c) Staco efficiency as a function of $p_{\mathrm{T}}(\mu)$

(d) Muid efficiency as a function of $p_{\mathrm{T}}(\mu)$

(e) Staco efficiency as a function of $\eta(\mu)$

(f) Muid efficiency as a function of $\eta(\mu)$

Figure 5.5.: Efficiencies for combined plus segment-tagged muons for the two reconstruction chains Staco (left) and Muid (right), obtained from data with background correction (dots) and Monte–Carlo of the signal (open triangles).

6. Measuring the Weak Mixing Angle in $pp \to Z/\gamma^* \to \mu\mu + X$

In the electroweak process $q\bar{q} \to Z/\gamma^* \to l^+l^-$ leptons are expected to exhibit a forward-backward asymmetry with respect to the quark direction in the rest frame of the dilepton pair. This is due to the parity violating properties of the electroweak interaction as explained in section 2.2. The magnitude of the asymmetry depends on the mass of the intermediate state and the weak mixing angle $\sin^2\theta_W^{\text{eff}}$. The asymmetry can therefore be used to measure the weak mixing angle. The method and the details of the analysis are is described in this chapter.

The differential cross section for the parton-level process in lowest order can be cast into the form

$$\frac{\mathrm{d}\sigma}{\mathrm{d}\cos\theta} = \frac{\pi\alpha^2}{2s}\left[F_0^q(1+\cos^2\theta) + 2F_1^q\cos\theta\right], \tag{6.1}$$

where $\sqrt{s}$ is the center-of-mass energy of the incoming partons and θ is the angle between the lepton (l^-) and the incoming quark in the rest frame of the dilepton system. F_0^q and F_1^q are defined in (2.37) and (2.38), respectively. The linear term in $\cos\theta$, while giving a null contribution to the integrated cross section, causes an asymmetry between the number of forward ($\cos\theta > 0$) and backward ($\cos\theta < 0$) events which is defined as

$$A_{fb} = \frac{\int_0^1 \frac{\mathrm{d}\sigma}{\mathrm{d}\cos\theta}\,\mathrm{d}\cos\theta - \int_{-1}^0 \frac{\mathrm{d}\sigma}{\mathrm{d}\cos\theta}\,\mathrm{d}\cos\theta}{\int_{-1}^1 \frac{\mathrm{d}\sigma}{\mathrm{d}\cos\theta}\,\mathrm{d}\cos\theta} = \frac{3}{4}\frac{F_1^q}{F_0^q}. \tag{6.2}$$

The dependence of the asymmetry on the weak mixing angle (cf. Fig. 6.1) is found in the definition of the vector coupling $g_V^f = I_3 - q^f\sin^2\theta_W^f$ which is used in the functions F_0^q and F_1^q. Consequently, the measurement of the forward-backward asymmetry (A_{fb}) measures the couplings of the electroweak interaction. In addition, several scenarios of physics beyond the Standard Model, e.g. additional Z bosons [69], predict a deviation of A_{fb} from its SM value.

Several methods exist to extract the weak mixing angle in the considered reaction. The three most often used ones are:

1. An unbinned maximum likelihood fit using the full event information and leaving (at least) $\sin^2\theta_W^{\text{eff}}$ as free parameter. Since it exploits the maximum amount of information present in each event, this approach should theoretically reach the highest sensitivity. However, all detector effects as well as the PDFs have to be modelled correctly in the likelihood function which is a very complex task with non trivial impact on the resulting uncertainties. Hence, this method has been discarded in this thesis.

2. The theoretical prediction of the asymmetry spectrum can directly be fitted to the measured asymmetry spectrum after correcting it for detector effects with $\sin^2\theta_W^{\text{eff}}$ being a free parameter in the fit. This method might be the most obvious one but

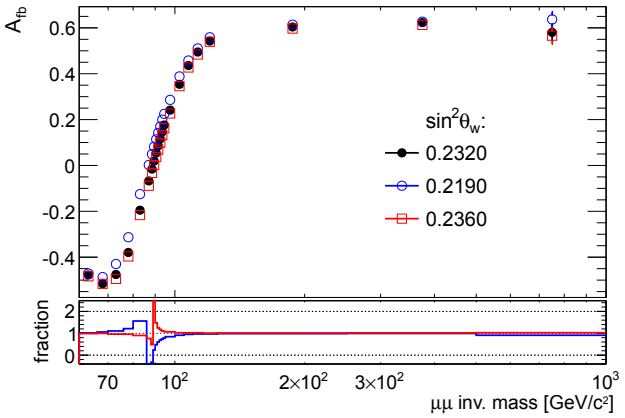

Figure 6.1.: Forward–backward asymmetry versus invariant $\mu\mu$ mass for three different values of the weak mixing angle. Simulated events without detector simulation are used to obtain the presented distributions. Fractions of the shown distributions w.r.t. a nominal weak mixing angle of 0.232 are shown in the lower canvas.

it has two disadvantages. The dependence of the asymmetry on the invariant $\mu\mu$ mass depends on the quark flavour in the initial state. Hence, the fraction of up-type to down-type quarks participating in the reaction has to be fitted along with the weak mixing angle, leading to larger uncertainties compared to a single free parameter. This could be avoided by constraining the fit to a very small region in the vicinity of the Z-peak where the asymmetry is fairly independent of the flavour composition. This, however, reduces significantly the available statistics. In addition, the unfolded[1] A_{fb} spectrum is needed. The unfolding procedure has to correct for acceptance and dilution[2] effects which reduce the asymmetry to 20% of its original value. This leads to additional uncertainties due to the large corrections needed and introduces a strong dependence on the MC simulation.

3. Templates of the asymmetry versus invariant $\mu\mu$ mass distribution are constructed from simulated event samples for various values of $\sin^2\theta_W^{\text{eff}}$. The value of the weak mixing angle present in the measured data is obtained by comparing the simulated distributions to the measured one. This method has the advantage of being easily controllable. Furthermore, no corrections to data have to be applied, a broad mass range can be used and $\sin^2\theta_W^{\text{eff}}$ is the only free parameter. However, also this method relies on a correct description of the asymmetry by the simulation and may hence depend on the chosen MC event generator.

In this thesis method 3 is used to extract the weak mixing angle. First, the reference frame used for the measurement of $\sin^2\theta_W^{\text{eff}}$ will be discussed in the next section, followed by the detailed presentation of method 3 in sec. 6.2. Further sections present the cross check of the statistical uncertainty (sec. 6.3), the event selection procedure (sec. 6.4), corrections applied to MC simulated events (sec. 6.5), background evaluation (sec. 6.6), study of systematic uncertainties (sec. 6.7) and eventually the final results (sec. 6.8).

[1] 'unfolding' names the procedure of removing all experimental effects from the measured data.
[2] *Dilution* is explained in section 6.1.1.

6.1. The Collins-Soper reference frame

In order to study the angular distribution of the lepton pairs from Z/γ^* decays w.r.t. the incoming partons, a suitable reference frame must be defined. To be sensitive to the underlying physics process in the reaction a rest frame of the intermediate Z/γ^* state is chosen. Non trivial is the definition of the polar (or z) axis relative to which the polar angle of the final state lepton shall be measured. Since the Z/γ^* origins from a $q\bar{q}$ annihilation, a natural choice would be the direction of the q. Without transverse momentum this coincides with the proton direction, i.e. the beam axis. Of course, it remains a priori unknown which of the colliding protons contained the quark and which the antiquark. This induces an ambiguity regarding the positive direction of the z-axis which can not be resolved event–wise. It can, however, be estimated on a statistical basis, as is described in sec. 6.1.1.

If significant transverse momentum of the Z/γ^* is observed the q and $\bar{q}$ are not collinear any more. In this case also the initial proton momenta p_1 and p_2 are not collinear in the Z/γ^* rest frame. But as the initial state quark (i.e. before gluon radiation) still is collinear with its parent proton, the proton momenta in the Z/γ^* rest frame are used to define a suitable coordinate frame. However, if the Z/γ^* system has transverse momentum the polar axis can not be determined unambiguously as it can not be inferred which of the initial protons (or partons) underwent gluon radiation. To minimize the effect of this lack of knowledge, the polar axis is defined in the rest frame of the intermediate state such that it is bisecting the angle between the momentum of one of the incoming protons and the inverse of the momentum of the second one. To complete the coordinate system the y-axis is defined as the normal vector to the plane spanned by the two incoming protons. In case of zero transverse momentum the direction of the y-axis is arbitrary. Finally, the x-axis is chosen such that a right handed Cartesian coordinate system is obtained. This specific reference frame is called Collins-Soper frame (CS) [70]. It is illustrated in Fig. 6.2.

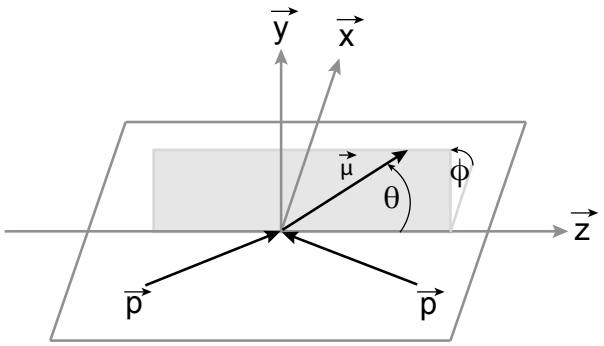

Figure 6.2.: The Collins-Soper frame is a rest frame of the Z/γ^* system. The polar axis ($\vec{z}$) is defined as the one bisecting the angle between the direction of one of the incoming protons and the inverted direction of the other proton. The $\vec{y}$-axis is defined as the normal vector to the plane spanned by the incoming proton momenta and the $\vec{x}$-axis is chosen to set a right handed Cartesian coordinate system with the other two axes. Polar and azimuthal angles are calculated w.r.t. the outgoing lepton (μ^-) and are labeled θ and ϕ, respectively.

The transformation into the CS frame is implemented in the analysis in the following way.

1. The incoming proton momenta are defined in the general form (p_x, p_y, p_z, E) as $p_1 = (0, 0, E_B, E_P)$ and $p_2 = (0, 0, -E_B, E_P)$ with E_B being the beam energy of 3.5 TeV and $E_P = \sqrt{E_B^2 + M_p^2}$ the proton energy with the rest mass of the proton, M_P.

2. Proton and lepton momenta are boosted into a rest frame of the lepton pair.

3. Now the coordinate axes are constructed using the boosted proton momenta:
   - $\vec{z} = \hat{p_1} - \hat{p_2}$
   - $\vec{y} = \hat{p_1} \times \hat{p_2}$
   - $\vec{x} = \vec{y} \times \vec{z}$

4. The angles are calculated as:
   - θ_{CS} = angle between the lepton (μ^-), boosted into the dilepton rest frame, and $\vec{z}$.
   - $\phi_{CS} = \mathrm{Arg}\,(\vec{p_\mu} \cdot \vec{y} + i\vec{p_\mu} \cdot \vec{x}) + \pi$

In order to determine the sign of $\cos(\theta_{CS})$ the direction of the incoming quark needs to be known. As mentioned above, in pp collisions there is in principle no way of knowing to which of the two beams the quark belonged and to which the anti-quark. However, one can gain some insight into the quark direction by observing the longitudinal boost of the resulting lepton pair in the laboratory frame. This is explained in the next section.

6.1.1. Dilution of the forward–backward asymmetry

The orientation of the reference axis, relative to which the polar angle in the CS frame is determined depends on the direction of the incoming quark. As it is a priori not known from which proton the (anti-) quark originates, also the sign of $\cos(\theta_{CS})$ is undetermined. If it were completely arbitrary, this would spoil any sensitivity to A_{fb} in this variable. However, the quark direction can be inferred on a statistical basis.

In pp collisions the antiquark must originate from the quark sea, whereas the quark in the reaction can be a valence quark. Using the fact that statistically valence quarks carry a larger momentum fraction of the proton momentum compared to sea quarks (cf. Fig. 2.5) a statistical sensitivity to the sign of $\cos(\theta_{CS})$ can be restored. This is achieved by observing the longitudinal direction of the Z/γ^* system in the lab frame which is likely to coincide with the direction of the incoming quark. This information is used to fix the direction of the polar axis[3] (i.e. the sign of $\cos\theta_{cs}$) in the following way:

$$\mathrm{sign} = \frac{p_z^{ll}}{|p_z^{ll}|}\,.$$

The sensitivity to the sign of $\cos(\theta_{CS})$ depends on the rapidity of the dilepton system which is illustrated in Fig. 6.3. For vanishing rapidity all sensitivity is lost while a sensitivity of 1 is asymptotically reached with increasing y. The reduction of the measured

[3] In fact the sign of E_B in the definition of p_1 and p_2 (sec. 6.1) are set according to the determined sign.

magnitude of A_{fb} compared to the true asymmetry in this context is called *dilution*. The impact of the dilution on $\cos(\theta_{CS})$ and A_{fb} is shown in Fig. 6.4. A rapidity averaged dilution factor of 0.17 is obtained in studies using the PYTHIA MC signal sample[4] within the acceptance of the detector.

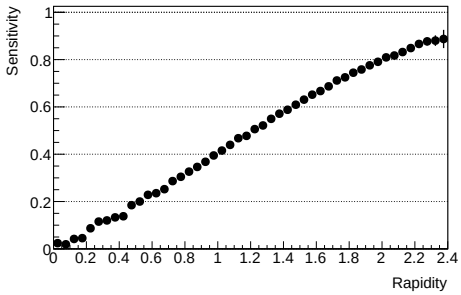

Figure 6.3.: Sensitivity to the sign of $\cos(\theta_{CS})$ in dependence on the rapidity of the dilepton system. The sensitivity, which is defined as $[(\#\{\text{sign estimate correct}\} - \#\{\text{sign estimate wrong}\}) \,/\, \#\{\text{all events}\}]$, is calculated within the geometrical acceptance of the detector which limits the rapidity to $|y| \leq 2.4$. Detector effects are excluded in the calculation.

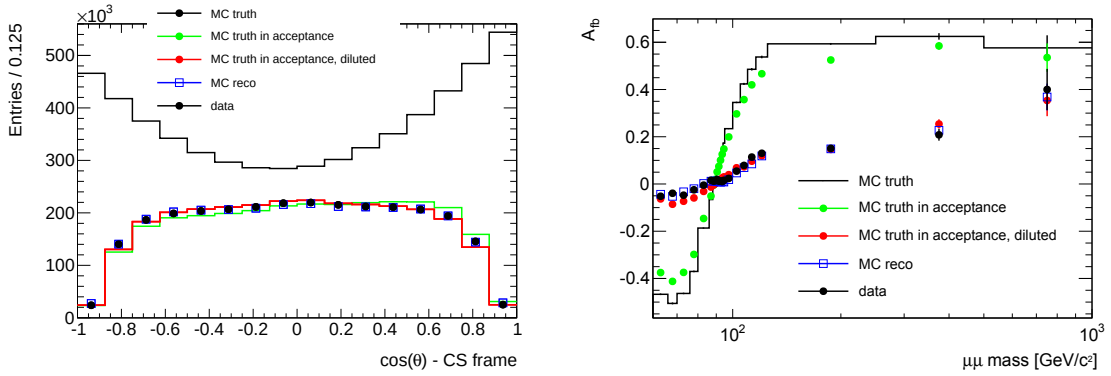

(a) (b)

Figure 6.4.: Influence of finite acceptance, dilution and detector effects on $\cos(\theta)$ (left) and A_{fb} (right). Shown are the simulated distributions without detector simulation in the full phase space (MC truth, black line), within the acceptance of the analysis (MC truth in acceptance, green line), with dilution added on top (diluted, red line), after detector simulation (MC reco, blue open squares) and the measured distributions (data, black dots). The largest distortion of the $\cos\theta$ distribution originates from the limited acceptance of the detector, whereas the largest reduction of the A_{fb} is due to dilution.

[4]See app. A Tab. A.2 for details on the MC samples.

6.1.2. Gluons in the initial state

The definition of the polar axis of the CS frame is explained above. If reconstructed events are used, the procedure is identical for measured data and for simulation. However, if the truth information of simulated events is used, some thought has to be given to the case of gluons in the initial state. This is the case for Compton-like processes (cf. section 2.2, Fig. 2.8), where the initial state is composed of a gluon g and a quark q or antiquark $\bar{q}$. Each vertex in Fig. 2.8 involving a gluon and two quarks is interpreted as gluon splitting ($g \to q\bar{q}$) or quark antiquark annihilation ($q\bar{q} \to g$). Hence, if the initial state comprises a gluon and a quark, the quark momentum orientation is taken as the reference in the construction of the polar axis. If instead a gluon and an antiquark are present in the initial state, the orientation of the gluon momentum is used as a reference.

6.2. The template method for extracting $\mathbf{sin^2\theta^{eff}_W}$

In this approach simulated event samples, each generated with a different value of $\sin^2\theta^{\text{eff}}_W$, are compared to the measured data. The best match between simulation and measurement reveals the weak mixing angle. All information on $\sin^2\theta^{\text{eff}}_W$ is found in the forward–backward asymmetry and its dependence on the mass of the $Z/\gamma*$ system. Hence the A_{fb} versus invariant $\mu\mu$ mass distribution is used for this comparison. No corrections need to be done to the measured data which is the advantage of this approach. However, it is crucial that the Monte–Carlo simulation describes the underlying physics processes as well as the detector response accurately. Any discrepancy potentially biases the measurement of the weak mixing angle. This, however, also holds for the other methods mentioned before. Great care has therefore been given to the study of any differences found between the MC and the measured data distributions, as discussed in section 6.5. As it turns out, this analysis is particularly sensitive to various kinds of misalignment within the tracking system of the detector. Several discrepancies between the description of the alignment in the MC simulation and the real situation present in the data have been uncovered, both in the inner detector (ID) and in the muon spectrometer (MS). These issues are discussed in section 6.7.2. Remaining influences due to alignment uncertainties are considered as systematic uncertainty and are well under control. All systematic studies are presented in section 6.7 and the final results in section 6.8. The method itself is described in detail in the next section.

6.2.1. The method in detail

A schematic overview of the method is shown in Fig. 6.5. The goal is to construct $A_{fb}(m_{\mu\mu})$ curves based on different values of $\sin^2\theta^{\text{eff}}_W$ including all detector effects in the simulation and compare the simulated with the measured A_{fb} distributions. However, the simulation of events including the full detector simulation is highly time consuming and not feasible on the scale of several 100 M events needed for this analysis. Therefore a dedicated method has been implemented to reweight the existing MC events, which include the detector simulation, to different values of $\sin^2\theta^{\text{eff}}_W$.

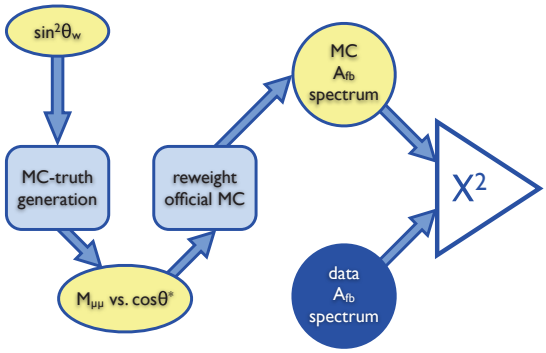

Figure 6.5.: Schematic overview of the extraction of the weak mixing angle using MC templates.

Within the region of interest, i.e between $0.217 \leq \sin^2\theta^{\text{eff}}_W \leq 0.236$, 20 MC data sets are generated containing 14 M events each. Truth information (without detector

simulation) is generated using the PYTHIA 6.4 event generator [38]. To be compatible with other ATLAS data sets the official *Evgen.trf* job transformation from the MC11 [39] simulation campaign is used. This ensures that the ATLAS specific generator tune is set. The only varied parameters are the weak mixing angle and the used PDF set for systematic studies. Note that changing the weak mixing angle leaves m_Z unchanged in the simulation (cf. Fig. 6.6). For details on how PYTHIA handles the weak mixing angle see section 3.1.1.

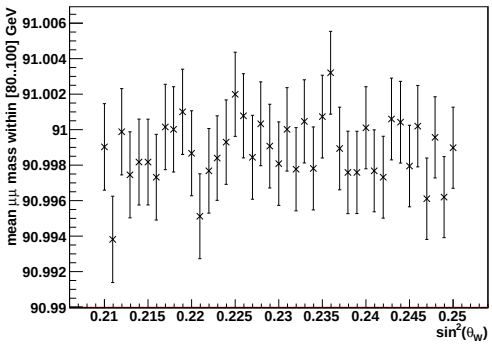

Figure 6.6.: Truth mean $\mu\mu$ invariant mass in the mass range $80\,\mathrm{GeV/c^2}$ to $100\,\mathrm{GeV/c^2}$ for different values of $\sin^2\Theta_W$. No systematic change of the Z mass wrt. $\sin^2\theta_W^{\mathrm{eff}}$ is visible.

From the newly generated MC samples the decay angle $\cos(\theta_{CS})$ and the invariant mass of the di-muon pair ($m_{\mu\mu}$) are filled into a two dimensional histogram, called *target* histogram. The number of entries in one bin is labelled $target_{ij}$, i, j denoting the bin number in m_{ll} and $\cos\theta_{CS}$, respectively. Another histogram is filled from the truth information of the default PYTHIA signal sample, called the *reference* histogram. The number of entries in one bin of this histogram is labelled ref_{ij}. Weights describing the difference between the reference and each of the target distributions are calculated in every bin as $w_{ij} = target_{ij}/ref_{ij}$. Target and reference histograms are normalised to the same number of entries before calculating the weights. These weights are then applied to the PYTHIA MC signal events which include the detector simulation, in order to obtain a fully simulated dataset for each of the different values of $\sin^2\theta_W^{\mathrm{eff}}$. These datasets are referred to as *reweighted* datasets in the following.

From the reweighted datasets the A_{fb} spectrum is compared to the measured one in a χ^2 test. The χ^2 value of each comparison is calculated as:

$$\chi^2 = \sum_{i=1}^{N} \frac{(data_i - MC_i)^2}{\sigma(data_i)^2 + \sigma(MC_i)^2 + \sigma(sys_i)^2}. \tag{6.3}$$

where $\sigma(data_i)$ and $\sigma(MC_i)$ represent the statistical uncertainties on the asymmetry in the i-th mass bin for the measured and simulated event samples, respectively. $\sigma(sys_i)$ is the systematic uncertainty in the i-th mass bin (cf. sec. 6.7). The statistical uncertainty in one bin is calculated as

$$\sigma = \frac{2}{(f+b)^2}\sqrt{(f\cdot\delta b)^2 + (b\cdot\delta f)^2} \tag{6.4}$$

with the number f (b) of forward (backward) events and the corresponding uncertainties δf (δb). For data distributions Gaussian errors are assumed, i.e. $\delta f_{data} = \sqrt{f}$. In this case Eq. (6.4) can be written as $\sigma = \sqrt{(1 - A_{fb}^2)/N}$. For the MC samples the uncertainty on the weights needs to be taken into account. The uncertainty for a single weight is calculated as

$$\delta w_{ij} = \sqrt{\left(\frac{\delta target_{ij}}{ref_{ij}}\right)^2 + \left(\frac{target_{ij} \cdot \delta ref}{{ref_{ij}}^2}\right)^2},\ \delta target_{ij} = \sqrt{target_{ij}},\ \delta ref_{ij} = \sqrt{ref_{ij}}. \tag{6.5}$$

The uncertainty of bin i of the reweighted distribution is obtained by adding the statistical uncertainty $\bar{w}\sqrt{n}$ and the uncertainty due to the weights $\sum \delta w$ in quadrature:

$$\delta f_{MC} = \sqrt{\left(\sum_{k=1}^{n} \delta w_k\right)^2 + \left(\bar{w}\sqrt{n}\right)^2} \tag{6.6}$$

with n being the number of events, w_k the weight of event k and $\bar{w}$ the average weight of events in the corresponding bin. As the summed weights are highly correlated their uncertainties are added linearly.

When plotting the obtained χ^2 values versus the value of $\sin^2\theta_W^{\text{eff}}$ used in the simulation a parabolic shape is obtained. Its minimum corresponds to the most probable value of $\sin^2\theta_W^{\text{eff}}$ in the measured data. It is determined by fitting a second order polynomial to the χ^2 distribution,

$$\chi^2(x) = a + b \cdot (x - c)^2, \tag{6.7}$$

where c corresponds to the minimum. The statistical uncertainty is given by $\sigma = \sqrt{1/b}$, which equals the width of the χ^2 parabola at $\chi^2_{\text{min}} + 1$ [71]. The obtained uncertainty is a composition of statistical components from the data and the simulated event samples. They are disentangeled by using either only the data or MC uncertainty in Eq. 6.3. The statistical uncertainty originating purely from the data sample is quoted as statistical uncertainty of the measurement. The contribution due to the finite MC statistics is included in the systematic uncertainty of the measurement, cf. section 6.7.

To verify the proper implementation of the analysis a so called *closure test* is performed. For this purpose the simulated event sample, with known weak mixing angle $\sin^2\theta_W^{\text{eff}} = 0.232$, is used as input to the analysis. The true $\sin^2\theta_W^{\text{eff}}$ of the event sample is recovered: $\sin^2\theta_W^{\text{eff}} = 0.23287 \pm 0.00056$, with $\chi^2_{\text{min}}/\text{ndf} = 0.1$. The corresponding χ^2 parabola is shown in Fig. 6.7. The $\chi^2_{\text{min}}/\text{ndf}$ is much smaller than 1 as the templates are generated from the same simulated event sample which is also used as data input. However, some statistical component is introduced due to the reweighting of the template distributions to different values of $\sin^2\theta_W^{\text{eff}}$, which explains why extracted and true values do not equal exactly but differ marginally.

6.3. Verifying the statistical uncertainty

The calculation of the statistical uncertainty has been verified in two ways. In each case the measured data is used as a starting point:

1. In a so called sub-sample test the available measured data has been divided into 30 disjunct subsets of 55 k events each and the analysis is performed on each sample.

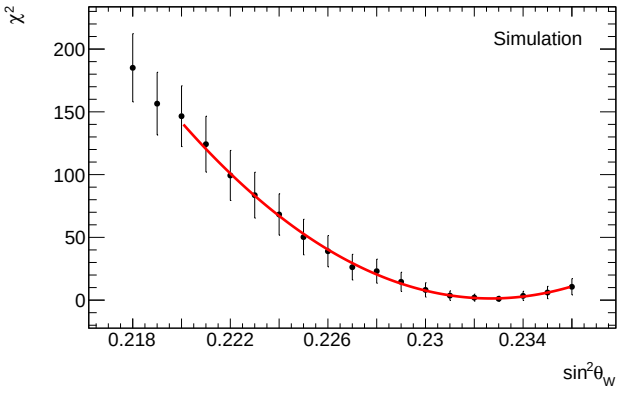

Figure 6.7.: χ^2 results of the template comparisons to the simulated event sample. A 2^{nd} order polynomial is fitted to the distribution from which the most probable value of $\sin^2\theta_W^{\text{eff}}$ is extracted. The $\chi^2_{\text{min}}/\text{ndf} = 0.1$ is below 1 as the templates are generated from the same simulated event sample used as input.

The resulting distribution of $\sin^2\theta_W^{\text{eff}}$ values is shown in Fig. 6.8. Its width of $45(6) \cdot 10^{-4}$ agrees well with the mean statistical uncertainty of the 31 samples of $< \sigma >= 48 \cdot 10^{-4}$.

2. A bootstrap test [72] has been performed. For this N events are drawn randomly from the data sample 1000 times. The analysis is performed on each of the 1000 pseudo data sets and the resulting distribution of extracted values for $\sin^2\theta_W^{\text{eff}}$ is fitted by a Gauss curve. Its width of $\sigma_{\text{boostrap}} = 0.00094$ agrees well with the uncertainty calculated in the template fit of $\sigma_{\text{t-fit}} = 0.00087$. Details are described below.

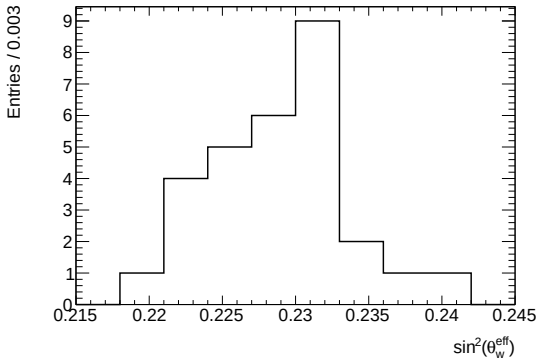

Figure 6.8.: The available dataset is divded into 30 disjunct samples with 55k events each. The measured $\sin^2\theta_W^{\text{eff}}$ are histogrammed. The RMS $= 45(6) \cdot 10^{-4}$ is a measure for the statistical uncertainty. It is in agreement with the mean statistical uncertainty calculated from the template fits $< \sigma >= 48 \cdot 10^{-4}$.

6.3.1. Bootstrap Test

Bootstrapping is a commonly used procedure to estimate observables of random distributions when only a sub-sample S of the unknown underlying distribution F is available [72]. Here it is adapted to estimate the statistical uncertainty of the measurement of the weak mixing angle.

The idea is to N times randomly draw with replacement n events from S. The N drawn samples are considered statistically independent. For this study $\sin^2\theta_W^{\text{eff}}$ is extracted from each of the N samples. The distribution of resulting values for $\sin^2\theta_W^{\text{eff}}$ is expected to follow a Gauss curve if N is chosen large enough. Its width corresponds to the statistical uncertainty of the sample S on this observable.

In this specific case n is chosen to equal the number of events in the data sample S, which is 1.6 M, and N to be 1000. Instead of drawing random events, which is an inefficient procedure on the root-trees used to store the event information, all events are given an individual weight randomly drawn from a poisson distribution with mean and variance set to 1. For each of the N samples the initial random seed is changed.

The resulting distribution of extracted $\sin^2\theta_W^{\text{eff}}$ values is fitted with a Gauss function, shown in Fig. 6.9. The width corresponds to the statistical uncertainty on $\sin^2\theta_W^{\text{eff}}$ and is found to be $\sigma_{\text{bootstrap}} = 0.00094$. This is in good agreement with the value estimated from the template fit $\sigma_{\text{t-fit}} = 0.00087$.

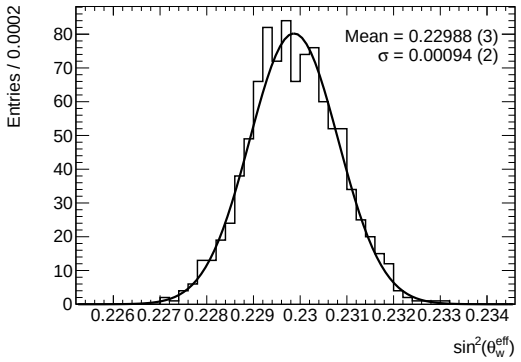

Figure 6.9.: Histogrammed $\sin^2\theta_W^{\text{eff}}$ values extracted from each of the 1000 bootstrap samples (cf. text). The distribution is fitted with a Gauss function. Good agreement of the width of the Gauss curve in comparison to the statistical uncertainty calculated during the extraction of $\sin^2\theta_W^{\text{eff}}$ from the data sample is found.

6.4. Event selection

As the data statistics is not limiting this analysis the best possible purity of events in matching the signature $pp \to Z/\gamma* \to \mu\mu$ was aimed at. All selection criteria are cuts on properties of the measured tracks and vertices. No calorimeter information is used in this analysis. The cuts are grouped in three categories: collision event selection, selection of well reconstructed muons and, finally, the Z selection. A summary of all event selection cuts, which are described in the following, can be found in Tab. 6.1. The event selection is similar to the one used for the efficiency determination described in section 5.2. Throughout the analysis the transverse momentum information is taken from the measurement of the inner detector track associated with the muon considered. The reason for this a mismodelled alignment of the muon spectrometer is the MC simulation, which turned out to significantly affect the analysis. For details see section 6.7.2.

All data recorded in 2011 with a fully operational detector is considered in this analysis, corresponding to $4.7\,\mathrm{fb}^{-1}$. The information about the detector status is provided on a per luminosity block basis in the so called good run list (GRL) provided by the Data Quality Group [47]. Events must furthermore pass the muon trigger *EF_mu18_MG_medium* which includes a lower threshold of $18\,\mathrm{GeV/c}$ on the transverse momentum of the muon track. To ensure that the event is a p–p collision at least one primary vertex not further than 200 mm away from the nominal interaction point with at least three associated tracks must be reconstructed. These requirements are considered as the collision event selection.

In the next steps well reconstructed muons are identified. They must have a transverse momentum above the trigger threshold of $p_\mathrm{T} > 20\,\mathrm{GeV/c}$ and fall within the acceptance of the inner detector, i.e. $|\eta| < 2.4$. The tracks are required to be isolated in order to reject background events, in particular muons originating from QCD processes. The isolation variable is the sum of the transverse momenta of all tracks in a cone of $\Delta R = \sqrt{(\Delta\eta)^2 + (\Delta\phi)^2} < 0.2$ around the track in question, excluding that one, divided by the p_T of the track in question. This variable, named *cone activity*, is required to be smaller than 0.1. To ensure a proper definition of the cone activity in the entire geometrical acceptance of the analysis, the η range is limited to be smaller than 2.4, whereas the acceptance of the inner detector reaches up to $|\eta| < 2.5$. All muons are furthermore required to have a minimum number of silicon hits in the inner detector and a maximum number of missing hits, called holes, as well as a successful extension in the TRT within its geometrical acceptance. To reduce the contamination with cosmic rays, the tracks must have a longitudinal impact parameter of less than 10 mm with respect to the reconstructed primary vertex.

The last set of cuts selects the actual event signature of interest. Exactly two good muons with opposite charges are required. Events with more than two good muons are discarded in the analysis to avoid combinatorial background when reconstructing the Z bosons. Finally, the invariant mass of the di-muon pair is required to be larger than $60\,\mathrm{GeV/c^2}$, as is the case for the generated intermediate state of the used MC signal sample.

The distributions of several kinematic quantities for the selected $Z/\gamma^* \to \mu\mu$ candidates are shown in Fig. 6.10 for the measured data and the PYTHIA MC signal sample. To reach the very good agreement observed between data and simulation in these plots, several corrections have to be applied to the simulated event sample, which are described in the next section.

Tab. 6.2 shows the number of data events surviving the selection described above.

Collision Event Selection	
Data quality	GRL [48]
Trigger	EF_mu18_MG_medium (p_{T} threshold 18 GeV/c)
Primary Vertex (PV) with $\geq$ 3 tracks	$\geq$ 1
$\lvert z_0\,(\mathrm{PV})\rvert$	< 200 mm
Good Muon Selection	
Kinematics	$p_{\mathrm{T}} \geq 20$ GeV/c & $\lvert\eta\rvert \leq 2.4$ & $\lvert z_0\rvert < 10$ mm
ID Si hit requirement	hit in B-layer = 1 if expected
	number of pixel hits[1]> 1, SCT hits > 5
TRT hit requirements: $\lvert\eta\rvert \leq 1.9$	Hits + Outliers > 5 & $\frac{\text{Outliers}}{\text{Hits+outliers}} < 0.9$
TRT hit requirements: $\lvert\eta\rvert > 1.9$	if (Hits + Outliers > 5): $\frac{\text{Outliers}}{\text{Hits+outliers}} < 0.9$
Isolation	$\sum_{\text{tracks}} p_{\mathrm{T}}^{ID} \,/\, p_{\mathrm{T}} < 0.1$ inside cone of 0.2
Z signature selection	
number of muons in event	$= 2$
charge of muons	$c_1 \cdot c_2 = -1$
invariant mass	$m_{\mathrm{Z}} > 60$ GeV/c^2

[1] non functional sensors in the path of the track are counted as hits for these cuts

Table 6.1.: Summary of all cuts used for selecting $pp \to Z\gamma^* \to \mu\mu$ candidate events.

For reference, Tab. 6.3 shows the same results, obtained with the signal MC.

Data			
Cut	**Number of Events [10^6]**	**Abs. Efficiency [%]**	**Rel. Efficiency [%]**
Collision event. selection	59.79	100	100
Muon type	9.71	16.2	16.2
$p_T(\mu) > 20\,\text{GeV}$	2.15	3.60	22.2
$\eta(\mu) < 2.4$	2.03	3.41	94.60
MCP Quality	1.96	3.28	96.29
$(z_0 - z_{vtx}) < 10$ mm	1.958	3.27	99.84
Isolation	1.70	2.85	86.95
exactly 2 muons	1.70	2.85	99.99
Opposite charge	1.70	2.85	99.93
Invariant mass $> 60\,\text{GeV/c}^2$	1.63	2.73	96.02

Table 6.2.: Number of events in data sample passing each selection cut. The cut flow starts after the collision event selection as no information about the events rejected by the GRL or the trigger is available.

Monte Carlo signal			
Cut	**Number of Events [10^6]**	**Abs. Efficiency [%]**	**Rel. Efficiency [%]**
All	9.99	100	100
Collision event selection	7.24	72.46	72.46
Muon Type	4.99	49.90	68.87
$p_T(\mu) > 20\,\text{GeV/c}$	4.36	43.67	87.51
$\eta(\mu) < 2.4$	4.11	41.11	94.15
MC Quality	4.00	40.05	97.41
$(z_0 - z_{vtx}) < 10$ mm	3.99	39.98	99.82
Isolation	3.94	39.39	98.51
exactly 2 muons	3.93	39.39	1.00
Opposite charge	3.93	39.39	99.99
Invariant mass $> 60\,\text{GeV/c}^2$	3.92	39.27	99.70

Table 6.3.: Number of events in Monte Carlo signal sample passing each selection cut. Absolute and relative efficiency of each cut are shown.

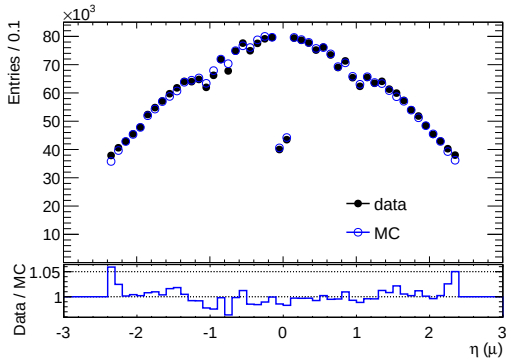

(a) Pseudorapidity distribution of selected muons.

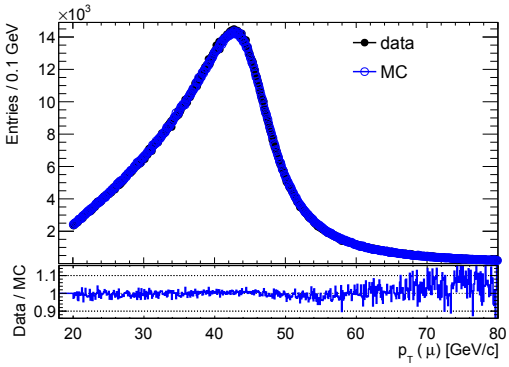

(b) Transverse momentum distribution of selected muons.

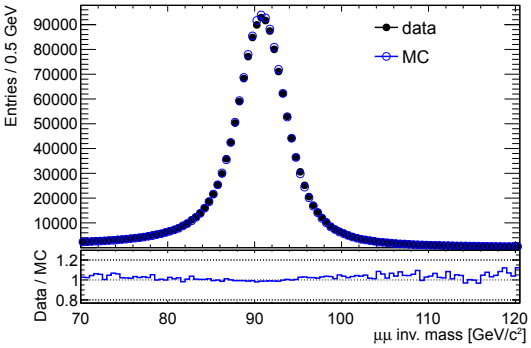

(c) Invariant mass distribution of selected muon pairs, linear scale.

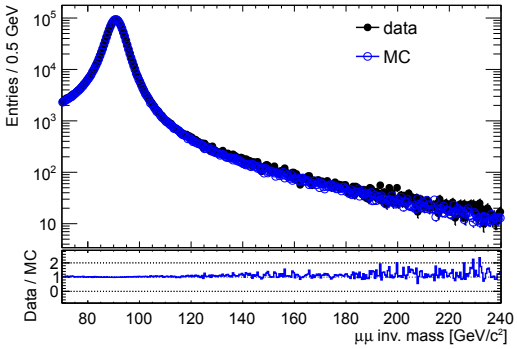

(d) Invariant mass distribution of selected muon pairs, logarithmic scale.

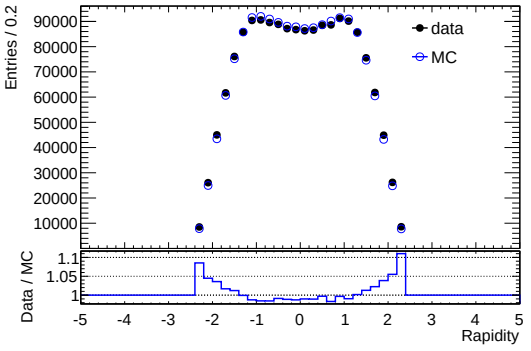

(e) Rapidity distribution of selected muon pairs.

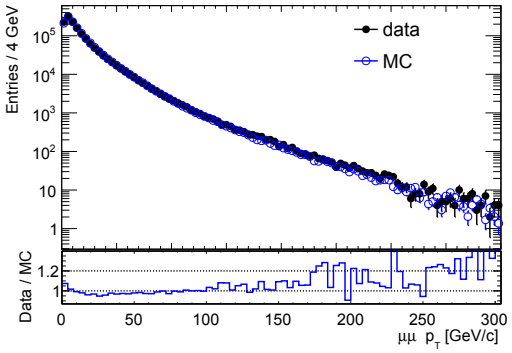

(f) Trasvers momentum distribution of selected muon pairs.

Figure 6.10.: Comparison of control distributions obtained from PYTHIA MC simulation after all corrections (open circles) and measured data (filled circles). A good agreement between simulation and measurement is observed in particular in the invariant mass distributions.

6.5. Corrections applied to the Monte–Carlo simulation

The MC simulation incorporates the best knowledge of the detector at the time of production of the simulated events. But with an increasing amount of analysed data the understanding of the actual detector system improves and on top of that the detector conditions may vary. Most importantly the resolution and efficiencies are time dependent, e.g. due to changes in the alignment or failing modules. To obtain the best predictions from the simulated events those effects have to be taken into account at the time of analysing the recorded data. Therefore a number of corrections are applied to the simulated events. These corrections are provided to the ATLAS collaboration by the performance groups, in case of muons by the Muon Combined Performance (MCP) group, and are recalculated whenever a significant amount of new data has been collected. Note that no corrections are applied to data after the reconstruction of the events.

The corrections applied in this analysis are calculated for the entire data set recorded in 2011. PYTHIA is used as event generator for the simulation of the signal process. Applied corrections are listed here and their impact on the analysis will be explained later on:

- Pile–up correction
- Momentum smearing
- Momentum scale correction
- Trigger and reconstruction efficiency correction
- Reweighting of transverse momentum distribution of the Z/γ^*.

Pile–up correction:
The average number of multiple interactions within one bunch crossing, μ, also called pile–up, varies with the instantaneous luminosity. The amount of pile–up depends on the number of protons in the colliding bunches and the size of the beam spot at the interaction point. The luminosity, in addition, also depends on the number of bunches in both beams. Accordingly, μ varies for different periods of data taking when the beam parameters change. Additionally, μ decreases during a fill as the instantaneous luminosity drops. In MC, however, only a couple of different values of μ are simulated. As the analysis as well as the event reconstruction may show a μ dependent performance the pile–up spectrum in the simulated event samples is reweighted to match the one found in the data sample used in the analysis. It turns out that the asymmetry spectrum is not affected by pile–up effects.

Momentum smearing:
The resolution of the detector is modelled slightly better in the simulation than it turns out to be in reality. This effect is accounted for by smearing the momenta of the reconstructed muons in the simulated event sample until the resolution matches the one found in data. The ID track momentum as well as the combined muon momentum is smeared. The smearing constants are determined by fitting the Z lineshape. The procedure is described in detail in [73]. The correction constants used are distributed with the muon momentum smearing package MuonMomentumCorrections-00-05-03 including

the uncertainties on the correction constants.

Momentum scale correction:
The scale of the muon momenta is determined from the decay of Z bosons into muons. The scale information is provided in bins of the position of the muon within the detector, (η, ϕ), and its transverse momentum, p_{T}. The position of the Z mass peak is used to determine the momentum scale [73]. A global scale, common for both charges of the decay muons, is determined as well as a charge dependent scale. Accordingly the scale correction is applied in two steps: first the global correction followed by the charge dependent one. As the momentum scale also influences the width of the Z mass peak, similar to the momentum smearing, the corresponding corrections for the simulated events are provided together with the momentum smearing and, in addition, also the corresponding uncertainties.

Trigger efficiency correction:
The efficiency of the muon trigger is also slightly different in the recorded data compared to the simulation. This is corrected by means of scale factors describing the efficiency difference between data and simulation in bins of η, ϕ and p_{T} of the muon which are applied to the simulated event sample. Details on the trigger efficiency scale factors can be found in [74]. The scale factors are provided with the muon efficiency correction package MuonEfficiencyCorrections-02-01-01.

Reconstruction efficiency correction:
The reconstruction efficiency is handled similarly to the trigger efficiency. The determination of the reconstruction efficiency scale factors is described in detail in chapter 5 and published in [63]. As the results shown there have been obtained with the data set recorded in 2010 they are not used in this analysis. Instead the up to date numbers obtained from the data set recorded in 2011 are used which are distributed with the muon efficiency correction package MuonEfficiencyCorrections-02-01-01. The analysis result proved to be insensitive to variations of the efficiency scale factors.

Reweighting of $p_{\mathrm{T}}(Z/\gamma^*)$:
The $p_{\mathrm{T}}(Z)$ distribution of the PYTHIA signal sample (cf. App. A) is wrongly modelled in the MC11 tune [39], but correct in the older MC10 tune. Hence a reweighting of the used MC events to the valid $p_{\mathrm{T}}(Z)$ distribution is performed. Very good agreement with the measured data is observed afterwards (cf. Fig. 6.10f). Note that this correction is only applied to the PYTHIA signal sample.

After all corrections are applied the agreement between the simulated events and the measured data is very good. This can be seen in the distributions of basic properties of the selected muons and Z bosons shown in Fig. 6.10. Also the forward–backward asymmetry spectrum is described well by the PYTHIA simulation (see Fig. 6.11).

6.5.1. Some remarks on the shape of the A_{fb} versus $m_{\mu\mu}$ distribution

The A_{fb} spectrum measured from data is well described by the PYTHIA simulation (cf. 6.11). There is one surprising eye-catching feature: The asymmetry is nearly constant in the vicinity of the Z-peak (86 GeV/c^2–95 GeV/c^2) in the data as well as in the

reconstructed MC, while this is not the case before the detector simulation (truth information). This effect is caused by the finite mass resolution of the detector. It can be reproduced by smearing the truth information on the invariant mass according to the detector resolution, after taking into account the effects of dilution and acceptance (cf. fig6.12).

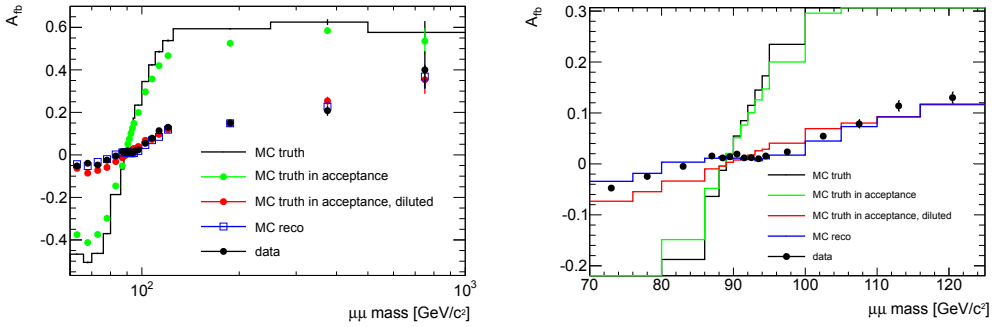

(a) Full considered mass range

(b) Zoom into the Z-peak region.

Figure 6.11.: Comparison of the A_{fb} versus $\mu\mu$ invariant mass ($m_{\mu\mu}$) distribution from measured data and MC simulation: before detector simulation in the full phase-space (truth), within the acceptance of this analysis, with added dilution and after detector simulation (reco). (a): full mas range, (b): zoomed mass range.

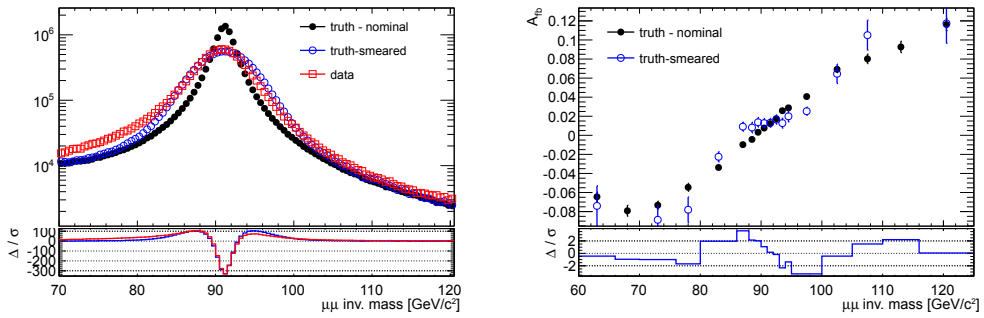

(a) Z-mass spectrum in simulation before and after smearing in comparison to the measured data.

(b) A_{fb} spectrum before and after smearing of the invariant mass.

Figure 6.12.: Illustration of the impact of the finite detector resolution on the A_{fb} versus $\mu\mu$ invariant mass distribution. Simulated events are considered before detector simulation, but required to be within the acceptance of the analysis and with added dilution. The invariant mass is smeared with a Gaussian function with $\sigma = 2.8\,\mathrm{GeV/c^2}$.

6.6. Background considerations

The amount of events originating from background (bg) processes passing the event selection (cf. sec. 6.4) and their influence on the measured weak mixing angle is studied in this section. Background processes can be split into four categories:

1. Electroweak single boson production
2. Electroweak di-boson production
3. $t\bar{t}$ production
4. QCD reactions with muons in the final state, e.g. $c\bar{c}$ and $b\bar{b}$ jet production.

Electroweak processes and top production are well described by MC simulation and large event samples are available. Therefore, the bg contamination due to these events is studied on the simulated event samples. The cross section for QCD reactions with muons in the final state is about two orders of magnitude larger than the cross section of Z boson production. No simulated event samples with large enough statistics exist to reliably determine the impact of QCD background on this measurement. Accordingly, it has to be estimated from the data sample itself. An overview of all considered bg channels is presented in Tab. 6.4 and a summary of their contributions in Tab. 6.6. Important features of the bg samples, such as the generator used, the generator efficiency, ϵ_{gen}, the generator cross section, σ_{gen}, and (N)NLO corrections applied to σ_{gen} by means of a multiplicative factor, called k-factor, are listed in Tab. 6.5. The integrated luminosity of each sample is calculated by

$$\int L = \frac{\sum \text{event weights}}{\sigma_{\text{gen}} \cdot k \cdot \epsilon_{\text{gen}}}.$$

As some generators produce events with weights $w \neq 1$ the sum of event weights is used rather than the number of events in the sample.

Channel	σ_{eff} [nb]	$\int L\,[fb^{-1}]$	available	after selection	norm $\int L_{data}$
Data	-	4.70		$1.67 \cdot 10^6$	$1.67 \cdot 10^6$
$Z \rightarrow \tau\tau$	0.833	5.522	4.6 M	1.42 k	1.20 k
$W \rightarrow \mu\nu$	10.50	0.4 - 8.3	11.6	201	205
$W \rightarrow \tau\nu$	10.50	0.4 - 8.3	11.6	15	22
WW	0.0222	112.16	2.49 M	30 k	1.22 k
WZ	0.0056	178.6	1.00 M	49 k	1.29 k
ZZ	0.0013	192.3	15.0 M	39 k	950
$t\bar{t}$	0.0909	165.0	15 M	133.4 k	3.8 k
QCD	-	-	-	27.75	499
sum					9186

Table 6.4.: Background contributions considered and the available MC statistics in each channel. The QCD bg has been estimated from the measured data (cf. sec. 6.6.1).

The total amount of bg events passing the selection is only 0.6% of the overall selected event sample. Such a small bg contamination can only significantly influence the

Process	Generator	σ_{gen} [nb]	k-factor	gen. eff	σ_{eff} [nb]
$Z \to \mu\mu$	PYTHIA	0.8356	1	1	0.8356
$Z \to \tau\tau$	PYTHIA	0.8328	1	1	0.8328
$W \to \mu\nu$	Alpgen	8.75	1.2	1	10.50
$W \to \tau\nu$	Alpgen	8.75	1.2	1	10.50
WW	Herwig	0.0150	1.48	1	0.0222
WZ	Herwig	0.0035	1.60	1	0.0056
ZZ	Herwig	0.0046	1.30	0.213	0.0013
$t\bar{t}$	MCNLO	0.0790	1.15	1	0.0909

Table 6.5.: List of generators and event sample properties of the considered bg processes.

Backgrounds used in correction	fitted $\sin^2\theta_W^{\text{eff}}$	difference to uncorrected data
no correction	0.22969	-
$t\bar{t}$	0.22947	$-22 \cdot 10^{-5}$
EW	0.22969	0
QCD	0.22969	0
All	0.22937	$-22 \cdot 10^{-5}$

Table 6.6.: EW and $t\bar{t}$ background contributions are estimated from MC simulation, the QCD bg from the measured data. Estimated bg contributions are subtracted from the data distributions after appropriate normalisation. $\sin^2\theta_W^{\text{eff}}$ is extracted from the bg corrected distributions.

asymmetry, if it shows a significant asymmetry in the $\cos(\theta)$ distribution itself. For the largest bg channel, which is $t\bar{t}$ production, the $\cos(\theta)$ distribution of selected events is shown in Fig. 6.13. A clear asymmetry is observed, which is opposite in sign to the one observed in the signal sample (cf. Fig. 6.4a). To check the impact of the $t\bar{t}$ contamination on the measured $\sin^2\theta_W^{\text{eff}}$, it is subtracted from the data distributions and $\sin^2\theta_W^{\text{eff}}$ is extracted. Compared to the unmodified data sample the extracted weak mixing angle changes by $-22 \cdot 10^{-5}$ from 0.22959 to 0.22937. As the second largest contribution, $Z \to \tau\tau$, has four times less events passing the selection it contribute at least a factor of four less than the $t\bar{t}$ channel. For the final result all bg contributions are summed up, normalised to the integrated luminosity of the data sample, and subtracted from the data distribution before extracting the weak mixing angle. The summed contribution of all background channels listed in Tab. 6.4 changes the measured value of $\sin^2\theta_W^{\text{eff}}$ by $-22 \cdot 10^{-5}$, completely dominated by the $t\bar{t}$ channel. In fact, correcting the measured distributions for QCD or EW background contributions has no visible effect at all. The cross sections of all processes, except QCD reactions, are known to better than 10%. The selected amount of QCD bg events is estimated with rather large uncertainty. However, the $\cos(\theta)$ distribution is symmetric for these events, as is shown in the next subsection. Even doubling the amount of QCD events in the bg correction does change the result only by $0.4 \cdot 10^{-5}$. Hence, a systematic uncertainty of $(10\% \cdot 22 + 0.4) \cdot 10^{-5} \approx 3 \cdot 10^{-5}$ is assigned to the impact of the total background on the measured $\sin^2\theta_W^{\text{eff}}$.

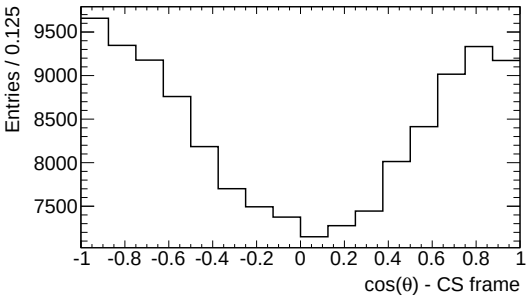

Figure 6.13.: Distributions of the decay angle $\cos(\theta)$ in simulated $t\bar{t}$ events passing the event selection. The spectrum is not normalised to the data sample size.

6.6.1. QCD background estimation from data

The QCD production of heavy quark pairs (i.e. $b\bar{b}$ and $c\bar{c}$) with subsequent decay into at least one muon in the final state has a cross section of roughly 100 nb, which is two orders of magnitude above the cross section for $Z \to \mu\mu$ events. In most cases the final state muons of these events are accompanied by several pions and other hadrons and are rejected in the analysis by the isolation requirement. Only in rare cases two isolated leptons are found in such an event. However, due to the overall large cross section this background contribution can not be neglected. For the same reason no simulated event samples exist which are large enough to predict the impact on the measurement reliably. Therefore, it has to be estimated from the measured data itself.

In order to select an event sample containing mostly QCD events the isolation requirement is inverted: $\sum p_{\mathrm{T}}^{\mathrm{track}}/p_{\mathrm{T}}^{\mu} > 0.1$. 27.75 k data events pass this selection. The cone activity spectrum is shown in Fig. 6.14a. Figure 6.14b shows the invariant mass spectrum of the selected events which follows an exponential function, as is expected. No significant asymmetry is observed in the $\cos\theta_{CS}$ spectrum, cf. Fig. 6.14c. Also the asymmetry spectrum (Fig. 6.14d) is compatible with zero asymmetry. Hence, a contamination of the signal sample with QCD events will only lead to a dilution of the observed asymmetry. This effect is negligible if the number of selected bg events is small. The PYTHIA MC samples containing $b\bar{b}$ and $c\bar{c}$ events (bb_muX and cc_muX) are used to determine the fraction of QCD events passing the nominal isolation requirement over QCD events passing the inverted isolation to be 1.8%. Using this, the total number of QCD events in the selected event sample is estimated to be $27.75\,\mathrm{k} \cdot 0.018 = 500$, equivalent to a fraction of $3 \cdot 10^{-4}$ on the total amount of data events. When subtracting the QCD template estimated as described above from the selected event sample no change of the measured weak mixing angle is observed. Even when assuming large uncertainties on the number of QCD bg events of a factor two, the extracted $\sin^2\theta_W^{\mathrm{eff}}$ changes by only $0.4 \cdot 10^{-5}$ which is negligible. Nevertheless, this background channel is taken into account when calculating $\sin^2\theta_W^{\mathrm{eff}}$ and a systematic uncertainty of $0.4 \cdot 10^{-5}$ is assigned on the $\sin^2\theta_W^{\mathrm{eff}}$ measurement.

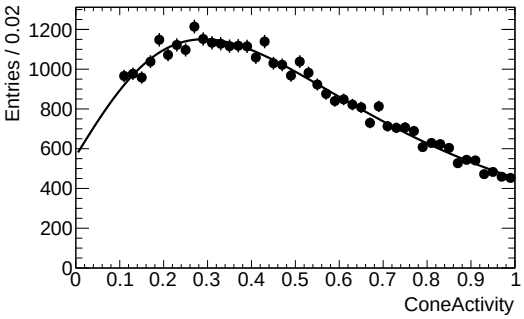

(a) Cone activity spectrum after inverting the isolation requirement to $\sum p_{\mathrm{T}}^{\mathrm{track}}/p_{\mathrm{T}}^{\mu} > 0.1$. The distribution is well described by a Landau function (solid line).

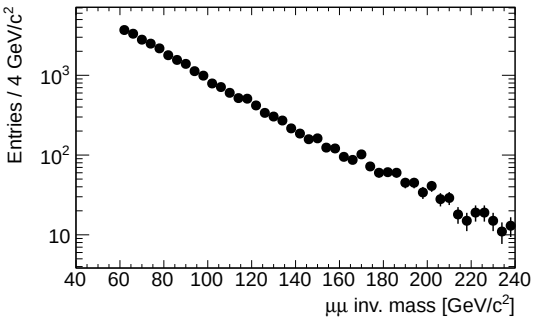

(b) Dimuon invariant mass spectrum, following the expected behaviour for QCD reactions.

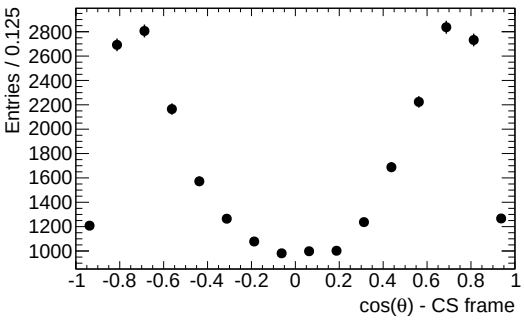

(c) $\cos(\theta_{CS})$ spectrum. No significant asymmetry is observed (mean = 0.0064).

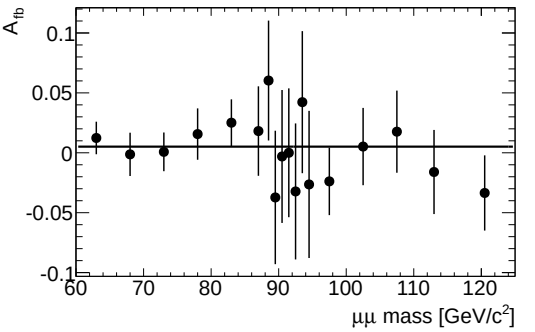

(d) A_{fb} versus invariant $\mu\mu$ mass distribution, fitted with a constant function. The result $c = 0.0051(63)$ is compatible with 0 within the errors.

Figure 6.14.: Spectra of QCD events selected form the data sample by inverting the isolation requirement.

6.7. Systematics

Several corrections are applied to the MC simulation, as described in sec. 6.5. The uncertainties on these corrections are treated, among others, as systematic uncertainties of the measurement. All contributions to the systematic uncertainty are discussed in this section. The various sources are, in order of significance:

- MC statistics:
  This item reflects the impact of the statistical uncertainty of the templates on the measured quantity due to the limited size of the MC samples. With the generation of larger MC samples this uncertainty could relatively easily be reduced.

- PDFs:
  The asymmetry spectrum differs for up- and down-type quarks. Hence the measurement is sensitive to the flavour composition of the initial state which is described by the PDF.

- Momentum scale dependence:
  Changing the weak mixing angle has a similar effect on the A_{fb} spectrum as moving the position of the Z-peak. Therefore, a precisely fixed absolute momentum scale of the muons, which determines the Z-peak position and influences its width, is crucial for this measurement.

- Alignment uncertainties:
  Mismodelled alignment of the tracking detectors may result in charge dependent variation of the measured momentum. Even if the Z peak position remains unchanged the boost into the Z-rest frame will change. In the worst case this leads to a flip of the sign of the measured polar angle in the decay. Although this effect overlaps with the systematics on the momentum scale, it is added as a separate uncertainty as studies showed a large sensitivity on misalignment effects.

- Momentum smearing:
  To match the MC prediction to the data the momenta of the muons are smeared. This contribution accounts for the uncertainty on the smearing coefficients.

- Background:
  The uncertainty of the background cross sections is only known to a precision of $\sim 10\%$. This translates into an uncertainty on the measured weak mixing angle, which has been discussed in sec. 6.6.

Table 6.7 lists all contributions. Adding them in quadrature yields a total systematic uncertainty of ± 0.00119. This is nearly twice the size of the statistical uncertainty of ± 0.00087 on the measurement and is dominated by the MC statistics and the PDF uncertainty. The latter can be improved relatively easily.

The influence of the limited MC statistics can be assessed by removing $\sigma(\text{data}_\text{i})$ and $\sigma(\text{sys}_\text{i})$ from the χ^2 calculation in Eq. (6.3). The statistical uncertainty calculated in this way solely depends on the MC uncertainty and is quoted as systematic contribution due to the limited MC statistics. For the momentum scale and smearing corrections $1\,\sigma$ uncertainties on the correction constants are provided (cf. 6.5). They are used to vary the corrections independently up and down. The value of $\sin^2\theta_W^{\text{eff}}$ is extracted

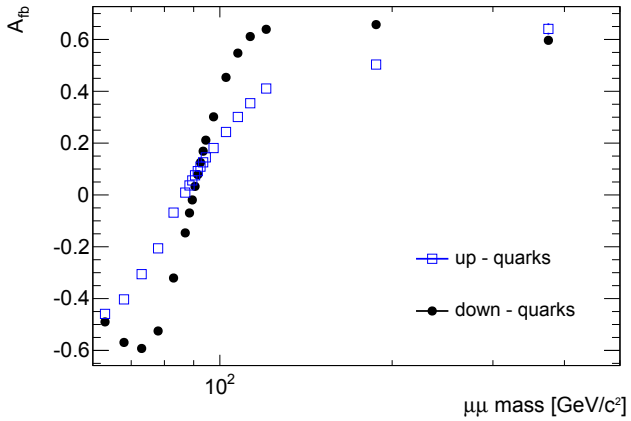

Figure 6.15.: Forward–backward asymmetry, calculated separately for up- and down-quarks in the initial sate, obtained from PYTHIA truth events without detector simulation. The PDF set used is *MRSTMCal*.

with newly generated templates for each variation. The maximum deviation of the up/down variations from the nominal value is quoted as a systematic uncertainty. A particularity of the momentum scale correction is that two independent contributions, a charge independent correction and on top of it a charge dependent factor, are applied. Both systematic contributions are listed. The latter one is showing a larger impact on $\sin^2\theta_W^{\text{eff}}$.

Contribution	size $[10^{-5}]$
Smearing correction	3
Scale correction (charge indep.)	14
Scale correction (charge dep.)	53
Misalignment	18
PDFs	59
Background	3
MC statistics	86
Total	119

Table 6.7.: Contributions to the systematic uncertainty. For the final result all contributions are added in quadrature.

6.7.1. Choice of PDF and PDF–systematics

The $A_{fb}(m_{\mu\mu})$ functional shape depends on the charge of the initial state partons, as the charge of the parton enters the definition of the vector coupling g_V. Hence, the A_{fb} mass dependence is sensitive to the fraction of up- to down-type quarks in the initial state. Fig. 6.15 shows the simulated A_{fb} versus $\mu\mu$ invariant mass distributions for up- and down-type quarks in the initial state, which differ significantly. The flavour composition of the initial state is described by the parton density function used in the simulation. Accordingly, any uncertainty on the used PDF translates into an uncertainty on the

extracted $\sin^2\theta_W^{\text{eff}}$. The procedure to estimate this uncertainty in this analysis follows [75].

The PDF used in the PYTHIA MC simulation is called *MRSTMCal* [76]. It is a leading order (LO) PDF which uses relaxed physical constraints in the PDF fitting procedure. Due to these modifications this particular PDF set is not used in the analyses. A more suited PDF is *MSTW2008Lo* [77]. It also is a LO PDF but additionally provides error sets. However, within the ATLAS EW working group it was shown that the provided error sets underestimate the uncertainty [78]. A more reliable error estimate is obtained from the *CT10* PDF set [79]. This is a NLO PDF providing 90% C.L. uncertainties. However, the predictions of a NLO PDF in conjunction with a LO MC generator may be biased. Hence, this PDF is only used for estimating the uncertainty and not for the extraction of the central value. To extract the central value, events from the PYTHIA signal simulation are reweighted to the *MSTW2008Lo* PDF, called the *target* PDF. The necessary weights are calculated as $w = f_{target}(x_1, fl_1, x_2, fl_2, Q^2)/f_{original}(x_1, fl_1, x_2, fl_2, Q^2)$. f_{target} gives the probability to find the two initial state partons with flavour fl_i and momentum fraction x_i at a given momentum transfer Q^2 using the target PDF. $f_{original}$ gives the same probability using the original PDF used in the PYTHIA simulation. In the calculation of the templates (cf. sec. 6.2) the required PDF can alternatively be specified in the generation of the truth events. In this case no dedicated reweighting is needed. To avoid the simulation of too many truth samples, the reweighting is utilised in the estimation of the PDF uncertainty. In the following the calculation of the PDF uncertainty is explained.

A common approach to estimate the PDF uncertainty is to compare results obtained using completely different PDFs and quoting the observed difference. This is considered to lead to arbitrary results, as the choice of PDFs to compare is arbitrary itself. Instead it is suggested by ATLAS [75] to use the error sets provided with the used PDF set to estimate the systematic uncertainty. For each free parameter in the parametrisation of a given PDF two additional PDFs, called *error sets*, are provided. In these PDFs the corresponding eigenvector (EV) of the diagonalised covariance matrix is set to the upper and lower limit, respectively. The error sets of a particular PDF represent the best knowledge of its uncertainty, including experimental and most theoretical uncertainties. To get the uncertainty on the measured quantity, the analysis has to be run for all error set members. The difference on $\sin^2\theta_W^{\text{eff}}$ of the up/down variation of each EV of the *CT10* PDF is presented in Fig. 6.16. To get a symmetric uncertainty estimate, the difference of the up and down variation of each EV is summed in quadrature, as is explained in [79]:

$$\sigma_{\text{PDF}} = \frac{1}{2}\sqrt{\sum_{\text{EV i}} \left(F(X_i^+) - F(X_i^-)\right)^2} = 97 \cdot 10^{-5}. \tag{6.8}$$

Asymmetric uncertainties are calculated as:

$$\sigma^+_{\text{PDF}} = \sqrt{\sum \left(\max\left[F(X_i^+) - F(X^0), F(X_i^-) - F(X^0), 0\right]\right)^2} = 93 \cdot 10^{-5} \tag{6.9}$$

$$\sigma^-_{\text{PDF}} = \sqrt{\sum \left(\max\left[F(X^0) - F(X_i^+), F(X^0) - F(X_i^-), 0\right]\right)^2} = 104 \cdot 10^{-5} \tag{6.10}$$

where $F(X^{\pm})$ denotes the extracted value of $\sin^2\theta_W^{\text{eff}}$ using templates generated with the up- (down-) ward variation of the ith EV and $F(X^0)$ the extracted $\sin^2\theta_W^{\text{eff}}$ using the central PDF in the templates. As the variation in the *CT10* error PDFs correspond to a

90% C.L. but all other uncertainties correspond to one standard deviation (68.27% C.L.), the uncertainty is scaled by a factor of 1/1.64485 [80] yielding a value of $\sigma_{\mathrm{PDF}} = 59 \cdot 10^{-5}$. It corresponds to one standard deviation and is used in the following.

The obtained uncertainty on the A_{fb} versus invariant $\mu\mu$ mass distribution itself is shown in Fig. 6.17. Furthermore, the simulated A_{fb} versus invariant $\mu\mu$ mass distributions obtained with each of the 52 *CT10* error sets, normalised by the distribution obtained with the central *CT10* PDF, are displayed. Clear correlations between the shape of these distributions on the used PDF set are visible.

The difference in $\sin^2\theta_W^{\mathrm{eff}}$ obtained for the two central PDFs of the *CT10* and *MSTW-2008Lo* PDFs is $2 \cdot 10^{-5}$, which is negligible w.r.t. the uncertainty calculated from the *CT10* error sets.

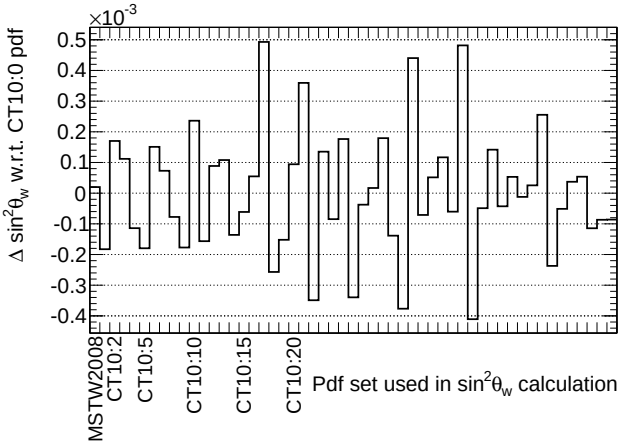

Figure 6.16.: Shown is the difference of the extracted $\sin^2\theta_W^{\mathrm{eff}}$ when varying the PDF set used for creating the templates w.r.t. the CT10 PDF. In the first bin the *MSTW2008Lo* PDF is used. In the other 52 bins the CT10 error sets are used, reflecting the up / down variations of the 26 eigenvectors describing the *CT10* PDF.

6.7.2. Alignment uncertainty

During this study the forward–backward asymmetry turned out to be very sensitive to the so called *weak mode* misalignments of the ATLAS tracking detectors. In general, geometry descriptions which satisfy the assumed track model but lead to biased physics measurements are called *weak modes*. They can also be defined as those geometry deformations which leave track-hit residuals[5] or the χ^2 of the track fit invariant. Possible origins can be deformations of the detector or artefacts of the alignment procedure itself. Two types are distinguished: One acts symmetric on both charges while the other leads to antisymmetric changes of the measured track momenta w.r.t. the sign of the charge. A detailed study of these effects and their correction is given in [81]. The first one is mainly absorbed in the calibration of the momentum scale. The second one, however, mostly affects the forward–backward asymmetry. The deformations can, e.g., be a *twist* or *curl* of the detector. The peculiarity of these deformations is that the Z-peak position remains

[5]Track-hit residuals are defined as the distance between the fitted track and the individual position measurements. They are a quality measure of the reconstructed track.

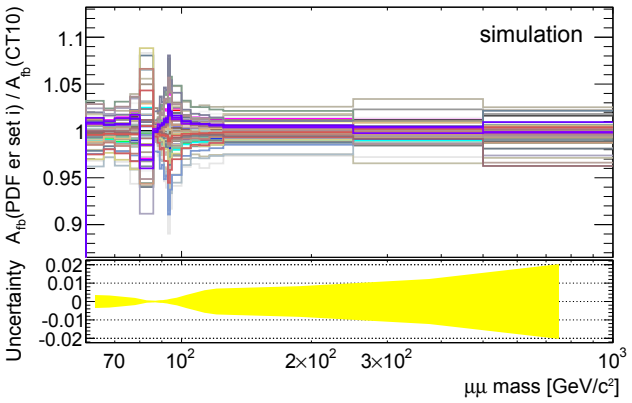

Figure 6.17.: The upper canvas displays the A_{fb} versus invariant $\mu\mu$ mass distribution for each of the 52 CT10 PDF error sets used in the simulation, normalised by the simulated distribution using the central CT10 PDF. The lower canvas displays the absolute uncertainty calculated using Eq. 6.8 (cf. sec. 6.7.1).

practically unchanged if the full phase space is integrated over. Only a degradation of the mass resolution is observed. However, when studying the dependence of the observed Z-peak on the positions of the muons in the detector, the real effect on the Z-peak position is exhibited. For more details see the dedicated note on this topic [81].

Similarly, the asymmetry is only little distorted when integrating over the full phase space. Nevertheless, the discrepancy of the measured A_{fb} versus invariant $\mu\mu$ mass distribution to the simulation is significant, cf. Fig. 6.18a. This observation triggered a thorough investigation of the weak mode misalignment. In the following the reconstruction software without correction of the charge antisymmetric weak mode misalignment is referred to as *release 16* whereas the event reconstruction including these corrections is referred to as *release 17*.

Requiring that both muons in an event fall onto the same side of the detector revealed the picture shown in 6.18b. At the Z mass events with muons recorded in one detector side exhibit a pronounced 'dip'-like structure in the A_{fb} versus invariant $\mu\mu$ mass distribution whereas the other detector side shows a much smoother behaviour. This clearly hints to a detector related origin of the observed effect. Figures 6.18c and 6.18d show the same distributions, but determining the momentum of the muons by using the inner detector (ID) or the muon spectrometer (MS), respectively. The wiggle is only observed using the ID momenta and only in the A side of the detector. These findings triggered further studies within the ID tracking performance group which eventually identified a twist of the ID in itself. A correction for this twist applied to the measured muon momenta eliminates the observed structure. In the *release 17* reconstruction the geometry description itself includes the revealed deformations. The asymmetry spectrum now shows the same behaviour on both detector sides and agrees well with the simulation when using the ID or MS p_{T} information, as shown in Fig. 6.19. The ID tracking performance group quotes 25% of the original weak mode misalignment as remaining uncertainty on the alignment in the *rel. 17* processing [81]. To assess the size of this remaining bias on $\sin^2\theta_W^{\mathrm{eff}}$ the original correction produced for the *release 16* reconstruction is applied with 25% strength to the newly processed data. The change in $\sin^2\theta_W^{\mathrm{eff}}$

of $18 \cdot 10^{-5}$ is stated as the corresponding systematic uncertainty.

In *release 16* also the asymmetry spectrum generated using the MS p_{T} information shows features which depend on the detector region, e.g. the slope is different in both detector sides, as shown in Fig. 6.18d. This effects is cured with an updated geometry of the MS in the new reconstruction, as is demonstrated by the good agreement between simulation and data in figures 6.19c and 6.19d.

Despite these improvements the asymmetry spectrum generated using momenta of combined muons shows a similar structure as seen before using the ID information, and it is incompatible with the simulation, cf. figures 6.19e and 6.19f. This was first observed in the present analysis. With valuable input provided from this analysis, the origin of this effect could be traced within the Muon Combined Performance group. As it turned out, the MS endcap C is misplaced in the geometry description by 5 cm along the beam axis. This leads to systematic shifts of the reconstructed combined muon momenta due to the setup of the track fitting algorithms. As the asymmetry analysis is the only one affected significantly, a fix of the geometry description will only be available with the next reprocessing of the collected data. Unfortunately, this is beyond the time frame of this thesis. Therefore, it was decided to only use the momentum information from the ID for this thesis. This is a reasonable approach as the momentum measurement is dominated by the ID measurements up to transverse momenta of 50 GeV/c. From 50 GeV/c to roughly 100 GeV/c both subsystems have similar contributions. The transverse momentum distribution of muons from Z decays has a maximum at 43 GeV/c.

6.7.3. Determination of used mass range in χ^2 calculation

The influence of the flavour composition of the initial state is strongest for small and large invariant masses of the dilepton pair (cf. Fig. 6.15). At the Z-pole the influence is smallest (cf. Fig. 6.17). Hence, a dependence of the systematic uncertainty due to the error on the PDF on the used mass range for extracting $\sin^2\theta_W^{\mathrm{eff}}$ is expected. Furthermore, as the weak mixing angle itself depends on the Q^2 of the reaction, it is important to study the impact of the used mass range on the measured value of $\sin^2\theta_W^{\mathrm{eff}}$. The results of this study is presented in Tab. 6.8. The extracted value for $\sin^2\theta_W^{\mathrm{eff}}$ shows no systematic dependence on the mass window. The mass range chosen for this analysis is $70 - -250\,\mathrm{GeV/c^2}$, which is a trade-off between statistical uncertainty and influence due to the uncertainty on the used PDF.

Mass range $[GeV/c^2]$	ndf	$\sigma_{\mathrm{stat.}}$	$\sin^2\theta_W^{\mathrm{eff}}$	$\chi^2_{\mathrm{min}}/ndf$
60-1000	21	87	0.22929	1.09
60-300	20	87	0.22929	1.14
70-250	17	88	0.22937	1.15
76-250	16	89	0.22900	1.03
80-125	14	90	0.22874	0.97
80-105	11	91	0.22890	1.00
86-100	9	99	0.22774	0.80

Table 6.8.: Influence of the mass range used in the χ^2 calculation on the $\sin^2\theta_W^{\mathrm{eff}}$ and its statistical uncertainty.

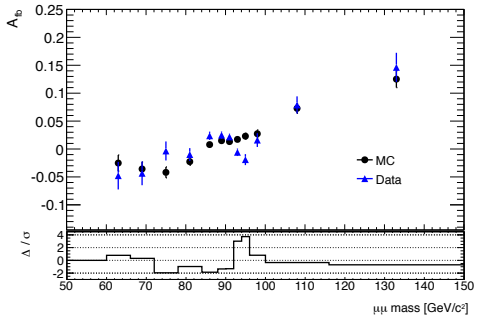

(a) A_{fb} spectrum in release 16 for data and simulation.

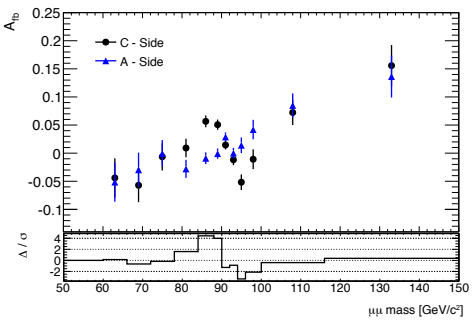

(b) A_{fb} spectrum with both muons in either one or the other side of the detector. Momentum information taken from combined muons.

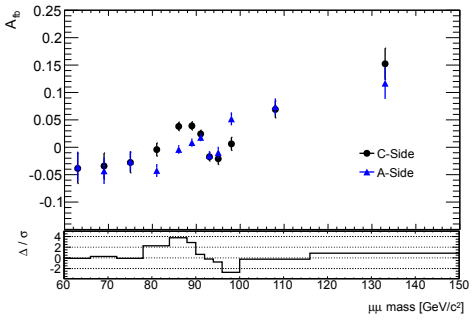

(c) A_{fb} spectrum with both muons in either one or the other side of the detector. Momentum information from the ID used.

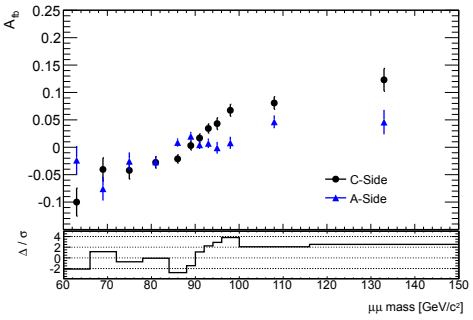

(d) A_{fb} spectrum with both muons in either one or the other side of the detector. Momentum informatino from the MS used.

Figure 6.18.: A_{fb} versus $\mu\mu$ mass distributions obtained from 460 pb^{-1} of data reconstructed with *release 16*, shown for different detector regions and detector subsystems. The influence on the asymmetry is caused by weak mode misalignments.

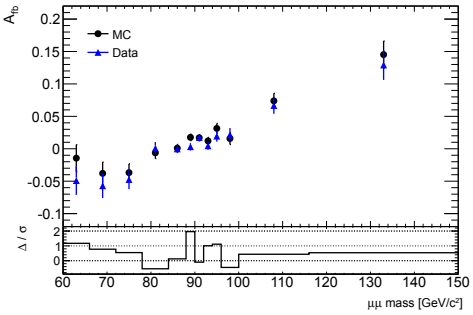

(a) ID p_{T} information, A side.

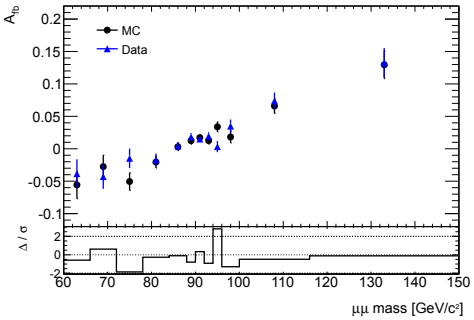

(b) ID p_{T} information, C side.

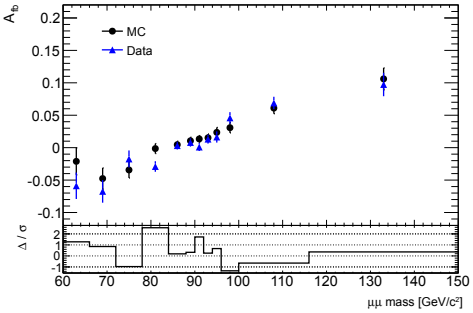

(c) MS p_{T} information, A side.

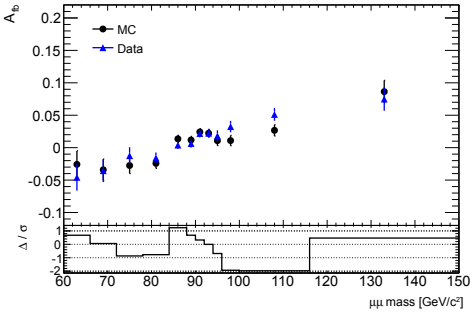

(d) MS p_{T} information, C side.

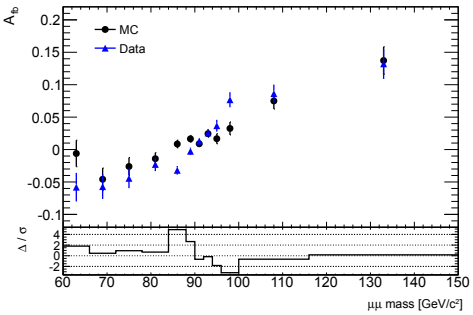

(e) CB p_{T} information, A side.

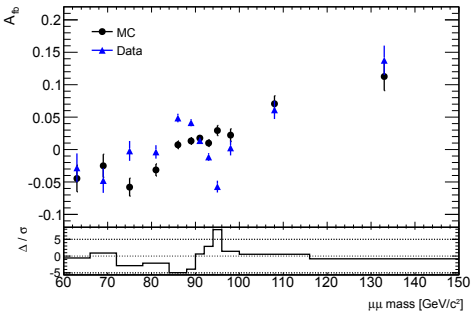

(f) CB p_{T} information, C side.

Figure 6.19.: Comparison of MC simulation to the measured data, reconstructed with *release 17* including corrections for the weak mode misalignment of the inner detector (ID).

6.8. Results

In this section the extracted value of $\sin^2\theta_W^{\text{eff}}$ from the measured forward–backward asymmetry is presented and compared to other measurements of this particular quantity.

The forward–backward asymmetry is strongly affected by the limited acceptance of the detector and the dilution (cf. section 6.1.1). Furthermore, it is very sensitive to the correct alignment of the tracking detectors, as the present study revealed (cf. section 6.7.2). However, all these effects are well described by the MC simulation which reproduces the measured data nicely. Hence, the extraction of the weak mixing angle from the A_{fb} spectrum is reliably possible using template comparisons (cf. section 6.2).

The χ^2 results of the template comparisons to the data is shown in Fig. 6.20. Each point corresponds to the χ^2 value obtained from the comparison of a template created with a particular value of $\sin^2\theta_W^{\text{eff}}$ to the measured A_{fb} spectrum. The resulting parabola is fitted to estimate its minimum, which corresponds to the measured $\sin^2\theta_W^{\text{eff}}$. The extracted value is

$$\sin^2\theta_W^{\text{eff}} = 0.22937 \pm 0.00087(stat.) \pm 0.00119(sys.).$$

The quality of the template prediction for the best matching template is obtained as $\chi^2/\text{ndf} = 1.13$. The value found is close to one, ensuring a reliable estimation of the weak mixing angle using this technique.

There have been numerous measurements of $\sin^2\theta_W^{\text{eff}}$ at similar Q^2 scales, among them the LEP and Tevatron experiments as well as CMS at the LHC. The different measurement techniques and results are presented in the following.

- LEP and SLD: The weak mixing angle is calculated directly from the forward–backward asymmetry observed at the Z-pole. Leptonic and hadronic final states are taken into account. Additionally the SLD experiment measures the left–right polarisation asymmetry A_{LR}, yielding the most precise results for the weak mixing angle. The obtained value from SLD, averaged over all experiments, is 0.23096 ± 0.00020 [17]. The averaged results from the LEP experiments is 0.23181 ± 0.00028 [17]. These two results dominate the current world average of 0.23152(16)[6].

- D0 (Tevatron): Template comparisons are used to extract the weak mixing angle (as in the present work). The obtained value is 0.23090(100) [22].

- CDF (Tevatron): CDF extracts the weak mixing angle directly from the asymmetry by comparing the SM prediction of the parameter A_4 of the angular distribution to the measurement. This method is afflicted with large theoretical uncertainties from QCD predicitons. Their obtained value is $\sin^2\theta_W^{\text{eff}} = 0.23290 \pm 0.00080(\text{A}_4\,\text{error})^{+0.00100}_{-0.00090}(\text{QCD})$ [82].

- CMS (LHC): CMS uses a maximum likelyhood fit to extract the weak mixing angle [23]. The obtained value is 0.22870(320).

- Global fit over all SM parameters: The particle data group publishes a fit over all SM parameters including many experimental datasets. Their result is $\sin^2\theta_W^{\text{eff}} = 0.23146(12)$ [17].

An overview of all results is given in Tab. 6.9 and Fig. 6.21. The result of this analysis is well compatible the results of other experiments.

[6] As presented at the Moriond conference in 2011.

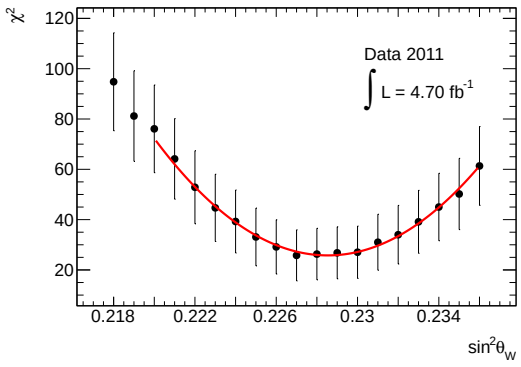

Figure 6.20.: χ^2 results of the template comparisons for different values of $\sin^2\theta_W^{\text{eff}}$ with the measured data. A second order polynomial is fitted to the distribution from which the most probable value of $\sin^2\theta_W^{\text{eff}}$ as well as the statistical uncertainty is extracted. The data distribution has been corrected for background. Note that all χ^2 values are correlated as the same simulated event sample is reweighted and compared to the same measured event sample each time. Hence the displayed statistical errors appear larger than the statistical fluctuations of the χ^2 values.

Source	$\sin^2\theta_W^{\text{eff}}$	$\Delta[10^{-5}]$	Δ/σ
this analysis	0.22937 ± 0.000147	-	-
PDG global fit [17]	0.23146 ± 0.00012	209	1.4
SLD result [17]	0.23096 ± 0.00020	159	1.1
LEP result [17]	0.23181 ± 0.00028	244	1.6
D0 [22]	0.23090 ± 0.00100	153	0.9
CDF [82]	$0.23290 \pm 0.00080^{+0.00100}_{-0.00090}$	353	1.8
CMS [83]	0.22870 ± 0.00320	67	0.2

Table 6.9.: Comparison of prediction and different results for $\sin^2\theta_W^{\text{eff}}$. Δ denotes the absolute difference of the result w.r.t. to the result of the present analysis. Δ/σ denotes the difference in units of the uncertainty (the uncertainties of both results in question are added in quadrature).

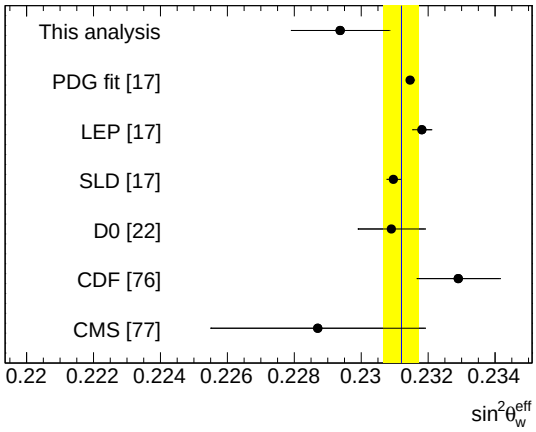

Figure 6.21.: Results from various measurements of $\sin^2\theta_W^{\text{eff}}$ in comparison to the obtained value from this analysis. The vertical bar indicates the average over all shown values, excluding the global fit, with its uncertainty.

7. Measurement of the Angular Distributions and the Spin of the Gluon

When particles decay, the angular distributions of the decay products are a rich source of information. The spin of the particle in question is accessible as well as several properties of the underlying interaction. The asymmetric part of the polar angular distribution in $Z \to \mu\mu$ decays for example is sensitive to the vector coupling of the weak force and with it to the weak mixing angle (cf. previous chapter). Other parameters of the angular distribution contain further interesting information, e.g. on the production mechanism of the intermediate state. Also properties of the particles involved in the reaction are accessible. It turns out that in the vicinity of the Z mass peak the reaction $pp \to \mu^+\mu^- + X$ is sensitive to the spin of the gluon (cf. sec. 2.2 and below). The Collins-Soper frame (CS frame) (sec. 6.1) is used to measure the angles. The event selection criteria are the same as described in sec. 6.4, except for an additional constraint on the invariant mass of the intermediate state which is required to be close to the Z mass: $|m_{ll} - m_Z| \leq 10\,\mathrm{GeV/c^2}$. In this analysis $4.70\,\mathrm{fb}^{-1}$ of data, collected in 2011, are used which corresponds to 1.46 M selected events.

The polar and azimuthal angular distributions of the decay lepton in the reaction $pp \to Z/\gamma^* + X \to \mu^+\mu^- + X$ can be separately described by two 1-dimensional functions (cf. sec. 2.2),

$$\frac{d\sigma}{d\cos\theta} \propto \left(1 + \cos^2\theta\right) + \frac{1}{2}A_0\left(1 - 3\cos^2\theta\right) + A_4\cos\theta, \tag{7.1}$$

$$\frac{d\sigma}{d\phi} \propto 1 + \frac{2\pi}{16}A_3\cos\phi + \frac{1}{4}A_2\cos(2\phi) + \frac{3\pi}{16}A_7\sin\phi + \frac{1}{4}A_5\sin(2\phi). \tag{7.2}$$

The full 2-dimensional cross section is given in Eq. (2.32). Of particular interest in this chapter are the two parameters A_0 and A_2 and their dependence on the transverse momentum (p_T) of the dilepton pair. According to the so called *Lam-Tung* relation [31] they are identical for all p_T if the spin of the gluon equals 1. In this case the leading order prediction for $A_0(p_\mathrm{T})$ and $A_2(p_\mathrm{T})$ is [33, 35]:

$$A_{0,2} = \frac{p_\mathrm{T}^2}{p_\mathrm{T}^2 + M_{ll}^2} \qquad \text{for annihilation processes,} \tag{7.3}$$

$$\text{and} \quad A_{0,2} = \frac{5p_\mathrm{T}^2}{5p_\mathrm{T}^2 + M_{ll}^2} \qquad \text{for compton} - \text{like processes.} \tag{7.4}$$

More information on the processes is given in section 2.2.

In addition, the angular distributions are interesting in themselves. They are difficult to simulate as they depend on the combination of the matrix element of the hard interaction and the parton shower model for jets due to gluon radiation. Also the spin-correlations of final state partons affect the angular distributions. They are, however, neglected in some generators. Hence, different MC generators yield different angular

distributions. PYTHIA, e.g., does only simulate the annihilation process and does not take into account spin correlations of partons in the final state (cf. chapter 3).

The measured angular distributions are heavily distorted by the acceptance of the detector. In order to recover the true angular distributions two methods are implemented using different approaches to compensate for detector effects. In the first method the effects of the acceptance on the angular distributions are estimated from the MC simulation. The measured data are corrected by applying a factor f_i in each bin i of the angular distribution, where f_i is the fraction of the bin content found in simulation on truth level (no detector simulation) and after detector simulation: $f_i = N_i^{\text{true}}/N_i^{\text{reco}}$. In this simple method significant uncertainties are introduced in the case of large f_i. Furthermore, no migration effects between bins are taken into account. However, as a rather coarse binning for the angular distributions is chosen, migration effects between bins are expected to be small.

Similar to the measurement of the weak mixing angle (cf. 6.2) the idea of the second method is to use templates which are created from MC events, and fit those to the measured angular distributions. For this purpose three orthogonal functions are created, the sum of which describes one of the 1-dimensional angular distributions. They are transformed into templates including all detector effects which finally are fitted to the measured angular distributions. This avoids any corrections to the measured data. From the relative contributions of the individual templates in this fit the coefficients A_i are calculated. Both methods yield very similar results, as is shown in sec. 7.4.

In the next section the expectations from MC simulation for the angular distribution are presented and the influence of the finite detector acceptance is discussed. The implementation and comparison of the results from both methods used to extract the angular coefficients are shown in sections 7.2, 7.3 and 7.4. Afterwards the systematic uncertainties on the angular coefficients are discussed in sec. 7.5. Finally, the measured coefficients are compared to the predictions from different MC generators and the spin of the gluon is determined (cf. sec. 7.6).

7.1. Expectations from simulation

Simulated event samples are used to study the impact of various detector effects on the angular distributions and to validate the fitting routines used to extract the coefficients A_i from the angular distributions. Furthermore, the prediction of the dependence of $A_{0,2}$ on the transverse momentum of the di-muon pair is studied in the mass window around the Z mass ($p_{\mathrm{T}}(Z)$). Several simulation programs and assumptions of spin 0 and 1 for the spin of the gluon are compared. If not stated otherwise, the angular coefficients are extracted from the measured distributions using the default PYTHIA MC event sample from the MC11c [39] production campaign for the process $Z \to \mu\mu$. The PYTHIA generator is chosen instead of AlpGEN as it nicely reproduces the transverse momentum distribution of the final state muons ($p_{\mathrm{T}}(\mu)$), which is not the case for AlpGEN. For details on the used event samples see appendix A.

The simulated (truth) angular distributions change drastically when limiting the considered phase space to the acceptance of this analysis (i.e. $p_{\mathrm{T}}(\mu) > 20\,\mathrm{GeV/c}$ and $|\eta| < 2.4$, cf. Fig. 7.1). This effect can be attributed to the correlation between the angles ($\cos\theta$, ϕ) and p_{T} or η of the final state muon (see Fig. 7.2). Compared to this acceptance effect all other experimental effects are small. The dilution of the forward–backward asymmetry due to the unknown direction of the incoming quark (see section 6.1.1) only affects the $\cos\theta$ distribution and overall remains a small effect. Further detector effects, like non–perfect resolution and efficiency, alter the shape of the angular distributions only marginally.

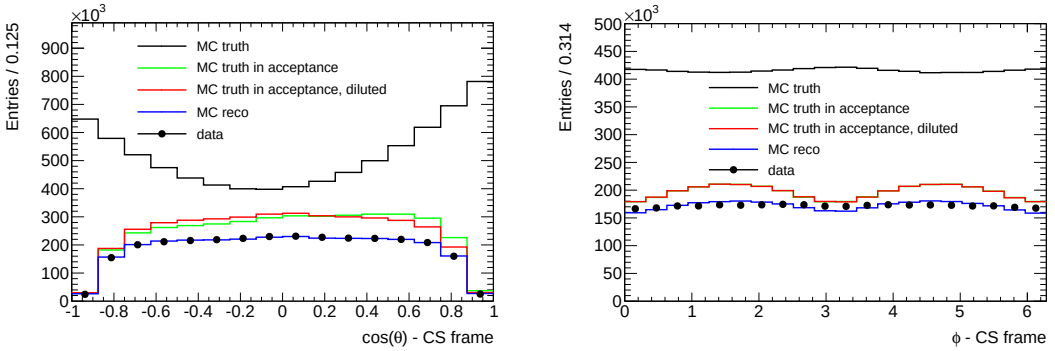

(a) (b)

Figure 7.1.: Angular distributions of the polar angle $\cos\theta$ (left) and the azimuthal angle ϕ (right) averaged over all $p_{\mathrm{T}}(Z)$. To illustrate the deformations of the true angular distributions from various sources the following histograms are overlaid: simulated true angular distributions (MC truth), acceptance cuts applied, dilution added on top, results from the MC including detector simulation (MC reco) and eventually the results from data. For both angles the limited detector acceptance has the greatest impact on the spectra. The ϕ–distribution is not affected at all by the dilution. Therefore, the green and red curves in (b) lie on top of each other. The $\cos\theta$–distribution obtained from data is matched very well by the MC prediction, whereas the ϕ–distribution is not. This is explained in detail in section 7.1.1.

All of the analysis is performed in bins of the transverse momentum of the dilepton pair

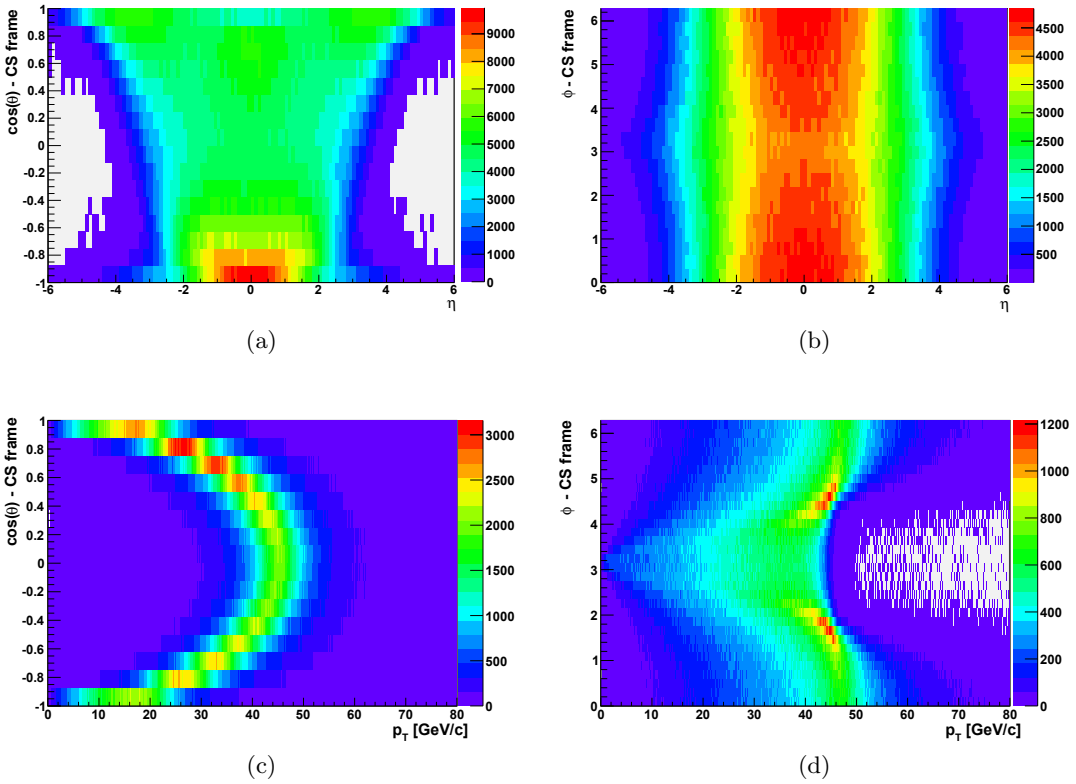

Figure 7.2.: Correlations between the decay angles $\cos\theta$ (left) / ϕ (right) and the kinematic properties of the decay muon η (upper row) / p_{T} (lower row).

in order to evaluate the dependence of the angular distributions on p_{T}. Of particular interest are the coefficients $A_0(p_{\mathrm{T}})$ and $A_2(p_{\mathrm{T}})$. The chosen binning is $p_{\mathrm{T}}^i := [0, 5, 10, 15, 20, 30, 50, 80, 150, 300]$. Unless otherwise noted, histograms of $\cos\theta$ and ϕ distributions in this chapter are from the 4^{th} p_{T} bin ($15\,\mathrm{GeV/c} \leq p_{\mathrm{T}} < 20\,\mathrm{GeV/c}$). Corresponding plots for all p_{T} bins can be found in appendix B.

To extract $A_{0,2}(p_{\mathrm{T}})$ from the simulated event sample the functions (7.1) and (7.2) are fitted to the $\cos\theta$ and ϕ distributions obtained from truth information (without detector simulation), respectively. The fit is performed individually for each p_{T} bin. Exemplary results for a single p_{T} bin are shown in Fig. 7.3. The obtained values for the coefficients $A_{0,2}(p_{\mathrm{T}})$ are shown in Fig. 7.4 together with the leading order predictions for the annihilation and the Compton-like initial states (cf. sec. 2.2). As PYTHIA only simulates the $2 \to 1$ annihilation process in the current ATLAS configuration, it is expected that the result follows the prediction for annihilation processes. This is indeed observed in the low $p_{\mathrm{T}}(Z)$ region. For larger $p_{\mathrm{T}}(Z)$ the coefficients fitted to the simulated distributions lie below the LO prediction. In contrast to the PYTHIA simulation, the measured data is expected to be a mixture of both processes and hence the p_{T} dependence of A_0 and A_2 is expected to lie in-between the prediction of both processes.

In addition to the PYTHIA prediction, simulated events from three other MC generators were analysed: *MC@NLO*, *AlpGen* and *MadGraph* [45]. The first two are next-

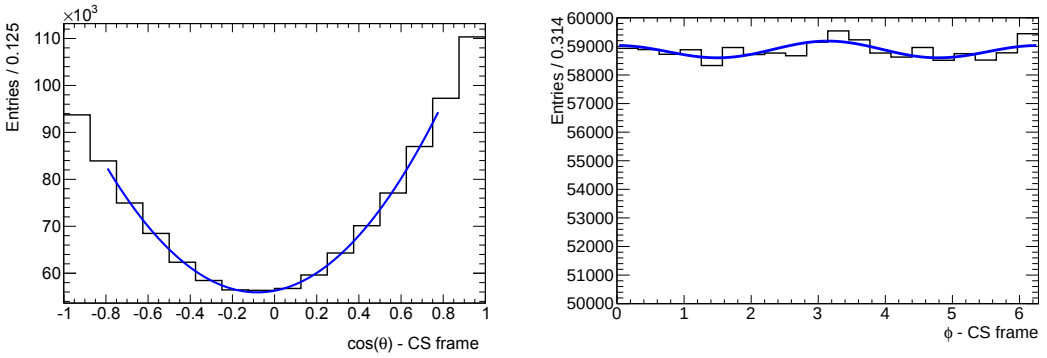

(a) (b)

Figure 7.3.: True angular distribution in $\cos\theta$ (left) and ϕ (right) for $15\,\mathrm{GeV/c} \leq p_\mathrm{T} < 20\,\mathrm{GeV/c}$, as predicted by PYTHIA. The leading order prediction (Eqs. (7.1), (7.2)) are fitted to the histograms (solid line). The fit to the $\cos\theta$ distribution excludes the outer most bins as this region is nearly completely cut out in data by the finite detector acceptance.

to-leading order generators whereas the last one is a so called matrix element generator (cf. section 3). The results obtained from *MC@NLO* and *AlpGen* are shown in Fig. 7.5. Both generators simultaneously simulate annihilation and Compton-like processes which is nicely reflected in the p_T-dependence of $A_{0,2}$. Unfortunately only 1.5 M events are available from *MC@NLO* within the considered mass window (0.5 M after detector simulation). *MadGraph* allows the generation of arbitrary Feynman graphs and the relatively easy tuning of the coupling structure of the simulated interactions. Therefore, it is used to predict angular distributions for the case of a scalar gluon. As no official ATLAS samples from this generator are available, the used event samples have been privately produced (see sec. 3.1.5), without detector simulation. Simulated are the $2 \to 2$ processes presented in section 2.2. In the case of a vector gluon ($S(g) = 1$), the extracted p_T dependence of $A_{0,2}$ (Fig. 7.6a) lies between the predictions of annihilation and compton-like processes, as expected. Furthermore they follow the Lam-Tung relation by lying on top of each other in the full p_T range. In case of a scalar gluon (Fig. 7.6b) the p_T dependence of both coefficients changes dramatically and the Lam-Tung relation becomes badly broken. Note that higher order QCD corrections violate the Lam-Tung relation only by 20% at most [84].

7.1.1. Impact of a non-zero beam crossing angle

At interaction point 1 of the LHC, where the ATLAS detector is located, the proton beams are crossing under an angle of $\beta = 240\,\mu\mathrm{rad}$, which leads to a small boost of all events along the x-axis of the laboratory frame (cf. Fig. 7.7). The effect of this non-zero crossing angle is negligible for most physics analyses. Hence the default ATLAS MC simulation assumes a zero crossing angle. However, the boost along a fixed axis in the laboratory frame defines a reaction plane for the Z-production and decay which, in general, will lead to a modulation of the azimuthal distribution of the decay leptons in the rest frame of the dilepton pair. The influence of this effect on the angular distributions is studied as follows. The boost B due to the crossing angle β of the beams is calculated

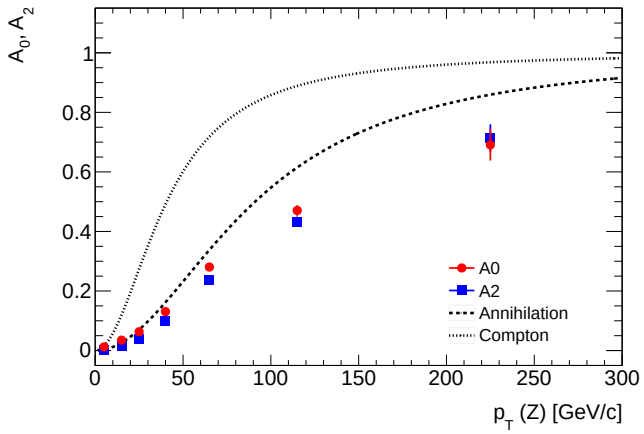

Figure 7.4.: Dependence of the coefficients A_0 (circles) and A_2 (squares) on the transverse momentum of the final state dilepton pair as obtained from the PYTHIA simulation (truth, no detector simulation applied). Leading order predictions for the annihilation and compton-like processes are shown as dashed and dotted lines, respectively. Only the $2 \rightarrow 1$ annihilation process is simulated, hence the simulation is close to the leading order prediction for the annihilation process.

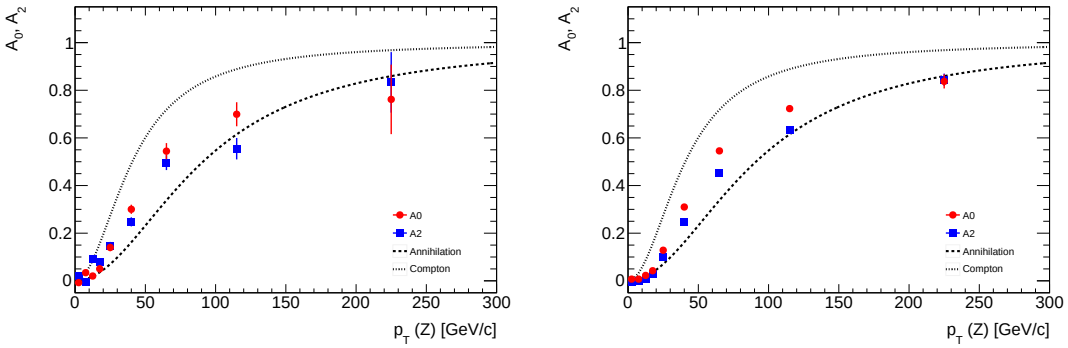

(a) MC@NLO, 1.5 M events within mass window.

(b) AlpGen, 6.7 M events within mass window.

Figure 7.5.: Predictions of A_0 and A_2 from different MC generators. No detector simulation is applied and muons are considered within the full phase space. The invariant mass of the di-muon pair is required to be within a window of $20\,\mathrm{GeV/c^2}$ around the Z-peak.

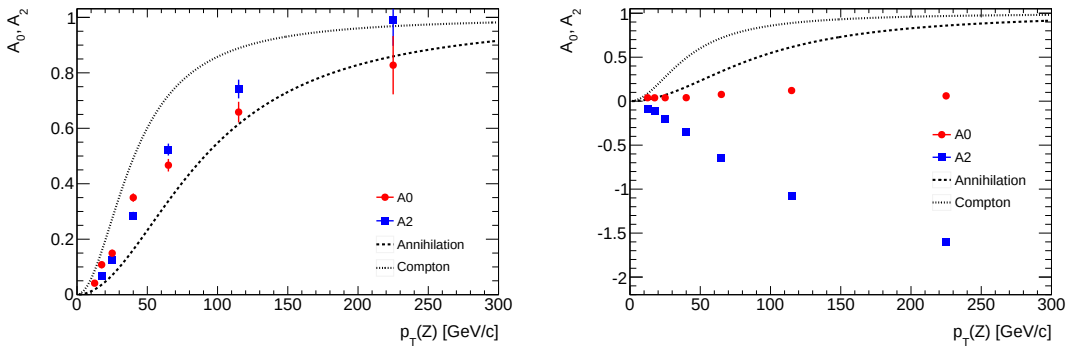

(a) Spin of gluon $S(g) = 1$

(b) Spin of gluon $S(g) = 0$

Figure 7.6.: Predictions of the dependence of $A_{0,2}$ on $p_{\mathrm{T}}(Z)$ produced with the *MadGraph* generator, once for the standard model gluon with spin $S(g) = 1$ (left hand side) and once for a scalar gluon with $S(g) = 0$ (right hand side). For the SM case the Lam-Tung relation is satisfied, i.e. $A_0(p_{\mathrm{T}}) = A_2(p_{\mathrm{T}})$ for all p_{T}, and $A_{0,2}$ lie between the LO prediction for annihilation and compton-like processes shown as dashed and dotted lines, respectively. For the scalar gluon case a completely different behaviour is observed: $A_0(p_{\mathrm{T}}) \approx 0$ and $A_2(p_{\mathrm{T}})$ is monotonously falling.

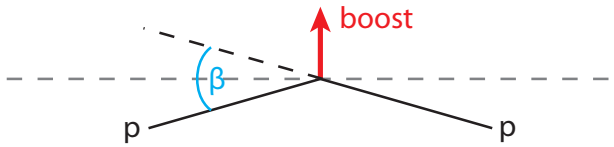

Figure 7.7.: Sketch of the beam crossing with non-zero crossing angle and resulting boost of the collision.

from the initial proton momenta, given as standard four vectors (p_x, p_y, p_z, E):

$$\begin{aligned}
\mathbf{p_1} &= \left(\sin(\beta/2)\cdot E_{\mathrm{beam}},\ 0,\ \cos(\beta/2)\cdot E_{\mathrm{beam}},\ \sqrt{E_{\mathrm{beam}}^2 + m_P^2}\right) \\
\mathbf{p_2} &= \left(\sin(\beta/2)\cdot E_{\mathrm{beam}},\ 0,\ -\cos(\beta/2)\cdot E_{\mathrm{beam}},\ \sqrt{E_{\mathrm{beam}}^2 + m_P^2}\right) \\
\mathbf{B} &= \mathbf{p_1} + \mathbf{p_2}. \qquad (7.5)
\end{aligned}$$

E_{beam} is the beam energy and m_P the mass of the proton. The resulting transverse momentum is 0.84 GeV/c. The boost calculated in Eq. (7.5) is applied to the simulated events in order to investigate the impact of the non-zero beam crossing angle on the angular distributions. The impact on the angular distributions is found to be very small. $A_{0,2}$ are affected by at most 2% in the lowest $p_{\mathrm{T}}(Z)$ bin and much less elsewhere ($\leq 0.5\%$). A_3 is changed by up to 2.3% in the lowest bin and around 1% for larger p_{T}. A_4 is not affected at all. Hence, it is confirmed that, compared to the total uncertainties (cf. Tab. 7.6) inherent to the angular distributions, the non-zero beam crossing angle is indeed negligible.

7.2. Method 1: Acceptance correction factors

The angular coefficients are determined by fitting the analytical functions Eqs. (2.33) and (2.34) to the measured angular distributions. Before this fit can be performed, however, the distortions caused by the detector on the angular distributions need to be corrected. This is described in the following. The influence of the detector is estimated using simulated events. The angular distributions are divided into bins of transverse momentum, p_{T}, and polar angle, $\cos\theta$, or azimuthal angle, ϕ. In each bin i the fraction

$$w_i = \frac{N_i^{\mathrm{true}}}{N_i^{\mathrm{reco}}} \tag{7.6}$$

is calculated, with N_i^{true} being the number of events in bin i in the full phase space, i.e before detector simulation, and N_i^{reco} the number of events in bin i after detector simulation. The weights w_i are multiplied to the measured data distributions to obtain the true angular distributions. The obtained weights for both angles are shown in Fig. 7.8. In regions affected most by the limited acceptance of the detector they become large.

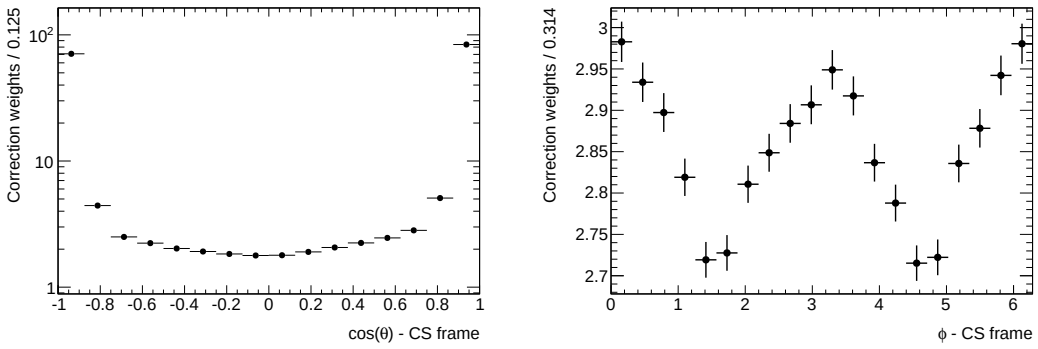

(a) (b)

Figure 7.8.: Weights to correct the influence of the detector on the angular distributions in the range $15\,\mathrm{GeV/c} < p_{\mathrm{T}}(\mu\mu) < 20\,\mathrm{GeV/c}$. In particular, the $\cos\theta$ spectrum (a) is affected by the limited acceptance of the detector. Correction factors on the ϕ spectrum show lower fluctuations and reflect the overall acceptance of about 37%.

This introduces large uncertainties on the corrected spectra. Furthermore, asymmetrical migration of events between bins is not taken into account. This effect is small due to the coarse binning.

To check the consistency of the correction method the weights are applied to the same event sample used to calculate them (closure test). As expected, the true angular distribution is recovered (see Fig. 7.9). The angular distributions obtained from data are shown in Fig. 7.10.

Finally the coefficients $A_{0,2}(p_{\mathrm{T}})$ are determined by fitting the analytical functions from Eqs. (2.33) and (2.34) to the corrected angular distributions. The result is shown in Fig. 7.11 and Tab. 7.1 in sec. 7.4.

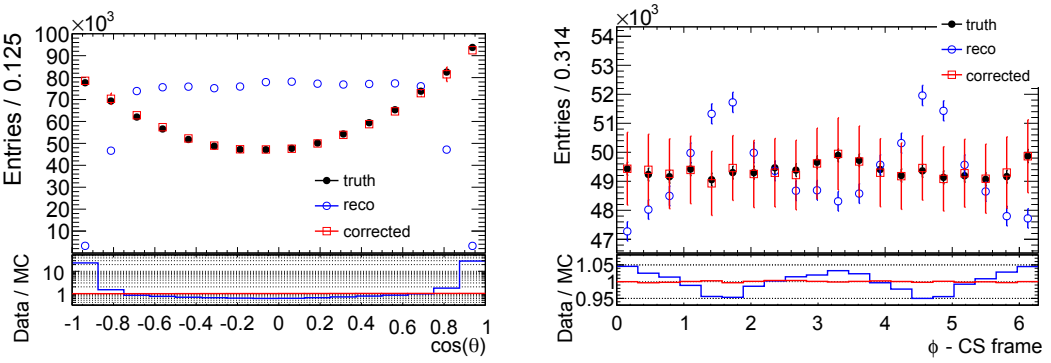

(a) (b)

Figure 7.9.: Closure test for the correction of detector effects on the angular distributions. The correction factors are applied to the same simulated event sample used to calculate them. Results are shown for the range $15\,\mathrm{GeV/c} < p_\mathrm{T}(\mu\mu) < 20\,\mathrm{GeV/c}$. Note the different scales on the y-axis of both plots. All histograms are normalised to the same integral for better comparison of the shapes.

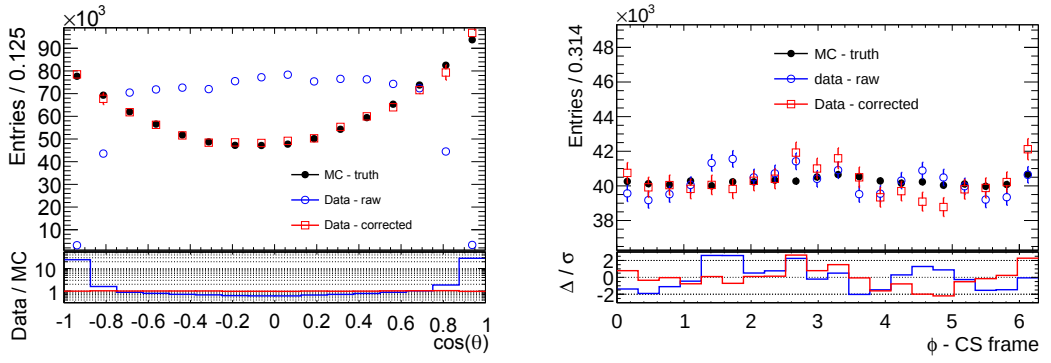

(a) (b)

Figure 7.10.: Angular distributions in the range $15\,\mathrm{GeV/c} < p_\mathrm{T}(\mu\mu) < 20\,\mathrm{GeV/c}$ as obtained from the measured data in comparison to the simulation. Note the different scales on the y-axis of both plots. All histograms are normalised to the same integral for better comparison of the shapes.

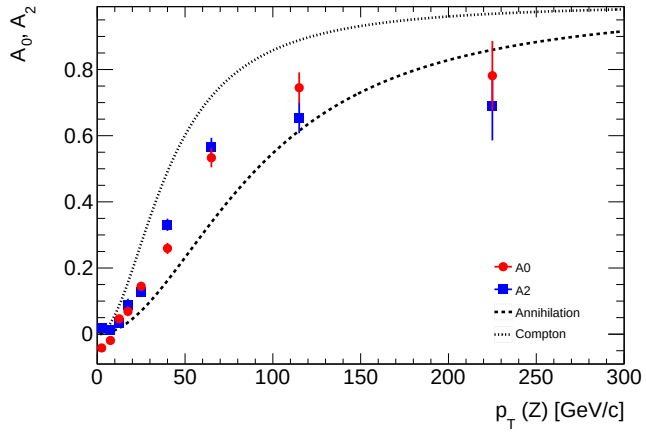

Figure 7.11.: Coefficients $A_{0,2}$ of the angular distributions as a function of the transverse momentum (p_{T}) of the final state di-muon pair. The coefficients are extracted from measured data using method 1. The simulated event sample is reweighted to match the measured $p_{\mathrm{T}}(\mu\mu)$ distribution before calculating the correction factors applied to the measured angular distributions.

7.3. Method 2: Template Fits

In this approach no corrections are applied to the measured distributions, avoiding large correction factors and the corresponding uncertainties. Instead a set of templates is created from the simulated event samples which can be fitted directly to the measured distributions. The coefficients A_i are then calculated from the respective contributions of the templates to the description of the measured data.

The templates have to fulfil certain requirements. First of all they need to be linearly independent. Otherwise the fit result may not be unique and converging fitting routine will become problematic. Furthermore, all entries in the templates must be greater or equal to zero in all bins to assure a proper normalisation. With this in mind, Eqs. (2.33) and (2.34) can be rewritten as

$$\begin{aligned}\frac{1}{\sigma}\frac{d\sigma}{d\cos\theta} &= \left(1+\frac{1}{2}A_0 - A_4\right) + (A_4)\,(1+\cos\theta) + \left(1-\frac{3}{2}A_0\right)\cos^2\theta \\ &= \alpha + \beta\cos^2\theta + \gamma\,(1+\cos\theta) \qquad (7.7)\\ \frac{1}{\sigma}\frac{d\sigma}{d\phi} &= \left(1-\frac{A_2}{4}-\frac{16A_3}{3\pi}\right) + \frac{A_2}{4}\,(1+\cos(2\phi)) + \frac{16A_3}{3\pi}\,(1+\cos\phi) \\ &= \alpha' + \beta'\,(1+\cos(2\phi)) + \gamma'\,(1+\cos\phi)\,. \qquad (7.8)\end{aligned}$$

The chosen templates are 1, $1+\cos\theta$ and $\cos^2\theta$ for the polar distribution, and 1, $1+\cos(2\phi)$ and $1+\cos\phi$ for the azimuthal. The coefficients $\alpha^{(\prime)}$, $\beta^{(\prime)}$ and $\gamma^{(\prime)}$ are determined by fitting the templates to the measured angular distributions. The integral of the template distributions is normalized to 1 before the fitting procedure. The normalisation factor, $1/\sigma$, reflects the number of entries in the measured distributions. It is determined in the fitting procedure as well, using the extended maximum likelihood method [71]. This method is chosen over the maximum likelyhood method as it shows a more stable behaviour. The fitting procedure is implemented using the *roofit* toolkit [85].

The templates are created as follows. First, the angular distributions as obtained from the MC simulation without acceptance restrictions (without detector simulation) are weighted in a way to reproduce the desired shapes. The so obtained templates are called *truth-templates* in the following. The weights are calculated by dividing the analytical template description by the angular distributions obtained from the MC simulation, without detector simulation and without acceptance restrictions. Then, the same weights are applied to the MC distributions after detector simulation. These templates, called *reco-templates* in the following, can directly be fitted to the measured angular distributions. The fit of the reco-templates to the measured distributions is done independently for each p_{T} bin of the analysis.

A closure test is performed by fitting the truth-templates to the angular distributions obtained from simulated events without detector simulation. The true spectrum is recovered by the fit as shown in Fig. 7.12 (a) and (b). The closure test on MC events after detector simulation is shown in subfigures (c) and (d). The results on the measured data are displayed in subfigures (e) and (f). The data distributions are well described by the reco-templates.

The coefficients $A_{0,2}$ are calculated from the fit parameters as:

$$A_0 = 2\frac{\alpha - \beta + \gamma}{3\alpha + \beta + 3\gamma} \tag{7.9}$$

$$A_2 = \frac{1}{4}\frac{\beta}{\alpha + \beta + \gamma}. \tag{7.10}$$

The measured p_{T} dependence of $A_{0,2}$ using this method is listed in Tab. 7.1. The results are compatible with the ones obtained using method 1, as will be discussed in more detail in the next section.

7.4. Comparison of method 1 and 2

The results obtained from the two methods described above are compared in Fig. 7.13 and Tab. 7.1. When using simulated events without detector simulation (truth) both methods produce virtually identical results. All deviations are negligible. The results obtained when applying both methods to data agree within 1.5 standard deviations. However, the statistical uncertainties of the measured coefficients A_i from method 1 are larger (by 50% or more for A_0) compared to those of method 2 (cf. Tab. 7.1). This is largely due to the acceptance correction factors applied in method 1 which naturally increase the statistical uncertainty of the result. The influence on the systematic uncertainties, however, is not obvious at all. It is expected that the reduction of the statistical uncertainty in method 2 is counteracted by an increase of the systematic uncertainties as both methods use the same measured information. However, as a deeper investigation showed, method 2 yields overall slightly smaller uncertainties compared to method 1. As the central value of both methods is very similar and no systematic discrepancy is observed, only results of method 2 will be considered in the following.

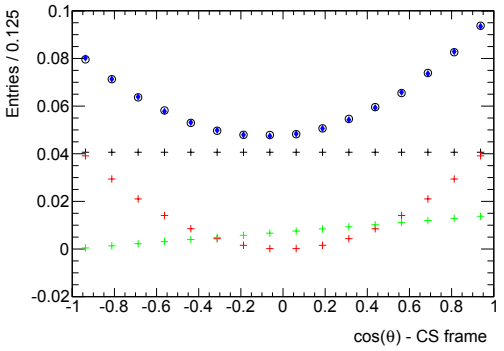

(a) PYTHIA truth - $\cos(\theta)$

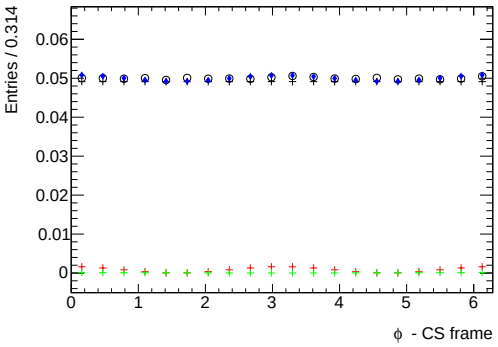

(b) PYTHIA truth - ϕ

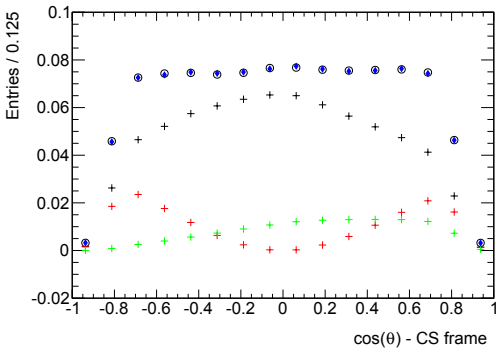

(c) PYTHIA full sim - $\cos(\theta)$

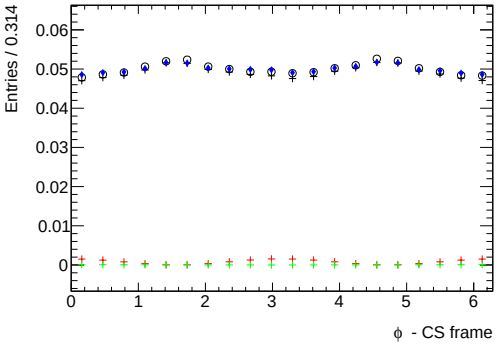

(d) PYTHIA full sim - ϕ

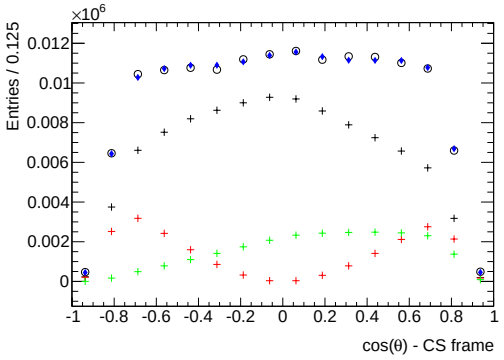

(e) Measured $\cos(\theta)$ distribution; templates include beam crossing angle.

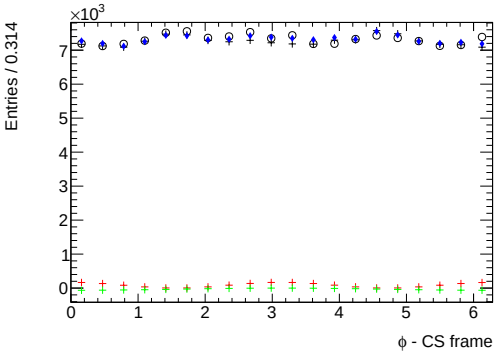

(f) Measured ϕ distribution; templates include beam crossing angle.

Figure 7.12.: Result of the template fit to: PYTHIA simulation without detector simulation (a,b); PYTHIA simulation including detector effects (c,d) with templates generated from the same simulated event sample; measured data (e,f) with templates generated from PYTHIA simulation and corrected for the beam crossing angle. Shown is the p_{T} range $15\,\mathrm{GeV/c} < p_{\mathrm{T}}(\mu\mu) < 20\,\mathrm{GeV/c}$. The original distributions are displayed as open circles. The 3 templates as crosses (black: 1; green: $1+\cos\theta$, $1+\cos\phi$; red: $\cos^2\theta$, $1+\cos(2\phi)$) and the sum of the templates, obtained from the fit, as solid diamonds. In all cases the fitted templates describe the original distributions very well. Note that the histograms shown in (a)-(d) are normalized to an integral of one.

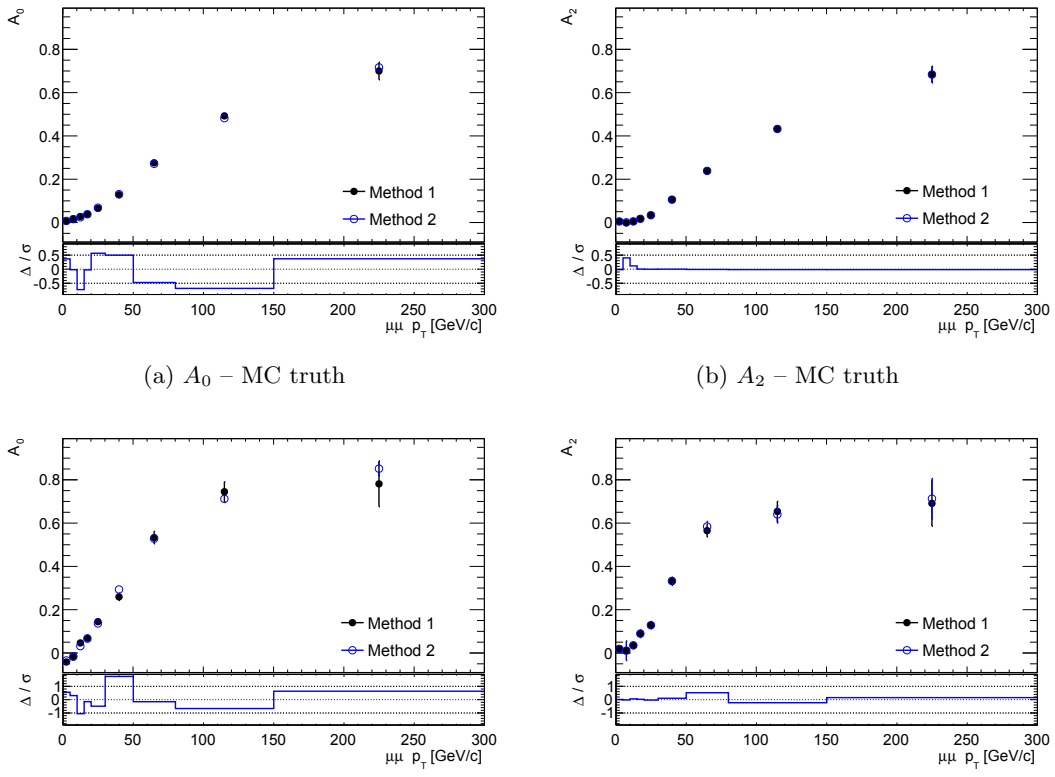

(a) A_0 – MC truth

(b) A_2 – MC truth

(c) A_0 – data

(d) A_2 – data

Figure 7.13.: Dependence of $A_{0,2}$ on the transverse momentum of the di-muon pair $p_{\mathrm{T}}(\mu\mu)$ obtained using extraction methods 1 and 2. (a,b): Results from PYTHIA simulation without detector simulation (truth). (c,d): Results from measured data. The PYTHIA simulation is used to correct the data distributions (method 1) and to create the templates used in method 2.

	Method 1		Method 2	
$p_{\mathrm{T}}(\mu\mu)$ [GeV/c]	A_0	A_2	A_0	A_2
0 - 5	-0.042 ± 0.011	0.019 ± 0.014	-0.034 ± 0.006	0.019 ± 0.008
5 - 10	-0.019 ± 0.009	0.012 ± 0.012	-0.015 ± 0.006	0.011 ± 0.046
10 - 15	0.046 ± 0.012	0.034 ± 0.015	0.032 ± 0.008	0.036 ± 0.010
15 - 20	0.069 ± 0.015	0.089 ± 0.018	0.066 ± 0.010	0.090 ± 0.014
20 - 30	0.145 ± 0.014	0.129 ± 0.017	0.136 ± 0.009	0.128 ± 0.013
30 - 50	0.259 ± 0.017	0.331 ± 0.018	0.294 ± 0.010	0.333 ± 0.015
50 - 80	0.533 ± 0.029	0.565 ± 0.029	0.528 ± 0.012	0.584 ± 0.024
80 - 150	0.745 ± 0.047	0.654 ± 0.047	0.712 ± 0.017	0.640 ± 0.040
150 - 300	0.781 ± 0.105	0.691 ± 0.105	0.852 ± 0.035	0.713 ± 0.093

Table 7.1.: Coefficients $A_{0,2}$ of the angular distributions in dependence of the transverse momentum (p_{T}) of the final state di-muon pair. Coefficients extracted using method 1 and method 2 are shown with statistical uncertainties only.

7.5. Systematic uncertainties

Several sources of systematic uncertainties on the angular coefficients are studied using the PYTHIA MC event sample after detector reconstruction. They are listed in the following in order of significance. Figures illustrating the systematic variations of the coefficients $A_{0,2}$ are presented for the four largest systematics.

- Alignment uncertainties (cf. Fig. 7.16a,b):
  As described in sec. 6.7.2 a remaining uncertainty on the inner detector alignment exists. A correction within the uncertainty has been applied to the MC events in order to study the impact on the angular coefficients. As it turns out the alignment significantly impacts $A_{0,2}$, in particular in the low transverse momentum region. The absolute deviations from the nominal MC are up to 0.05 for A_0 and up to 0.04 for A_2.

- Variation of the rapidity spectrum (y) (cf. Fig. 7.16c,d):
  The simulated rapidity spectrum (after detector simulation) of the di-muon pairs does not perfectly match the measured one. As no unfolded measurement of the y spectrum with the needed precision is available for the time being, differences between the MC predictions from the generators PYTHIA and AlpGEN are used to estimate the systematic uncertainty on the angular coefficients. The variation of the measured angular coefficients between using one of the two generators in the extraction is assigned as systematic uncertainty. This is a significant contribution to the systematic uncertainty, although the predictions of both generators after detector simulation nicely envelop the measured distribution (cf. Fig. 7.14). It even contributes the largest uncertainty on A_0. A maximum absolute deviation w.r.t. the nominal MC of 0.06 on A_0 and 0.02 on A_2 is observed.

- Momentum scale dependence (cf. Fig. 7.16e,f):
  The momentum scale correction for the MC samples consists of two independent contributions: a charge independent correction and on top of it a charge dependent factor. Uncertainties on the momentum scale correction factors corresponding to one standard deviation are carefully evaluated and provided by ATLAS. These are used to calculate up/down variations of both contributions independently. The maximum variation in the angular coefficients from one up/down variation is assigned as systematic uncertainty. The uncertainty due to each momentum scale factor is added in quadrature. A maximum uncertainty on A_0 of 0.014 in the highest p_{T} bin is observed and much smaller uncertainties elsewhere. A_2 is very sensitive to the momentum scale in the low p_{T} region with systematic deviations up to 0.036.

- PDFs (cf. Fig. 7.17a,b):
  The *CT10* PDF and its error sets are used to estimate the uncertainty due to the used PDF on the extraction of the angular coefficients from the measured data. MC events are reweighted to each of the PDF error sets before creating the templates used in method 2. The uncertainty on $A_{0,2}$ is calculated in each p_{T} bin using Eq. (6.8) described in sec. 6.7.1. The PDF uncertainty is small in the whole p_{T} region, with a maximum of 0.015 on A_0 and 0.007 on A_2.

- Momentum smearing:
  To match the MC prediction of the width of the Z-peak to the measured width

an additional smearing of the muon momenta is applied to the simulated events. The uncertainty on the magnitude of the smearing translates into a systematic uncertainty on the measured angular coefficients. It is determined by varying the amount of smearing. A maximum deviation of 0.007 w.r.t. the nominal MC is observed on A_0 and A_2, which is one order of magnitude less than the alignment uncertainty.

- Variations of the $p_{\mathrm{T}}(\mu\mu)$ spectrum:
  The true transverse momentum spectrum of the Z/γ^* system is measured precisely in [86]. Hence the simulated spectrum is reweighted to match the measured one. It is then varied within the uncertainties on the measurement. The corresponding changes of the angular coefficients is assigned as systematic uncertainty. This is the smallest systematic uncertainty compared to the other studied sources with a maximum deviation w.r.t. the nominal MC of $6 \cdot 10^{-4}$ on A_0 and 0.002 on A_2.

  Note that in general the angular distributions are very sensitive to the transverse momentum spectrum of the di-muon pairs, in particular the azimuthal one. This can be seen when studying events simulated using the original PYTHIA MC11 tune [39] without reweighting the transverse momentum distribution of the di-muon pairs to the measured one. In this case the predicted azimuthal angular distribution changes significantly, as do the values of the measured coefficient A_2 which is illustrated in Fig. 7.15.

- Background:
  The contamination of the selected event sample with events from background processes is below 0.5%. It has no significant impact on this analysis and is hence neglected.

The individual uncertainty contributions for each p_{T} bin as well as the total systematic uncertainty are listed for the angular coefficients $A_{0,2,3,4}$ in Tabs. 7.2 - 7.5, respectively.

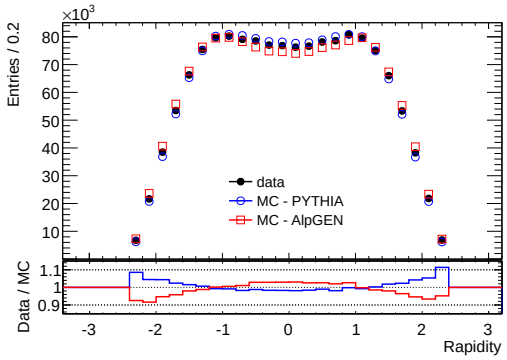

Figure 7.14.: Comparison of the rapidity distribution observed in data with simulations from PYTHIA and AlpGEN.

$p_T(\mu\mu)$ [GeV/c]	Alignment	p scale	p smearing	y	$p_T(\mu\mu)$	PDF	total
0–5	0.0131	0.0058	0.0037	0.0597	0.0001	0.0144	0.0631
5–10	0.0099	0.0088	0.0064	0.0591	0.0002	0.0148	0.0626
10–15	0.0294	0.0032	0.0011	0.0588	$< 10^{-4}$	0.0146	0.0675
15–20	0.0481	0.0048	0.0010	0.0575	0.0001	0.0145	0.0765
20–30	0.0204	0.0060	0.0023	0.0542	0.0000	0.0138	0.0599
30–50	0.0151	0.0041	0.0009	0.0528	0.0003	0.0137	0.0568
50–80	0.0088	0.0034	0.0028	0.0420	0.0002	0.0133	0.0452
80–150	0.0326	0.0054	0.0040	0.0275	0.0006	0.0106	0.0445
150–300	0.0213	0.0145	0.0077	0.0106	0.0004	0.0068	0.0297

Table 7.2.: Systematic uncertainties on the angular coefficient A_0.

$p_T(\mu\mu)$ [GeV/c]	Alignment	p scale	p smearing	y	$p_T(\mu\mu)$	PDF	total
0–5	0.0303	0.0165	0.0020	0.0033	0.0022	0.0019	0.0348
5–10	0.0222	0.0328	0.0057	0.0039	0.0005	0.0029	0.0403
10–15	0.0259	0.0349	0.0051	0.0030	0.0001	0.0027	0.0439
15–20	0.0046	0.0200	0.0048	0.0052	0.0004	0.0038	0.0221
20–30	0.0322	0.0174	0.0027	0.0070	0.0004	0.0035	0.0376
30–50	0.0193	0.0079	0.0066	0.0146	0.0010	0.0052	0.0268
50–80	0.0395	0.0086	0.0027	0.0158	0.0001	0.0048	0.0437
80–150	0.0156	0.0116	0.0072	0.0092	0.0005	0.0033	0.0230
150–300	0.0196	0.0088	0.0072	0.0062	0.0019	0.0072	0.0247

Table 7.3.: Systematic uncertainties on the angular coefficient A_2.

$p_T(\mu\mu)$ [GeV/c]	Alignment	p scale	p smearing	y	$p_T(\mu\mu)$	PDF	total
0–5	0.0281	0.0316	0.0065	0.0001	0.0001	0.0003	0.0428
5–10	0.0344	0.0391	0.0014	0.0012	0.0001	0.0007	0.0521
10–15	0.0102	0.0361	0.0025	0.0008	$< 10^{-4}$	0.0007	0.0376
15–20	0.0168	0.0303	0.0012	0.0001	$< 10^{-4}$	0.0003	0.0347
20–30	0.0176	0.0287	0.0024	0.0002	$< 10^{-4}$	0.0007	0.0338
30–50	0.0218	0.0286	0.0023	0.0005	0.0001	0.0010	0.0360
50–80	0.0099	0.0310	0.0024	0.0010	$< 10^{-4}$	0.0020	0.0327
80–150	0.0074	0.0348	0.0056	0.0020	$< 10^{-4}$	0.0017	0.0361
150–300	0.0920	0.0536	0.0083	0.0027	0.0001	0.0047	0.1069

Table 7.4.: Systematic uncertainties on the angular coefficient A_3.

$p_T(\mu\mu)$ [GeV/c]	Alignment	p scale	p smearing	y	$p_T(\mu\mu)$	PDF	total
0–5	0.0012	0.0036	0.0029	0.0022	$< 10^{-4}$	0.0034	0.0062
5–10	0.0186	0.0044	0.0024	0.0030	$< 10^{-4}$	0.0034	0.0198
10–15	0.0079	0.0066	0.0041	0.0032	$< 10^{-4}$	0.0033	0.0120
15–20	0.0111	0.0027	0.0016	0.0024	$< 10^{-4}$	0.0030	0.0122
20–30	0.0101	0.0038	0.0022	0.0025	$< 10^{-4}$	0.0027	0.0116
30–50	0.0134	0.0040	0.0026	0.0012	$< 10^{-4}$	0.0027	0.0145
50–80	0.0320	0.0023	0.0011	0.0004	$< 10^{-4}$	0.0024	0.0322
80–150	0.0464	0.0019	0.0007	0.0002	$< 10^{-4}$	0.0029	0.0465
150–300	0.1481	0.0120	0.0061	0.0048	0.0002	0.0032	0.1488

Table 7.5.: Systematic uncertainties on the angular coefficient A_4.

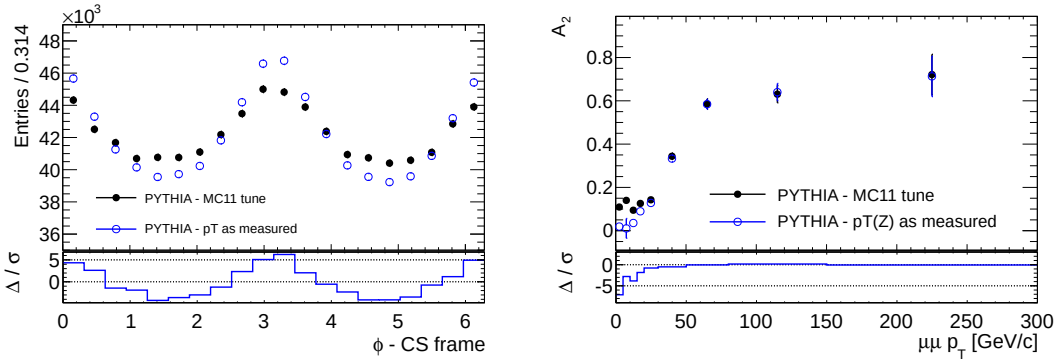

(a) (b)

Figure 7.15.: Impact of the simulated transverse momentum distribution of the dimuon pair on the simulated azimuthal angular distribution in the range $5\,\mathrm{GeV/c} < p_T(Z) < 10\,\mathrm{GeV/c}$ (a) and the measured coefficient A_2 (b). Compared is the original PYTHIA simulation using the MC11 tune (filled circles) and the same simulation with the $p_T(Z)$ distribution reweighted to the measured one (open circles).

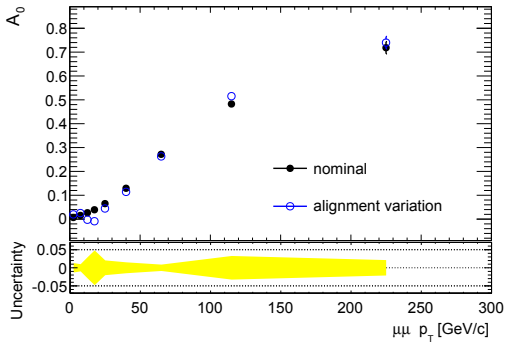

(a) A_0 – Alignment uncertainty

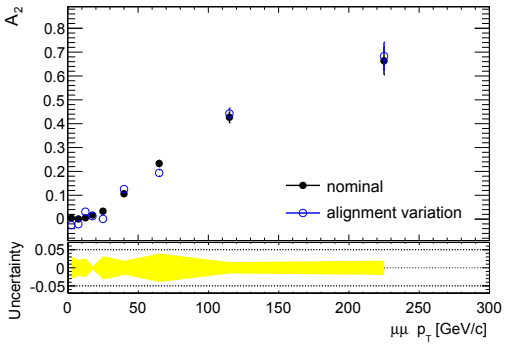

(b) A_2 – Alignment uncertainty

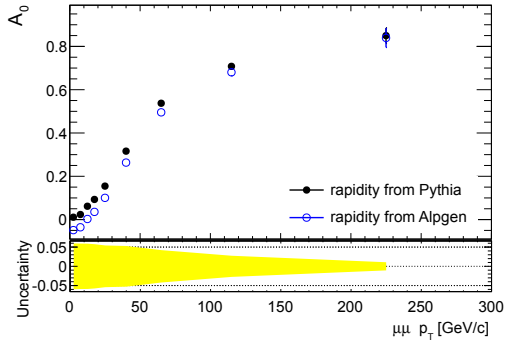

(c) A_0 – Uncertainty on rapidity spectrum

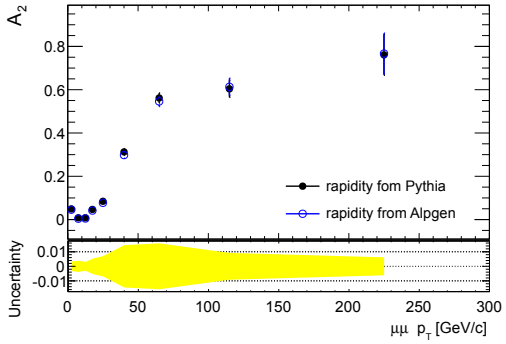

(d) A_2 – Uncertainty on rapidity spectrum

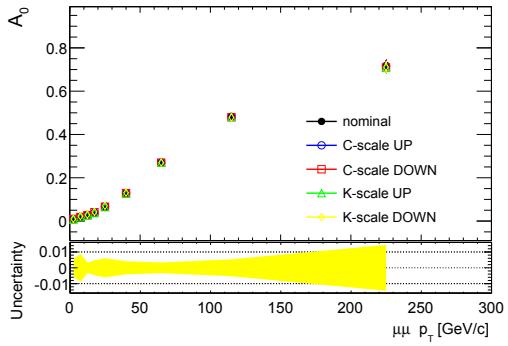

(e) A_0 – Corrections to the MC events

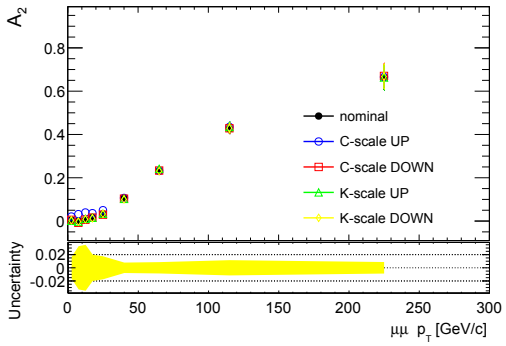

(f) A_2 – Corrections to the MC events

Figure 7.16.: Systematic uncertainties on the angular coefficients $A_{0,2}$ from several sources. The absolute systematic uncertainty is shown in the lower canvas of each plot. The $A_{0,2}$ values themselves are presented for all variations in the upper canvases.

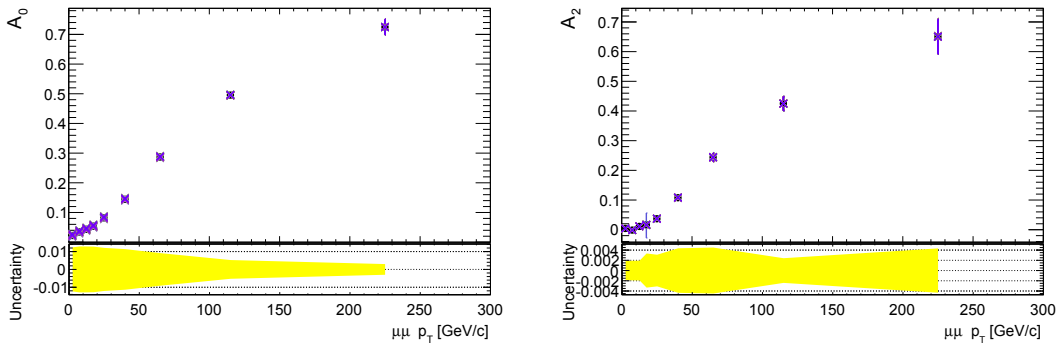

(a) A_0 – PDF Systematic

(b) A_2 – PDF Systematic

Figure 7.17.: Systematic uncertainty on $A_{0,2}$ due to the uncertainty on the PDF. The absolute systematic uncertainty is shown in the lower canvases. The distributions of $A_{0,2}$ for all 52 error sets of the CT10 PDF are overlaid in the upper canvases.

7.6. Results

The coefficients $A_0(p_\mathrm{T})$, $A_2(p_\mathrm{T})$, $A_3(p_\mathrm{T})$ and $A_4(p_\mathrm{T})$ describing the angular distributions of muons originating from Z/γ^* decays (cf. eqs. (7.1),(7.2)) are measured using two different techniques, both yielding similar results. The results presented in the following are obtained using method 2.

The measured dependence of A_i on the transverse momentum $p_\mathrm{T}(\mu\mu)$ of the intermediate state is compared to predictions from the MC generators PYTHIA, AlpGEN, MC@NLO and MadGraph in Fig. 7.18. For details on the MC generators see section 3.1. Note that the MadGraph simulation is using the default MadGraph tune and imposing a cut on the minimum transverse momentum of $p_\mathrm{T}(\mu\mu) > 10\,\mathrm{GeV/c}$. Nevertheless, MadGraph describes all measured angular coefficients very well except for A_4, whereas PYTHIA, the standard generator, describes the data worst. This is expected as PYTHIA only simulates the $q\bar{q}$ annihilation process in the used event sample. Quark–gluon initial states are not considered, but make up a significant fraction of the data events. All other simulated event samples include both production processes (cf. sec. 2.2). Overall, the AlpGEN simulation yields the best agreement with the measured angular coefficients $A_{0,2,3}$. However, due to the size of the uncertainties a meaningful discrimination between predictions from AlpGen, MC@NLO and MadGraph is not possible. The picture changes when looking at the coefficient A_4 which is directly related to the forward–backward asymmetry via $A_{fb} = \frac{3}{8}A_4$. The AlpGEN and MadGraph predictions do not describe the measured data at all in the low $p_\mathrm{T}(\mu\mu)$ region. The reason for this is unclear. PYTHIA, on the other hand, describes $A_4(p_\mathrm{T})$ very well, even better than MC@NLO. This is in agreement with the findings in chapter 6 where a good agreement between the PYTHIA prediction and the measured forward–backward asymmetry versus invariant $\mu\mu$ mass distribution is observed.

The presented measurement of the coefficients of the angular distributions is the first one done with data from the LHC. A similar measurement has recently been published by the CDF collaboration [87] presenting results obtained from $p\bar{p}$ collisions at a center-of-mass energy of $\sqrt{s} = 1.96$ TeV. Results of the presented measurement are compared

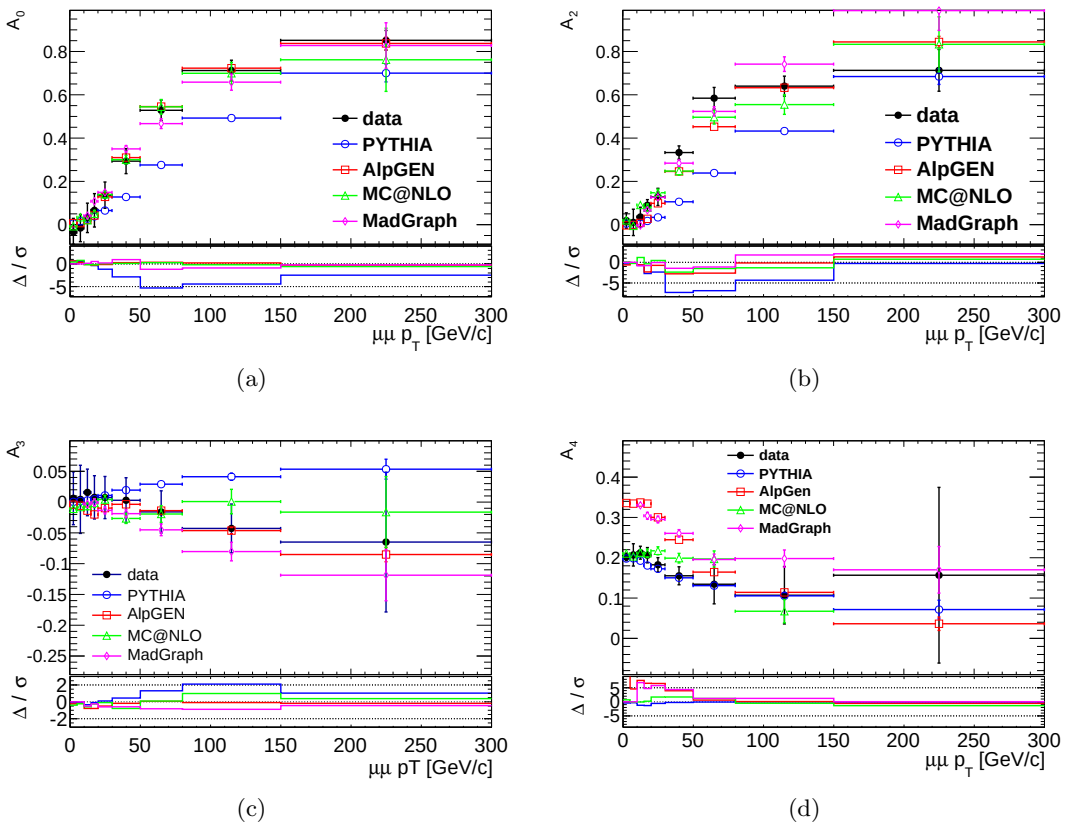

Figure 7.18.: Dependence of the angular coefficients on the transverse momentum of the di-muon pair $p_{\mathrm{T}}(\mu\mu)$ as extracted from data (black dots), including all systematics. MC predictions from different generators are shown for comparison.

to results from the CDF collaboration in Fig. 7.19. Both measurements of the angular distributions $A_{0,2,3}$ agree well. The measured slope of $A_3(p_{\mathrm{T}})$ is in particular in agreement with the recent prediction by [88] and the AlpGen and MadGraph simulations. Only PYTHIA, which is known to model the angular distributions poorly, predicts a positive slope of $A_3(p_{\mathrm{T}})$, in contrast to the measurement. The remaining coefficient A_4 agrees poorly in the low $p_{\mathrm{T}}(Z)$ region with the CDF measurement due to different mass regions used both analyses for selecting the di-lepton pairs in. The PYTHIA simulation describes the measured $A_4(p_{\mathrm{T}})$ dependence very well whereas AlpGen and MadGraph predict larger values of A_4, especially in the low $p_{\mathrm{T}}(Z)$ region.

The precision of the present measurement is limited by systematic uncertainties. The most significant contributions originate from the remaining uncertainty on weak mode misalignments of the tracking detector and the rapidity spectrum of the di-muon pair. The latter contribution will shrink significantly once a measurement of the differential cross section $\frac{d\sigma}{dy}$ of Z/γ^* production becomes available. In spite of the uncertainties, first sensitivity to theory predictions is achieved and subtle differences of individual MC generators become visible in this measurement. It more than doubles the studied range of transverse momentum of the di-muon pair in comparison to previous measurements at hadron colliders.

$p_{\mathrm{T}}(\mu\mu)$ [GeV/c]	A_0	A_2	A_3	A_4
0 - 5	0.011 ± 0.056	0.049 ± 0.038	-0.016 ± 0.045	0.204 ± 0.452
5 - 10	0.023 ± 0.044	0.008 ± 0.063	-0.005 ± 0.052	0.212 ± 0.461
10 - 15	0.062 ± 0.054	0.008 ± 0.045	-0.008 ± 0.038	0.208 ± 0.457
15 - 20	0.093 ± 0.057	0.047 ± 0.026	-0.008 ± 0.035	0.201 ± 0.449
20 - 30	0.155 ± 0.041	0.084 ± 0.053	-0.013 ± 0.034	0.180 ± 0.424
30 - 50	0.316 ± 0.068	0.313 ± 0.145	-0.002 ± 0.042	0.153 ± 0.392
50 - 80	0.537 ± 0.045	0.562 ± 0.170	0.016 ± 0.042	0.140 ± 0.376
80 - 150	0.708 ± 0.036	0.604 ± 0.048	0.040 ± 0.040	0.091 ± 0.308
150 - 300	0.850 ± 0.048	0.761 ± 0.103	0.089 ± 0.117	0.102 ± 0.382

Table 7.6.: Measured angular coefficients in dependence of the transverse momentum $p_{\mathrm{T}}(\mu\mu)$. Uncertainties include statistical and systematic errors.

7.6.1. Gluon spin $S(g)$

As outlined in section 2.2, the angular distributions are sensitive to the spin of the gluon $S(g)$. This is expressed in the Lam-Tung relation, stating that $A_0(p_{\mathrm{T}}) = A_2(p_{\mathrm{T}})$ for all p_{T} if $S(g) = 1$. Predictions of the angular coefficients $A_{0,2}$ are made for a scalar ($S(g) = 0$) and a vector ($S(g) = 1$) gluon using the MadGraph event generator (cf. Fig. 7.6). Comparing the predictions with the measured angular coefficients (cf. Fig. 7.18) reveals a clear preference of the data for a gluon with spin $S(g) = 1$. This is more clearly visible by studying the difference $A_0(p_{\mathrm{T}}) - A_2(p_{\mathrm{T}})$, which is shown in Fig. 7.20. The average difference is compatible with zero: $\langle A_0(p_{\mathrm{T}}) - A_2(p_{\mathrm{T}})\rangle = 0.002 \pm 0.078$. Note that the Lam-Tung relation is not exact any more when considering higher orders of α_s in the calculation of the angular distributions. A_2 is expected to change up to 20% whereas A_0 remains nearly unaffected [84]. The hypothesis of a vector like gluon ($A_0(p_{\mathrm{T}}) - A_2(p_{\mathrm{T}}) = 0$) is tested using a Kolmogorov-Smirnov test [89], neglecting higher order corrections. It yields a probability of 42% that this hypothesis is true. Applying the same test to the MadGrahp prediction for a scalar gluon yields a probability of 10^{-16}.

This result is in agreement with previous measurements of the spin of the gluon which was originally determined in studies of the angular distributions of 3-jet events in e^+e^- collisions [90].

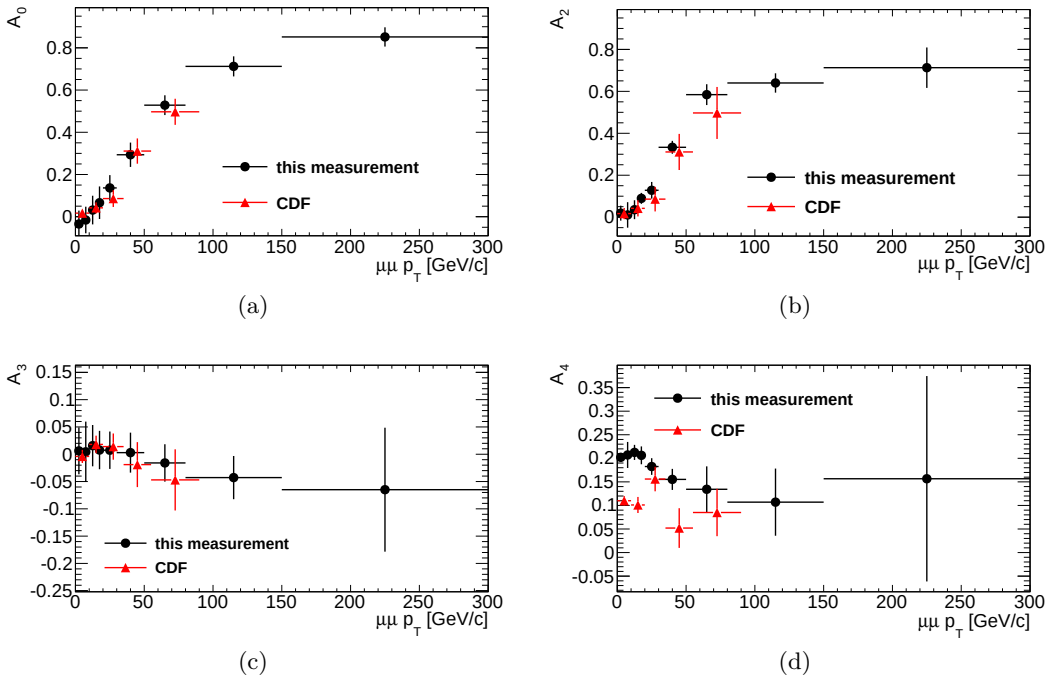

Figure 7.19.: Measured angular coefficients A_i (black circles) in comparison to the results from CDF [87] (red triangles). Good agreement is observed for $A_{0,2,3}$. A_4 differs between both analyses due to different mass ranges considered for the di-lepton pairs.

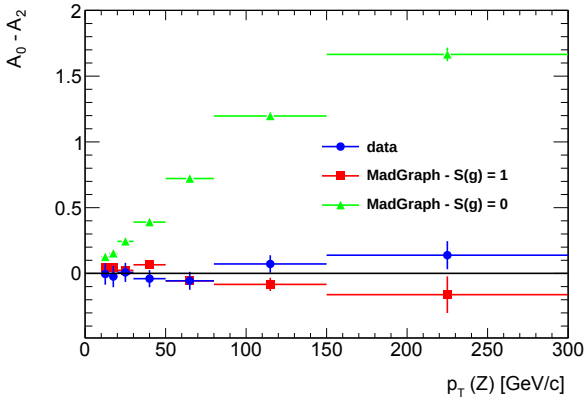

Figure 7.20.: $A_0 - A_2$ is plotted for the MadGraph predictions for a vector gluon (red squares) and a scalar gluon (green triangles) in comparison to the measured data (blue circles).

8. Summary

The main result of the present work is the measurement of the weak mixing angle, $\sin^2\theta_W^{\text{eff}}$, in the decay of Z bosons into pairs of muons, produced in proton–proton collisions at the LHC and observed with the ATLAS detector.

The LHC extended experimental particle physics into a new energy regime since the operation started in 2010 at a center-of-mass energy of $\sqrt{s} = 7\,\text{TeV}$. In 2011 a large data sample with an integrated luminosity of $\int \mathscr{L}\text{dt} = 4.70\,\text{fb}^{-1}$ was recorded with the ATLAS detector. It is used in this work to study the angular distributions of the final state muon (μ^-) in the reaction $pp \to Z/\gamma^* + X \to \mu^+\mu^- + X$. The angular distributions are sensitive to several aspects of the involved particles and interactions. One is the weak mixing angle which is accessible through the forward–backward asymmetry in $Z \to \mu^+\mu^-$ decays. A value of

$$\sin^2\theta_W^{\text{eff}} = 0.22937 \pm 0.00087(\text{stat}) \pm 0.00119(\text{sys})$$

is measured with a precision similar to the one reached in $p\bar{p}$ collisions at the Tevatron with an integrated luminosity of $\int \mathscr{L}\text{dt} = 5\,\text{fb}^{-1}$. It is compatible with previous measurements (cf. Fig. 8.1).

To achieve such a level of precision detailed studies concerning the muon reconstruction efficiency and the alignment of the tracking detectors were performed (cf. sections 5 and 6.7.2), the latter leading to an improved understanding of the geometry deformations within the ATLAS detector.

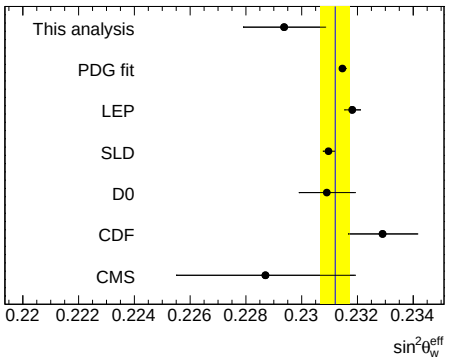

Figure 8.1.: Results from various measurements of $\sin^2\theta_W^{\text{eff}}$ in comparison to the value obtained in this analysis. The vertical bar indicates the average over all shown values, excluding the global fit, with its uncertainty.

Although $\sin^2\theta_W^{\text{eff}}$ has already been measured with higher accuracy in e^+e^- collisions at LEP and SLD, this is an important result, as both the complex initial state in proton–proton collisions compared to e^+e^- collisions and the by far increased collision energy w.r.t. previous hadron colliders might have resulted in unexpected effects. And not least, the understanding of the detector and the simulation is brought forward.

In addition to the integral forward–backward asymmetry the differential angular distributions ($d\sigma/d\cos\theta$ and $d\sigma/d\phi$) were measured in a small region around the Z mass. This is the first measurement of the angular distribution from Z boson decays at the LHC. Compared to the latest measurement from proton–antiproton collisions [87] the transverse momentum range is significantly increased while comparable uncertainties are achieved. The angular distribution is sensitive to the relative composition of $q\bar{q}$ annihilation and qg scattering in the initial state. Although the comparison to the $p\bar{p}$ results from CDF [87] seems to suggest a larger contribution of the qg initial state in the LHC data, the size of the uncertainties does not allow a conclusive statement.

In addition to the composition of the initial state, the angular distributions are also sensitive to the spin of the gluon through the so called Lam-Tung relation [32]. For two coefficients of the angular distribution it states that they are equal, $A_0(p_\mathrm{T}) = A_2(p_\mathrm{T})$, in the case that the gluon has spin $S(g) = 1$. The measured coefficients obey the Lam-Tung relation in the studied transverse momentum range of $0 \leq p_\mathrm{T}(Z) \leq 300\,\mathrm{GeV/c}$. An average difference of $\langle A_0(p_\mathrm{T}) - A_2(p_\mathrm{T})\rangle = 0.002 \pm 0.078$ is measured.

The study of angular distributions is particularly exciting in the light of the resonance at a mass of $m \simeq 126\,\mathrm{GeV/c^2}$, which has been discovered by ATLAS and CMS in 2012 and is thought to be the Higgs–Boson. A measurement of its spin and CP eigenstate, which is possible on the basis of angular correlations in the decay channel $H \to ZZ \to 4l$, will be an important step to unravel the identity of this Higgs candidate.

Bibliography

[1] P. W. Higgs. "Broken Symmetries and the Masses of Gauge Bosons".
In: *Phys. Rev. Lett.* 13 (16 1964), pp. 508–509.
DOI: 10.1103/PhysRevLett.13.508.
URL: http://link.aps.org/doi/10.1103/PhysRevLett.13.508.

[2] L. Evans and P. Bryant. "LHC Machine". In: *JINST* 3 (2008), S08001.
DOI: 10.1088/1748-0221/3/08/S08001.

[3] ATLAS Collaboration.
"The ATLAS Experiment at the CERN Large Hadron Collider".
In: *JINST* 3 (2008), S08003. DOI: 10.1088/1748-0221/3/08/S08003.

[4] S. Chatrchyan et al. "The CMS experiment at the CERN LHC".
In: *JINST* 3 (2008), S08004. DOI: 10.1088/1748-0221/3/08/S08004.

[5] D. Schaile. "Tests of the Electroweak Theory at LEP".
In: *Fortsch.Phys.* 42 (1994), pp. 429–484.

[6] B. Odom et al. "New Measurement of the Electron Magnetic Moment Using a One-Electron Quantum Cyclotron". In: *Phys. Rev. Lett.* 97 (3 2006), p. 030801.
DOI: 10.1103/PhysRevLett.97.030801.
URL: http://link.aps.org/doi/10.1103/PhysRevLett.97.030801.

[7] D. H. Perkins. *Introduction to High Energy Physics*. 4th ed. Cambridge, 2001.

[8] S. N. M. T. Morii C. S. Lim. *The Physics of the Standard Model and beyond*.
1st ed. World Scientific, 2004.

[9] M. P. D. Schroeder. *An Introduction to Quantum Field Theory*.
Westview Press, 1995.

[10] M. Gell-Mann.
"The interpretation of the new particles as displaced charge multiplets".
In: *Il Nuovo Cimento (1955-1965)* 4 (0 1956). 10.1007/BF02748000, pp. 848–866.
ISSN: 1827-6121. URL: http://dx.doi.org/10.1007/BF02748000.

[11] Y. Nambu and G. Jona-Lasinio. "Dynamical Model of Elementary Particles Based on an Analogy with Superconductivity. I".
In: *Phys. Rev.* 122 (1 1961), pp. 345–358. DOI: 10.1103/PhysRev.122.345.
URL: http://link.aps.org/doi/10.1103/PhysRev.122.345.

[12] J. Goldstone, A. Salam, and S. Weinberg. "Broken Symmetries".
In: *Phys. Rev.* 127 (3 1962), pp. 965–970. DOI: 10.1103/PhysRev.127.965.
URL: http://link.aps.org/doi/10.1103/PhysRev.127.965.

[13] M. Kobayashi and T. Maskawa.
"CP-Violation in the Renormalizable Theory of Weak Interaction".
In: *Progress of Theoretical Physics* 49.2 (1973), pp. 652–657.
DOI: 10.1143/PTP.49.652. URL: http://ptp.ipap.jp/link?PTP/49/652/.

[14] ATLAS Collaboration. "Observation of a new particle in the search for the Standard Model Higgs boson with the ATLAS detector at the LHC". In: *Phys.Lett.B* (2012). DOI: 10.1016/j.physletb.2012.08.020. arXiv:1207.7214 [hep-ex].

[15] CMS Collaboration. "Observation of a new boson at a mass of 125 GeV with the CMS experiment at the LHC". In: *Phys.Lett.B* (2012). DOI: 10.1016/j.physletb.2012.08.021. arXiv:1207.7235 [hep-ex].

[16] S. Weinberg. "New Approach to the Renormalization Group". In: *Phys. Rev. D* 8 (10 1973), pp. 3497–3509. DOI: 10.1103/PhysRevD.8.3497. URL: http://link.aps.org/doi/10.1103/PhysRevD.8.3497.

[17] J. Beringer et al. In: *Phys. Rev. D* 86 (010001 2012).

[18] A. Czarnecki and W. J. Marciano. "Electroweak radiative corrections to polarized Moller scattering asymmetries". In: *Phys.Rev.* D53 (1996), pp. 1066–1072. DOI: 10.1103/PhysRevD.53.1066. arXiv:hep-ph/9507420 [hep-ph].

[19] J. Erler and M. J. Ramsey-Musolf. "Weak mixing angle at low energies". In: *Phys. Rev. D* 72 (7 2005), p. 073003. DOI: 10.1103/PhysRevD.72.073003. URL: http://link.aps.org/doi/10.1103/PhysRevD.72.073003.

[20] R. D. Carlini. "The Qweak experiment: a precision measurement of the proton's weak charge". In: *AIP Conference Proceedings* 1261.1 (2010). Ed. by W. Melnitchouk, pp. 172–178. DOI: 10.1063/1.3479339. URL: http://link.aip.org/link/?APC/1261/172/1.

[21] G. P. Zeller et al. "Precise Determination of Electroweak Parameters in Neutrino-Nucleon Scattering". In: *Phys. Rev. Lett.* 88 (9 2002), p. 091802. DOI: 10.1103/PhysRevLett.88.091802. URL: http://link.aps.org/doi/10.1103/PhysRevLett.88.091802.

[22] V. Abazov et al. "Measurement of $\sin^2\theta^{\ell}_{\text{eff}}$ and Z-light quark couplings using the forward-backward charge asymmetry in $p\bar{p} \to Z/\gamma^* \to e^+e^-$ events with $\mathscr{L} = 5.0$ fb^{-1} at $\sqrt{s} = 1.96$ TeV". In: *Phys.Rev.* D84 (2011), p. 012007. DOI: 10.1103/PhysRevD.84.012007. arXiv:1104.4590 [hep-ex].

[23] S. Chatrchyan et al. "Measurement of the weak mixing angle with the Drell-Yan process in proton-proton collisions at the LHC". In: *Phys. Rev. D* 84 (11 2011), p. 112002. DOI: 10.1103/PhysRevD.84.112002. URL: http://link.aps.org/doi/10.1103/PhysRevD.84.112002.

[24] S. Dürr et al. "Ab Initio Determination of Light Hadron Masses". In: *Science* 322 (2008), pp. 1224–1227. DOI: 10.1126/science.1163233.

[25] E. Lobodzinska. "Original author of figure, private communication". (2012).

[26] H1 and ZEUS Collaborations. In: *H1prelim-10-142, ZEUS-prel-10-018* (2010). URL: https://www.desy.de/h1zeus/combined_results/index.php.

[27] TOTEM Collaboration. "First measurement of the total proton-proton cross-section at the LHC energy of $\sqrt{s} = 7\,TeV$". In: *EPL (Europhysics Letters)* 96.2 (2011), p. 21002. URL: http://stacks.iop.org/0295-5075/96/i=2/a=21002.

[28] E. Mirkes and J. Ohnemus. "W and Z polarization effects in hadronic collisions". In: *Phys.Rev.* D50 (1994), pp. 5692–5703. DOI: 10.1103/PhysRevD.50.5692. arXiv:hep-ph/9406381 [hep-ph].

[29] E. Mirkes and J. Ohnemus. "Angular distributions of Drell-Yan lepton pairs at the Tevatron: Order α_s^2 corrections and Monte Carlo studies". In: *Phys.Rev.* D51 (1995), pp. 4891–4904. DOI: 10.1103/PhysRevD.51.4891. arXiv:hep-ph/9412289 [hep-ph].

[30] G. Bella. *Prospects for* $\sin^2\theta_{eff}^{lept}$ *Measurement at ATLAS using* $Z \to \mu\mu$ *Events.* Tech. rep. ATL-PHYS-INT-2010-074. Geneva: CERN, 2010.

[31] C. S. Lam and W.-K. Tung. "Parton-model relation without quantum-chromodynamic modifications in lepton pair production". In: *Phys. Rev. D* 21 (9 1980), pp. 2712–2715. DOI: 10.1103/PhysRevD.21.2712. URL: http://link.aps.org/doi/10.1103/PhysRevD.21.2712.

[32] N. Arteaga-Romero, A. Nicolaidis, and J. Silva. "Z^0 Production at the $\overline{p}p$ Collider and the Spin of the Gluon". In: *Phys. Rev. Lett.* 52 (3 1984), pp. 172–175. DOI: 10.1103/PhysRevLett.52.172. URL: http://link.aps.org/doi/10.1103/PhysRevLett.52.172.

[33] M. Chaichian, M. Hayashi, and K. Yamagishi. "Angular distributions of high-mass dileptons in high-energy hadronic collisions". In: *Phys. Rev. D* 25 (1 1982), pp. 130–142. DOI: 10.1103/PhysRevD.25.130. URL: http://link.aps.org/doi/10.1103/PhysRevD.25.130.

[34] J. Lindfors. "Angular Distribution of Large q_T Muon Pairs in Different Reference Frames". In: *Physica Scripta* 20.1 (1979), p. 19. URL: http://stacks.iop.org/1402-4896/20/i=1/a=003.

[35] C. Lam and W.-K. Tung. "Structure function relations at large transverse momenta in Lepton-pair production processes". In: *Physics Letters B* 80.3 (1979), pp. 228 –231. ISSN: 0370-2693. DOI: 10.1016/0370-2693(79)90204-1. URL: http://www.sciencedirect.com/science/article/pii/0370269379902041.

[36] M. Dobbs et al. "Les Houches guidebook to Monte Carlo generators for hadron collider physics". In: (2004), pp. 411–459. arXiv:hep-ph/0403045 [hep-ph].

[37] F. Siegert. *Monte-Carlo event generation for the LHC.* PhD thesis, Durham University, 2010. URL: http://etheses.dur.ac.uk/484/.

[38] T. Sjostrand, S. Mrenna, and P. Z. Skands. "PYTHIA 6.4 Physics and Manual". In: *JHEP* 05 (2006), p. 026. DOI: 10.1088/1126-6708/2006/05/026. arXiv:hep-ph/0603175.

[39] ATLAS collaboration. *ATLAS tunes of PYTHIA 6 and Pythia 8 for MC11.* Tech. rep. ATL-PHYS-PUB-2011-009. Geneva: CERN, 2011.

[40] P. Golonka and Z. Was. "PHOTOS Monte Carlo: A Precision tool for QED corrections in Z and W decays". In: *Eur.Phys.J.* C45 (2006), pp. 97–107. DOI: 10.1140/epjc/s2005-02396-4. arXiv:hep-ph/0506026 [hep-ph].

[41] M. L. Mangano et al.
"ALPGEN, a generator for hard multiparton processes in hadronic collisions".
In: *JHEP* 07 (2003), p. 001. arXiv:hep-ph/0206293.

[42] J. Butterworth, J. R. Forshaw, and M. Seymour.
"Multiparton interactions in photoproduction at HERA".
In: *Z.Phys.* C72 (1996), pp. 637–646. DOI: 10.1007/s002880050286.
arXiv:hep-ph/9601371 [hep-ph].

[43] G. Corcella et al. "HERWIG 6 : an event generator for hadron emission reactions with interfering gluons (including supersymmetric processes)".
In: *Journal of High Energy Physics.* 1 (2001). http://dro.dur.ac.uk/1548/, 010.

[44] S. Frixione and B. R. Webber.
"Matching NLO QCD computations and parton shower simulations".
In: *JHEP* 0206 (2002), p. 029. arXiv:hep-ph/0204244 [hep-ph].

[45] J. Alwall et al. "MadGraph 5 : Going Beyond". In: *JHEP* 1106 (2011), p. 128.
DOI: 10.1007/JHEP06(2011)128. arXiv:1106.0522 [hep-ph].

[46] I. Bird. "Computing for the Large Hadron Collider". English.
In: *ANNUAL REVIEW OF NUCLEAR AND PARTICLE SCIENCE, VOL 61.*
Ed. by Holstein, BR and Haxton, WC and Jawahery, A. Vol. 61.
Annual Review of Nuclear and Particle Science. 4139 EL CAMINO WAY, PO BOX 10139, PALO ALTO, CA 94303-0897 USA: ANNUAL REVIEWS, 2011, 99–118. ISBN: 978-0-8243-1561-0.
DOI: {10.1146/annurev-nucl-102010-130059}.

[47] M. Baak et al.
Data Quality Status Flags and Good Run Lists for Physics Analysis in ATLAS.
Tech. rep. ATL-COM-GEN-2009-015. Geneva: CERN, 2009.

[48] ATLAS Collaboration. "Muon Reconstruction Performance".
In: *ATLAS-CONF-2010-064* (2010).

[49] ATLAS Collaboration.
"Expected performance of the ATLAS experiment: detector, trigger and physics".
In: *arXiv:0901.0512. CERN-OPEN-2008-020* (2009).

[50] ATLAS Collaboration. *Muon Performance in Minimum Bias pp Collision Data at $\sqrt{s} = 7$ TeV with ATLAS.* Tech. rep. ATLAS-CONF-2010-036.
Geneva: CERN.

[51] S. Amato et al. "LHCb technical proposal".
In: *CERN-LHCC-98-04, CERN-LHCC-P-4* (1998).

[52] P. Giubellino. "The ALICE detector at LHC".
In: *Nucl.Instrum.Meth.* A344 (1994), pp. 27–38.
DOI: 10.1016/0168-9002(94)90647-5.

[53] G. Anelli et al. "The TOTEM experiment at the CERN Large Hadron Collider".
In: *JINST* 3 (2008), S08007. DOI: 10.1088/1748-0221/3/08/S08007.

[54] O. Adriani et al. "The LHCf detector at the CERN Large Hadron Collider".
In: *JINST* 3 (2008), S08006. DOI: 10.1088/1748-0221/3/08/S08006.

[55] CERN. *The LHC Guide.* 2009. URL: http://cds.cern.ch/record/1165534/files/CERN-Brochure-2009-003-Eng.pdf.

[56] G. Aad et al. "The ATLAS Inner Detector commissioning and calibration". In: *Eur.Phys.J.* C70 (2010), pp. 787–821. DOI: 10.1140/epjc/s10052-010-1366-7. arXiv:1004.5293 [physics.ins-det].

[57] ATLAS Collaboration. *Comupter generated images of ATLAS*. 2008. URL: http://cds.cern.ch/record/1095924.

[58] ATLAS Collaboration. *Comupter generated images of the ATLAS inner detector*. 2008. URL: http://cds.cern.ch/record/1095926.

[59] ATLAS Collaboration. *Performance of primary vertex reconstruction in proton-proton collisions at $\sqrt{s}$ =7 TeV in the ATLAS experiment*. Tech. rep. ATLAS-CONF-2010-069. Geneva: CERN, 2010.

[60] J. Biesiada et al. *The Implementation and Performance of ROD DSP Software in the ATLAS Pixel Detector*. Tech. rep. ATL-INDET-INT-2010-006. Geneva: CERN, 2010.

[61] N. Garelli et al. *The Tuning and Calibration of the Charge Measurement of the Pixel Detector*. Tech. rep. ATL-COM-INDET-2010-017. Geneva: CERN, 2009.

[62] ATLAS Collaboration. *Comupter generated images of the ATLAS Muons subsystems*. 2008. URL: http://cds.cern.ch/record/1095929.

[63] ATLAS Collaboration. *Muon reconstruction efficiency in reprocessed 2010 LHC proton-proton collision data recorded with the ATLAS detector*. Tech. rep. ATLAS-CONF-2011-063. Geneva: CERN.

[64] T Cornelissen et al. *Single Track Performance of the Inner Detector New Track Reconstruction (NEWT)*. Tech. rep. ATL-INDET-PUB-2008-002. ATL-COM-INDET-2008-004. Geneva: CERN, 2008.

[65] A. Gelman et al. *Bayesian Data Analysis*. Champman & Hall/CRC, 2004.

[66] ATLAS collaboration. *ATLAS Monte Carlo tunes for MC09*. Tech. rep. ATL-PHYS-PUB-2010-002. Geneva: CERN, 2010.

[67] ATLAS Collaboration. *Measurement of the $W \to \ell\nu$ production cross-section and observation of $Z \to \ell\ell$ production*. Tech. rep. ATLAS-CONF-2010-051. Geneva: CERN.

[68] ATLAS Collaboration. "Measurement of the $W \to l\nu$ and $Z/\gamma* \to ll$ production cross sections in proton-proton collisions at $\sqrt{s} = 7$ TeV with the ATLAS detector. oai:cds.cern.ch:1299479". In: arXiv:1010.2130. CERN-PH-EP-2010-037 (2010).

[69] M. Dittmar, A.-S. Nicollerat, and A. Djouadi. "Z studies at the LHC: an update". In: *Physics Letters B* 583.12 (2004), pp. 111 –120. ISSN: 0370-2693. DOI: 10.1016/j.physletb.2003.09.103. URL: http://www.sciencedirect.com/science/article/pii/S0370269304000760.

[70] J. C. Collins and D. E. Soper. "Angular distribution of dileptons in high-energy hadron collisions". In: *Phys. Rev. D* 16 (1977), 22192225.

[71] R. Barlow.
Statistics: A Guide to The Use of Statistical Methods in the Physical Sciences.
Manchester Physics Series. Wiley, 1989. ISBN: 9780471922957.

[72] B. Efron. "Bootstrap Methods: Another Look at the Jackknife".
In: *The Annals of Statistics* 7.1 (1979), pp. 1–26.

[73] ATLAS Collaboration. *ATLAS Muon Momentum Resolution in the First Pass Reconstruction of the 2010 p-p Collision Data at sqrts = 7 TeV.*
Tech. rep. ATLAS-CONF-2011-046. Geneva: CERN.

[74] ATLAS Collaboration. *A measurement of the ATLAS muon reconstruction and trigger efficiency using J/psi decays.* Tech. rep. ATLAS-CONF-2011-021.
Geneva: CERN, 2011.

[75] C. Gwenlan and P. Loch. *Recommendations for systematic error contributions from PDFs to theoretical predictions.* Tech. rep.
https://indico.cern.ch/getFile.py/access?contribId=1&resId=0&materialId=slides&confId=137359. Geneva: CERN, 2011.

[76] A. Sherstnev and R. Thorne. "Parton Distributions for LO Generators".
In: *Eur.Phys.J.* C55 (2008), pp. 553–575.
DOI: 10.1140/epjc/s10052-008-0610-x. arXiv:0711.2473 [hep-ph].

[77] A. Martin et al. "Parton distributions for the LHC".
In: *Eur.Phys.J.* C63 (2009), pp. 189–285.
DOI: 10.1140/epjc/s10052-009-1072-5. arXiv:0901.0002 [hep-ph].

[78] U. Klein. "Private communication". 2012.

[79] H.-L. Lai et al. "New parton distributions for collider physics".
In: *Phys.Rev.* D82 (2010), p. 074024. DOI: 10.1103/PhysRevD.82.074024.
arXiv:1007.2241 [hep-ph].

[80] ATLAS PDF forum, U. Klein. "Private communication". 2012.

[81] ATLAS collaboration. "Study of alignment-related systematic effects on the ATLAS Inner Detector tracking". In: ATLAS-CONF-2012-141 (2012).

[82] J. Han et al. *Measurement of the Angular Coefficients of Drell-Yan e^+e pairs in the Z Mass Region from in $p\bar{p}$ collisions at $\sqrt{s} = 1.96$ TeV.*
Tech. rep. CDFPUBELECTROWEAKPUBLIC10312. 2011. URL: http://www-cdf.fnal.gov/physics/ewk/2010/Z_angle/angular_public_web/main.html.

[83] S. Chatrchyan et al. "Measurement of the weak mixing angle with the Drell-Yan process in proton-proton collisions at the LHC".
In: *Phys.Rev.* D84 (2011), p. 112002. DOI: 10.1103/PhysRevD.84.112002.
arXiv:1110.2682 [hep-ex].

[84] E. Mirkes. "Angular decay distribution of leptons from W bosons at NLO in hadronic collisions". In: *Nucl.Phys.* B387 (1992), pp. 3–85.
DOI: 10.1016/0550-3213(92)90046-E.

[85] W. Verkerke and D. P. Kirkby. "The RooFit toolkit for data modeling".
In: *eConf* C0303241 (2003), MOLT007. arXiv:physics/0306116 [physics].

[86] K. Müller. *Measurement of the transverse momentum distribution of Z bosons in $pp \to Z \to \mu^+\mu^-$ events produced at $\sqrt{(s)} = 7$ TeV.*
PhD thesis, University of Bonn - in preparation, 2012.

[87] T. Aaltonen et al. "First Measurement of the Angular Coefficients of Drell-Yan e^+e^- pairs in the Z Mass Region from $p\bar{p}$ Collisions at $\sqrt{s} = 1.96$ TeV". In: *Phys.Rev.Lett.* 106 (2011), p. 241801. DOI: 10.1103/PhysRevLett.106.241801. arXiv:1103.5699 [hep-ex].

[88] A. Lipatov, M. Malyshev, and N. Zotov. "Drell-Yan lepton pair production at high energies in the k_t-factorization approach". In: *JHEP* 1112 (2011), p. 117. DOI: 10.1007/JHEP12(2011)117. arXiv:1110.6582 [hep-ph].

[89] Chakravarti, Laha, and Roy. "Handbook of Methods of Applied Statistics". In: vol. I. John Wiley and Sons, 1967, pp. 392–394.

[90] C. Berger et al. "Topology of the Upsilon-decay". In: *Zeitschrift fur Physik C Particles and Fields* 8 (June 1981), pp. 101–114. DOI: 10.1007/BF01547873.

A. Used datasets and PDFs

Name	Ref.	Order	Usage and Remarks
MSTMCal	[76]	LO	Standard PDF in Pythia simultaion
MSTW2008Lo	[77]	LO	Extraction of $\sin^2\theta_W^{\text{eff}}$
CT10	[79]	NLO	Error estimation due to PDFs, 90%CL error sets + α_s variation included

Table A.1.: Overview of the used PDF sets in this thesis.

Prozess	Generator	Event sample identifier
		Signal samples
$Z/\gamma^* \to \mu\mu$	PYTHIA	mc11_7TeV.106047.PythiaZmumu_no_filter.merge.AOD.e815_s1272_s1274_r3043_r2993
$Z/\gamma^* \to \mu\mu$	MC@NLO	mc11_7TeV.106088.McAtNloZmumu_no_filter.merge.AOD.e872_s1310_s1300_r3043_r2993
$Z/\gamma^* \to \mu\mu$	AlpGEN	mc11_7TeV.10766[0..5].AlpgenJimmyZmumuNp[0..5]_pt20.merge.AOD.e835_s1299_s1300_r3043_r2993
		Background channels
$Z/\gamma^* \to \tau\tau$	PYTHIA	mc11_7TeV.106052.PythiaZtautau.merge.AOD.e825_s1349_s1300_r3060_r2993
$W \to \mu\nu + 0$ Jets	AlpGEN + Jimmy	mc11_7TeV.107700.AlpgenJimmyWtaunuNp0_pt20.merge.AOD.e835_s1299_s1300_r3043_r2993
$W \to \mu\nu + 1$ Jets	AlpGEN + Jimmy	mc11_7TeV.107701.AlpgenJimmyWtaunuNp1_pt20.merge.AOD.e835_s1299_s1300_r3043_r2993
$W \to \mu\nu + 2$ Jets	AlpGEN + Jimmy	mc11_7TeV.107702.AlpgenJimmyWtaunuNp2_pt20.merge.AOD.e835_s1299_s1300_r3043_r2993
$W \to \mu\nu + 3$ Jets	AlpGEN + Jimmy	mc11_7TeV.107703.AlpgenJimmyWtaunuNp3_pt20.merge.AOD.e835_s1299_s1300_r3043_r2993
$W \to \mu\nu + 4$ Jets	AlpGEN + Jimmy	mc11_7TeV.107704.AlpgenJimmyWtaunuNp4_pt20.merge.AOD.e835_s1299_s1300_r3043_r2993
$W \to \mu\nu + 5$ Jets	AlpGen + Jimmy	mc11_7TeV.107705.AlpgenJimmyWtaunuNp5_pt20.merge.AOD.e835_s1299_s1300_r3043_r2993
$W \to \tau\nu + 0$ Jets	AlpGen + Jimmy	mc11_7TeV.107700.AlpgenJimmyWtaunuNp0_pt20.merge.AOD.e835_s1299_s1300_r3043_r2993
$W \to \tau\nu + 1$ Jets	AlpGen + Jimmy	mc11_7TeV.107701.AlpgenJimmyWtaunuNp1_pt20.merge.AOD.e835_s1299_s1300_r3043_r2993
$W \to \tau\nu + 2$ Jets	AlpGen + Jimmy	mc11_7TeV.107702.AlpgenJimmyWtaunuNp2_pt20.merge.AOD.e835_s1299_s1300_r3043_r2993
$W \to \tau\nu + 3$ Jets	AlpGen + Jimmy	mc11_7TeV.107703.AlpgenJimmyWtaunuNp3_pt20.merge.AOD.e835_s1299_s1300_r3043_r2993
$W \to \tau\nu + 4$ Jets	AlpGen + Jimmy	mc11_7TeV.107704.AlpgenJimmyWtaunuNp4_pt20.merge.AOD.e835_s1299_s1300_r3043_r2993
$W \to \tau\nu + 5$ Jets	AlpGen + Jimmy	mc11_7TeV.107705.AlpgenJimmyWtaunuNp5_pt20.merge.AOD.e835_s1299_s1300_r3043_r2993
WW	HERWIG	mc11_7TeV.105985.WW_Herwig.merge.AOD.e825_s1310_s1300_r3043_r2993
WZ	HERWIG	mc11_7TeV.105987.WZ_Herwig.merge.AOD.e825_s1310_s1300_r3043_r2993
ZZ	HERWIG	mc11_7TeV.105986.ZZ_Herwig.merge.AOD.e825_s1310_s1300_r3043_r2993
$t\bar{t}$	MC@NLO	mc11_7TeV.105200.T1_McAtNlo_Jimmy.merge.AOD.e835_s1272_s1274_r3043_r2993
QCD: $b\bar{b}$	PYTHIA	mc11_7TeV.108405.PythiaB_bbmu15X.merge.AOD.e825_s1310_s1300_r3043_r2993
QCD: $c\bar{c}$	PYTHIA	mc11_7TeV.106059.PythiaB_ccmu15X.merge.AOD.e825_s1310_s1300_r3043_r2993
		AtlFast2 samplesfor the signal process used for the template validation
$\sin^2\theta_W^{\text{eff}} = 0.232$	PYTHIA	mc11_7TeV.106047.PythiaZmumu_no_filter.merge.AOD.e1025_a131_s1353_a139_r2900
$\sin^2\theta_W^{\text{eff}} = 0.250$	PYTHIA	mc11_7TeV.129836.PythiaZmumu_sin2ThW_2350.merge.AOD.e1452_a131_s1353_a145_r2993

Table A.2.: All simulated event samples used in the present analysis.

B. Angular distributions for all bins in $p_{\mathrm{T}}(\mu\mu)$

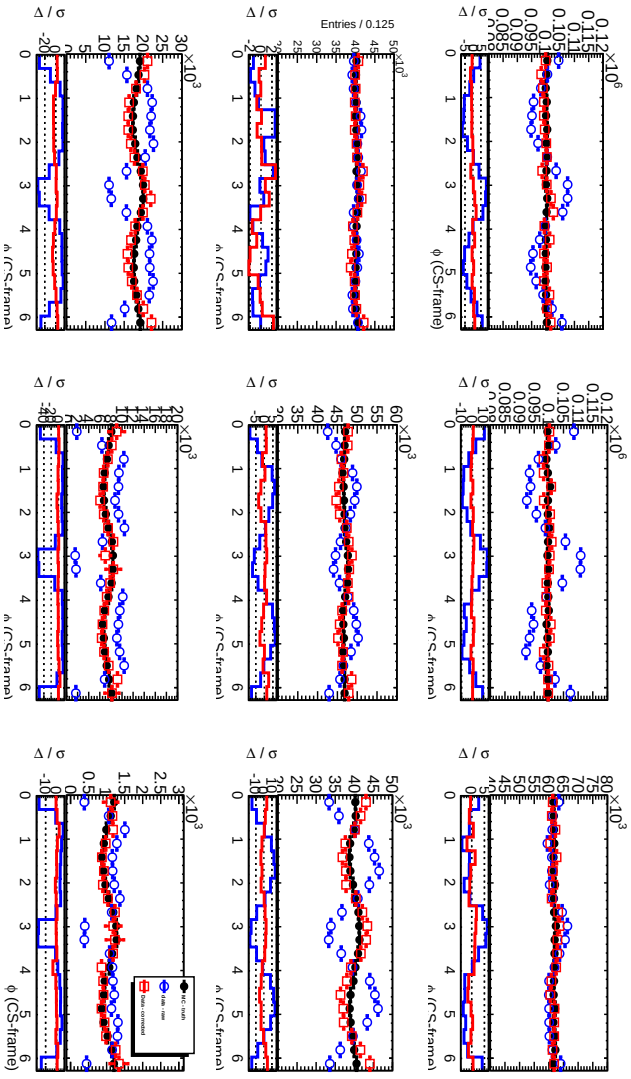

Figure B.1.: Azimuthal angular distributions obtained from the PYTHIA simulation without detector simulation (truth) in comparison of the measured distributions without (open circles) and with correction for detector effects (open squares). All distributions in one transverse momentum bin are normalized to the same integral for easier comparison of the shapes.

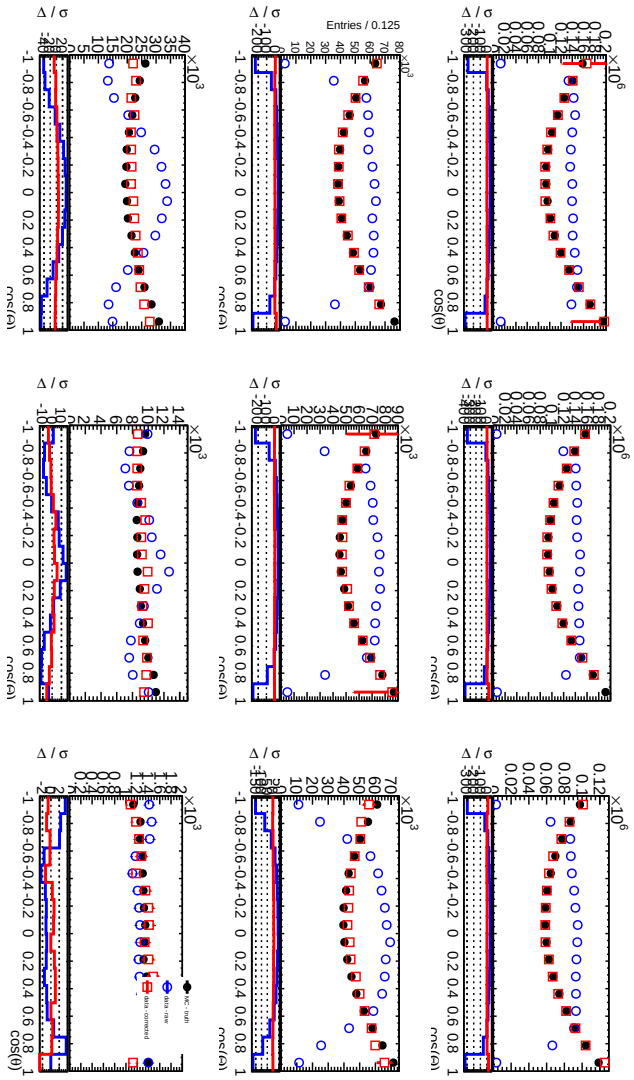

Figure B.2.: Polar angular distributions obtained from the PYTHIA simulation without detector simulation (truth) in comparison of the measured distributions without (open circles) and with correction for detector effects (open squares). All distributions in one transverse momentum bin are normalized to the same integral for easier comparison of the shapes.

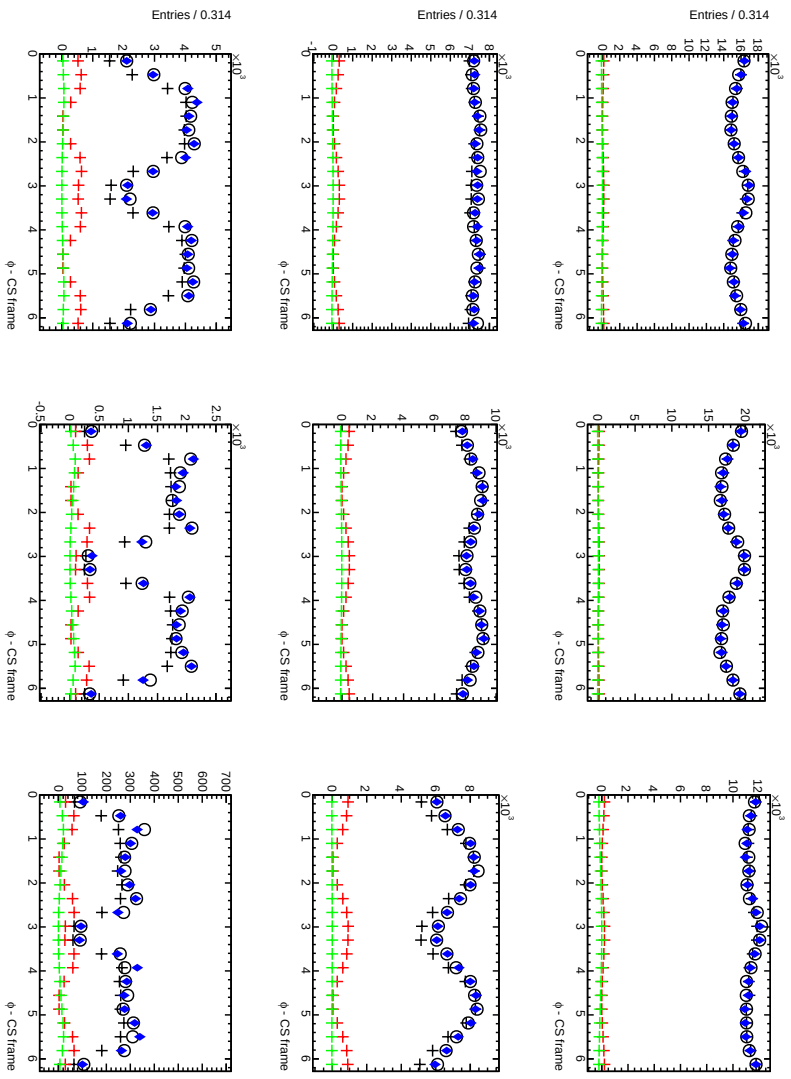

Figure B.3.: Template fit of the measured azimuthal angular distribution. The templates are constructed from the PYTHIA simulation with the $p_{\mathrm{T}}(Z)$ reweighted to the measured distribution. The three templates are shown as crosses (black, red and green), the measured distribution as open circles and the fit result as blue diamonds.

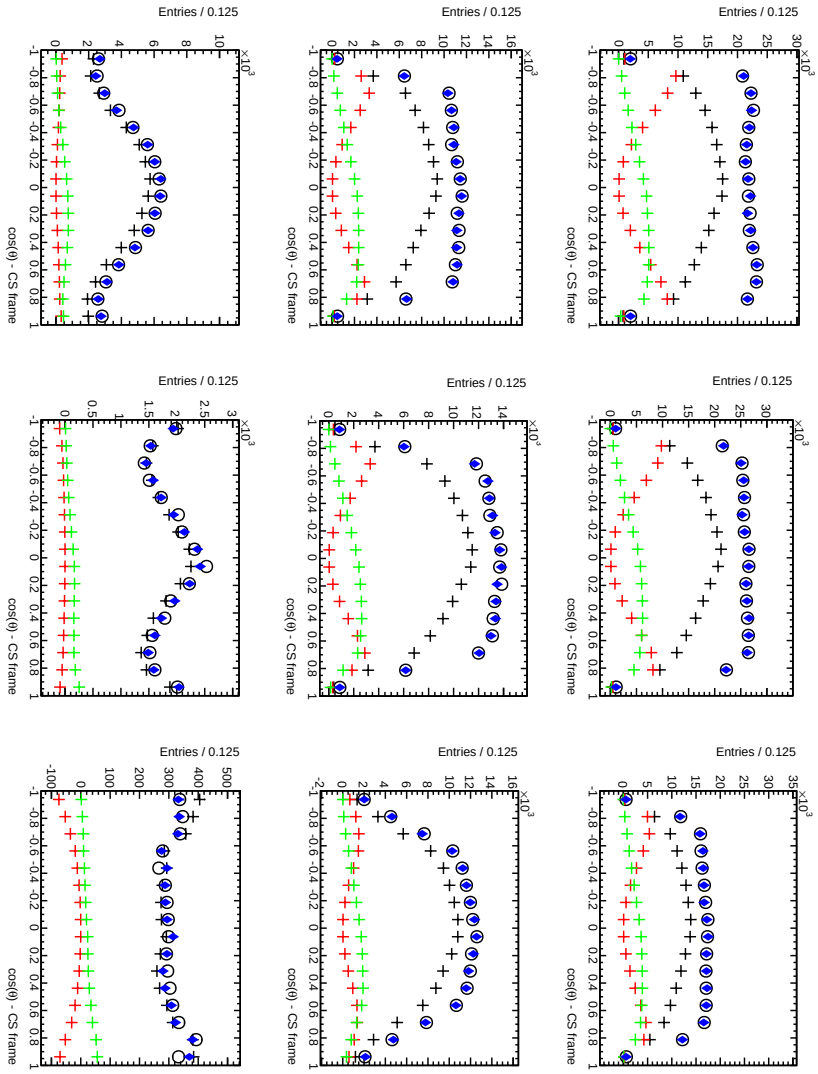

Figure B.4.: Template fit of the measured polar angular distribution. The templates are constructed from the PYTHIA simulation with the $p_{\mathrm{T}}(Z)$ reweighted to the measured distribution. The three templates are shown as crosses (black, red and green), the measured distribution as open circles and the fit result as blue diamonds.

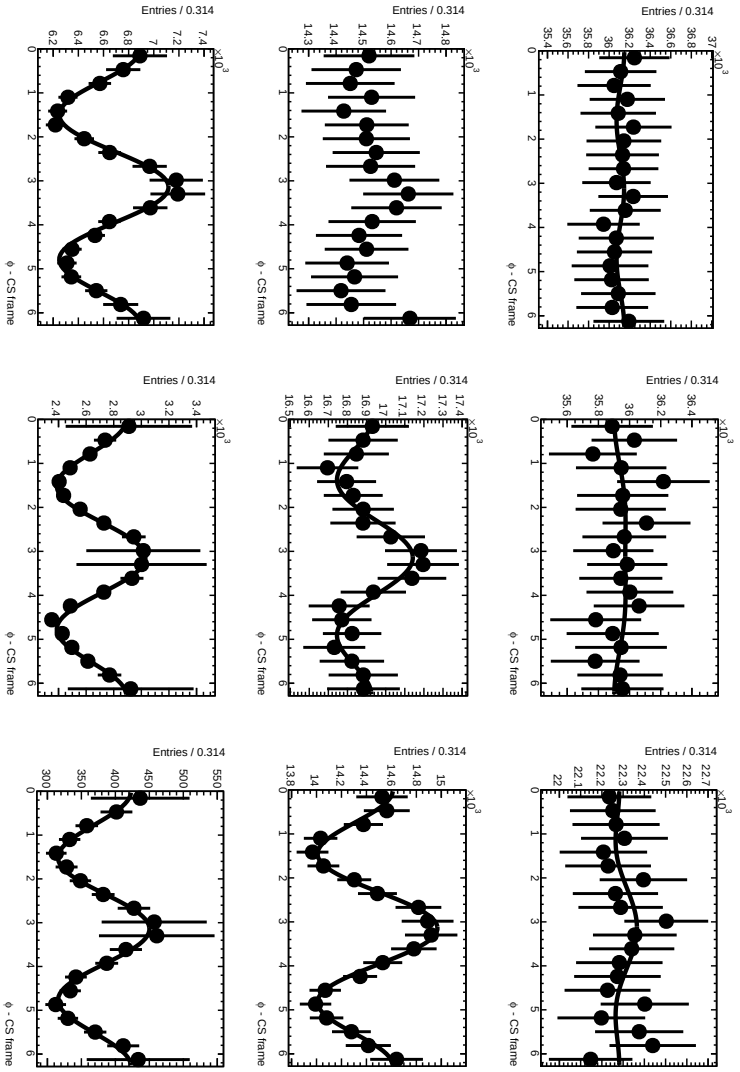

Figure B.5.: Closure test of the analytical fit method (1) which is used to extract the angular coefficients - azimuthal angle. The correction weights constructed from the PYTHIA simulation with the $p_{\mathrm{T}}(Z)$ reweighted to the measured distribution are fitted to the angular distributions are applied to the same MC sample. The analytical description of the angular distribution if fitted to the obtained distributions.

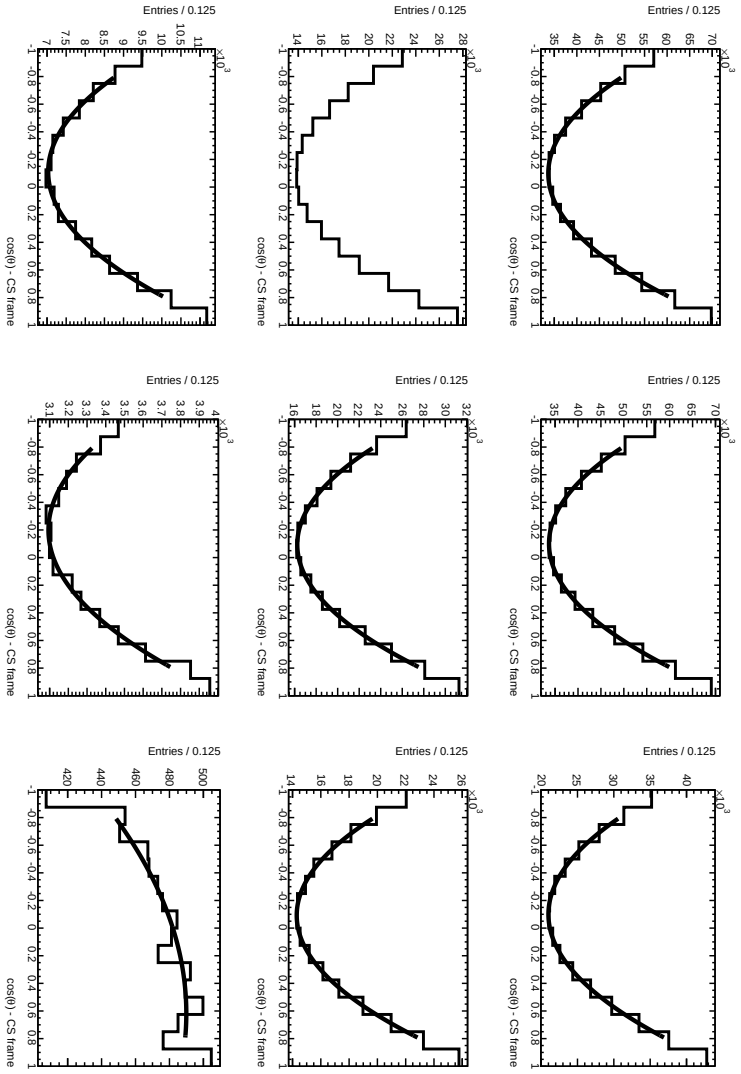

Figure B.6.: Closure test of the analytical fit method (1) which is used to extract the angular coefficients - polar angle. The correction weights constructed from the PYTHIA simulation with the $p_{\mathrm{T}}(Z)$ reweighted to the measured distribution are fitted to the angular distributions are applied to the same MC sample. The analytical description of the angular distribution if fitted to the obtained distributions.

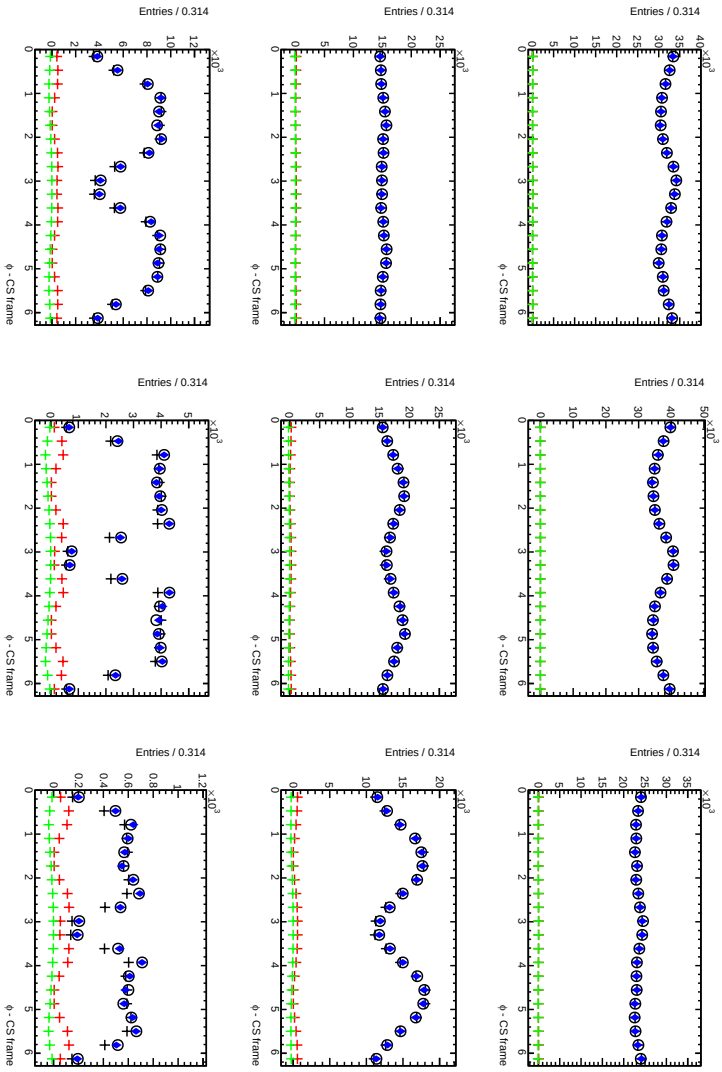

Figure B.7.: Closure test of the template fit method (2) which is used to extract the angular coefficients - azimuthal angle. The templates constructed from the PYTHIA simulation with the $p_{\mathrm{T}}(Z)$ reweighted to the measured distribution are fitted to the angular distributions obtained from the same MC sample. The three templates are shown as crosses (black, red and green), the measured distribution as open circles and the fit result as blue diamonds.

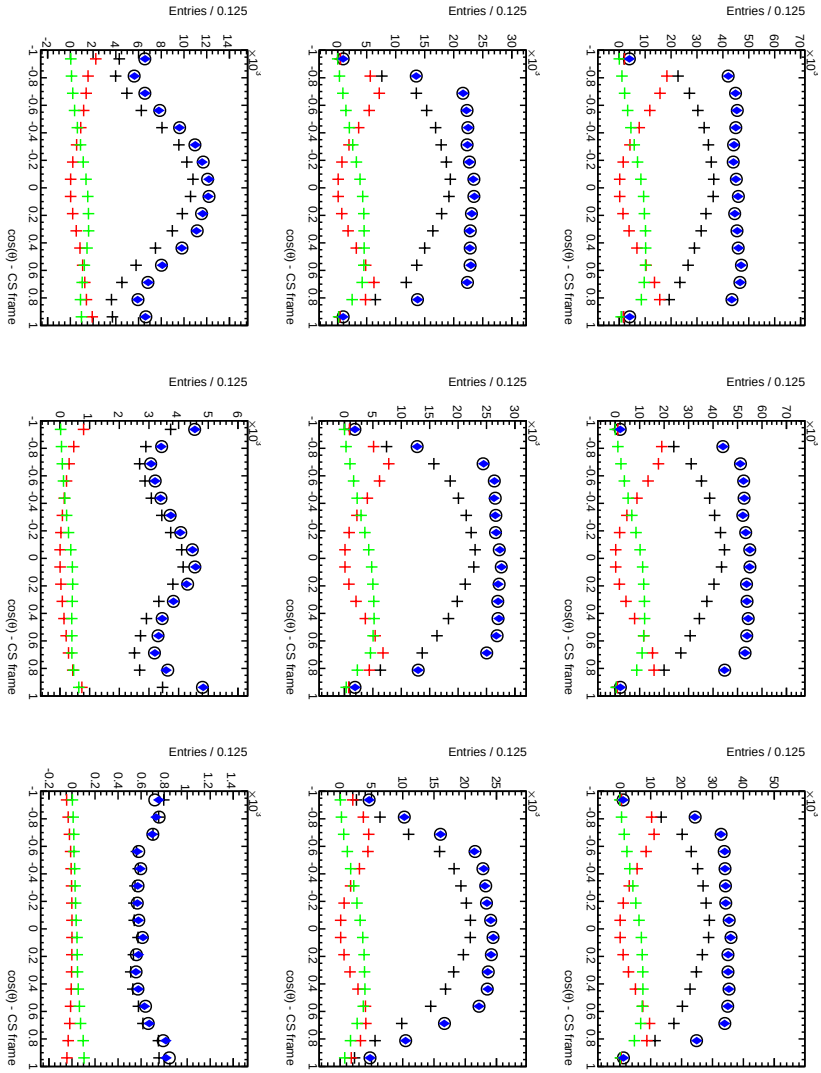

Figure B.8.: Closure test of the template fit method (2) which is used to extract the angular coefficients - polar angle. The templates constructed from the PYTHIA simulation with the $p_{\mathrm{T}}(Z)$ reweighted to the measured distribution are fitted to the angular distributions obtained from the same MC sample. The three templates are shown as crosses (black, red and green), the measured distribution as open circles and the fit result as blue diamonds.

Danksagung

An dieser Stelle möchte allen ein `DANKE` sagen, die mich bisher über ein längeres oder auch kürzeres Stück meines Weges begeleitet, geprägt und begeistert haben. Obwohl damit eigentlich alles gesagt ist möchte ich einige Menschen hervorheben:

- Meine Eltern. Die immer und überall in allen Lebenslagen für mich da sind und mich mehr unterstützen als mir bewust ist.
- Götz, für die ausgezeichnete Betreuung während meiner Zeit am CERN und darüber hinaus.
- Herrn Wermes, für die vielen Diskussionen, ausgezeichneten Ratschläge, die Betreuung und die Ermöglichung dieser Promotion.
- Meinen Freunden in Genf, Bonn und anderen Teilen der Welt. Für die schöne Zeit mit euch und die Unterstützung in allen Lebenslagen.
- Die Studienstiftung, für die unvergesslichen Sommerakademien und die Förderung meiner Arbeit.
- Stefanie, für so vieles.